Texture and Microstructure Development of the Silicon Containing Magnesium Alloys after Equal Channel Angular Pressing

Dissertation
zur Erlangung des Grades eines Doktors
der Ingenieurwissenchaften

vorgelegt von

Dipl. -Ing. Weimin Gan
aus Anhui / VR China

genehmigt von
der Fakultät für Natur- und Materialwissenschaften
der Technischen Universität Clausthal

Tag der mündlichen Prüfung
15 August, 2008

Texture and Microstructure Development of the Silicon Containing Magnesium Alloys after Equal Channel Angular Pressing

Dissertation
zur Erlangung des Grades eines Doktors
der Ingenieurwissenchaften

vorgelegt von

Dipl. -Ing. Weimin Gan
aus Anhui / VR China

genehmigt von
der Fakultät für Natur- und Materialwissenschaften
der Technischen Universität Clausthal

Vorsitzender der Promotionskommission: Prof. Dr. rer. nat. Albrecht Wolter

Hauptberichterstatter: Prof. Dr. rer. nat. Dr.-Ing. habil. Heinz-Günter Brokmeier

Berichterstatter: Prof. Dr.-Ing. Mingyi Zheng

Tage der mündlichen Prüfung: 15.08.2008

Diese vorliegende Arbeit wurde am Institut für Werkstoffkunde und Werkstofftechnik der Technischen Universität Clausthal angefertigt.

GKSS
FORSCHUNGSZENTRUM
in der HELMHOLTZ GEMEINSCHAFT

HELMHOLTZ
GEMEINSCHAFT

TU Clausthal
Clausthal University of Technology

1920
哈工大

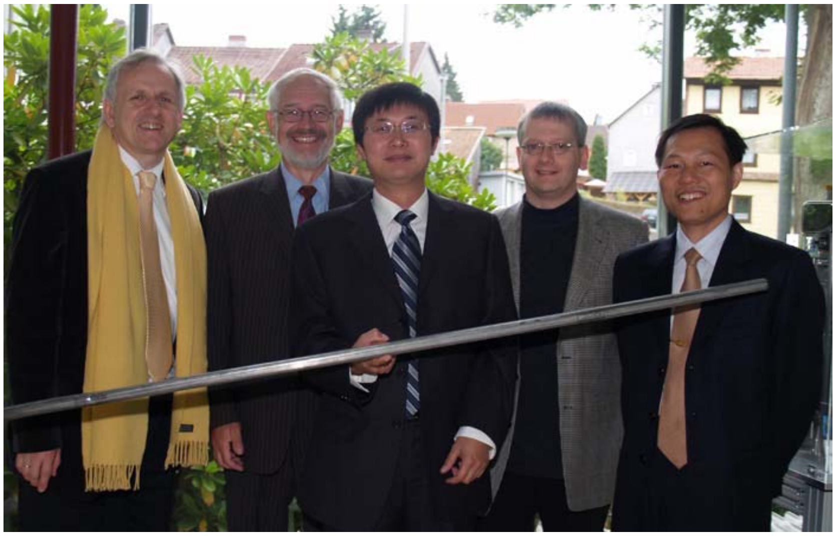

Stehen für das gute Verhältnis zwischen der TU-Clausthal und dem Harbin Institute of Technology: Prof. Albrecht Wolter, Prof. Heinz-Günter Brokmeier, Weimin Gan, Prof. Frank Endres und Prof. Mingyi Zheng (Foto von TU Pressereferent Christian Ernst, 15. 08. 2008).

Texture and Microstructure Development of the Silicon Containing Magnesium Alloys after Equal Channel Angular Pressing

Weimin Gan

Dissertation

TU Clausthal
2008

Acknowledgements

This work is a first cooperation between TexMat (Texture Analysis in Materials Science) research group at IWW (School of Materials Science & Engineering), TU Clausthal, Germany and High Performance Mg research group at Harbin Institute of Technology (HIT), P.R. China.

I would like to express my sincere regards for and gratitude to my supervisor Prof. Dr. Heinz-Guenter Brokmeier at TexMat, for his patience, support, encouragement and guidance during the period of this work.

I am also grateful to the advisor Prof. Dr. Kun Wu and Prof. Dr. Mingyi. Zheng at HIT for their kindly guiding, very helpful discussion and selfless help. Special thanks are given to Prof. Zheng for his carefully reviewing my thesis.

Thanks very much for Prof. Dr. Albrecht Wolter chairing my oral examination.

I am also very grateful to the useful discussion with Prof. Dr. Lothar Wagner at IWW (TU-Clausthal), Prof. Dr. Andreas Schreyer at GeNF and Prof. Dr.-Ing. Karl Ulrich Kainer at MagIC (GKSS).

The support from the DAAD-Helmholtz scholarship (10.2005-01.2008) is gratefully acknowledged.

I am grateful to the permission of the measurement beam time at GeNF (FRG-I, Geesthacht), Stress-Spec (FRM-II Munich), HARWI-II-W2 by accepted proposals. Kind help and nice discussions with the technicians at each facility are acknowledged.

I must show my sincere thanks to my colleagues Bernd Schwebke, Peter Spalthoff, PhD Candidate Emad Maawad, PhD Candidate S. Lenser, PhD Candidate Christian Randau, Dr. Zuzana Zúberová at TexMat, Dr. Sangbong Yi at MagIC (GKSS); and Dr. Xiaoshi Hu, Dr. Yanqiu Wang, Dr. Xiaojun Wang, Ph.D. Candidate Hai Chang and other colleagues at HIT, for their kind help and nice discussions during the experimental procedures.

Sincere thanks are also shown to the colleagues at GeNF (Geesthacht Neutron Facility) FRG-1 at GKSS Research Center, Geesthacht.

I am very appreciated for the kind helps in my daily life at Geesthacht from best friends Dr. Zhiyong Xie, Dr. Yuanding Huang, Dr. Zisheng Zhen, Dr. Xiumei Qi, Dr. Xuezhu Ma, Dr. Zhenzhen Wen, et al. who ever or now work at GKSS.

Finally, special thanks are given to my family housing at China, where is far separated by seas and oceans, for their understanding and encouragement during my work and stay in Germany.

1. Abstract

The global demand for energy and raw materials is increasing rapidly; however, the amount of available resources in the coming decades is very likely to decline. A promising approach to effectively use the resources and preserve the environment is the development and application of light-weight materials. Magnesium, which is the lightest metallic structural materials with a density of 1.74 g/cm^3, is an attractive candidate for light-weight applications, such as in automotive construction, astronautic components, electronic production, et al. Apart of the lowest density, the high specific strength, high specific stiffness, high damping capacity, and good castability as well as the high possibility of recycling are also the big advantages of Mg.

However, in fact the industrial usages of Mg are very limited comparing to steel and aluminum alloys, which are attributed to the most two disadvantages of Mg, i.e. relatively low strength and ductility, and low anti-corrosion property. Many efforts have been taken to improve the mechanical property of Mg, two of which to develop wrought Mg alloys with high strength and high ductility are alloying and deformation. Addition of second phases (intermetallic compound, quasicrystalline phase, et al.) to Mg can greatly improve its strength, especially at elevated temperatures. Alloying by Si, which is very low costive to form Mg-Si alloys, indicates that these alloys have high potential as heat resisting alloys because an intermetallic compound Mg_2Si is formed, which exhibits a high melting temperature, low density, high hardness, and a low thermal expansion coefficient. Mg-Si alloys could therefore potentially be used at elevated temperatures.

Unfortunately, Mg alloys containing second phases have low ductility due to the brittleness of coarse-grained second phase and their in-homogeneous distribution in matrix. Microstructures must therefore be optimized to improve the properties of Mg. According to Hall-Petch law the refinement of grains can improve the mechanical property of materials. Grain refinement in Mg can be obtained by thermo-mechanical processes, such as normal hot extrusion and rolling. Equal channel angular pressing (ECAP), as one prospective techniques of sever plastic deformation (SPD), is a novel metal forming process that can produce bulk ultra-fine grained (UFG) materials for a wide range of materials, including Mg alloys. In addition to the grain-refinement due to recrystallization, high intensity of texture will be obtained in the materials after thermo-mechanical processes.

Though the practical application of ECAP is still questionable, the unique texture developed by ECAP in ***fcc, bcc*** and ***hcp*** materials is one of the most attractive topics nowadays. Variation of the texture by ECAP processing with the construction of deformation device and processing parameters is still not fully understood. Since texture records the thermo-mechanical behavior of whole ECAP process, the deformation mechanism during ECAP can be understood by systematic analysis on texture evolution. Furthermore, it is possible to tailor the texture by a combination of ECAP with normal deformation as one desired. Another importance of the texture analysis in ECAP-processed Mg is related to the homogenous deformation of ECAP processing itself.

In addition, the low formability of Mg is originated from its crystallographic structure, which results in limited number of active deformation systems. Moreover, due to these reasons the deformed Mg easily exhibits a pronounced anisotropy in mechanical properties. Since most Mg alloys show a strong texture after typical thermo-mechanical processes such as rolling,

extrusion, annealing and ECAP, the orientation distribution of the crystallites (texture) is one of the most important parameters influencing on mechanical properties.

Objective and main topics

An attempt has been made to subject Mg-Si alloy which containing Mg_2Si hard to deform particles to ECAP. Firstly, improved mechanical property of Mg-Si alloy is expected. Secondly, present study will be carried out to contribute to a basic understanding of the interrelationship among texture and deformation mechanism during ECAP of Mg, the microstructure optimization in ECAP-processed Mg containing Si alloys, and as well the tensile behavior of ECAP-processed Mg. Effect of the second phase on the ECAP-processed texture will be strengthened. Homogeneity of the ECAP deformation will also be investigated. For attaining these extensive and complicated goals the general topics are roughly separated into following four parts.

Firstly, investigations on the effect of ECAP on mechanical behavior of Mg-Si alloy with different initial input texture will be performed, and the same work will be done in pure Mg for comparison. Three ECAP rotations will be used after optimizing the processing temperature. Tensile behavior in the ECAP-processed Mg and Mg-Si alloy under different processing conditions will be analyzed. Effect of the addition of Si to Mg on tensile behavior will be investigated.

Secondly, microstructure evolution of the ECAP-processed pure Mg and Mg-Si alloy with different rotations routes will be observed. Refinement and re-distribution of the second phase in the ECAP-processed billet via three different routes will be compared, and as well the matrix grains. Grain refinement mechanism and the effectiveness of ECAP to refine and re-distribute the hard second phase will be discussed.

Thirdly, texture development in the ECAP-processed pure Mg and Mg-Si alloy via different rotation routes and passes will be characterized by neutron radiation since neutron diffraction is powerful for bulk texture analysis. Texture development will be related to the deformation mechanism of ECAP. Effect of different initial textures (as-cast and as-extruded) on the following texture evolution will be analyzed. Another important discussion is laid on how the second phase affects the development of ECAP-processed texture by comparing Mg-Si alloy with pure Mg.

Lastly, a significant investigation on the local texture analysis in a single pass ECAP-processed pure Mg will be carried out to understand how the local texture evolves in the whole 90° channel from ingoing to outgoing regions. This texture analysis is firstly performed using neutron diffraction; and then more details at the deformation region is analyzed by synchrotron diffraction since that hard x-ray has high reflux comparing to neutrons. Texture homogeneity property in the ECAP-processed billet is therefore understood. Relationship between texture and deformation model is discussed, which will contribute to a better understanding of the ECAP mechanism under current construction of ECAP device.

2. Literature review

2.1 Introduction to Magnesium and its alloys

Magnesium has hexagonal close-packed (HCP) crystallographic structure with the lattice parameters of $a_1=a_2=0.312$ nm, c=0.512 nm, c/a= 1.632, $\alpha = \beta = 90°$, $\gamma = 120°$, as shown in Fig. 2-1, and its space group is P63/mmc (No. 194). Considering atomic packing factor and coordination number, HCP structure has the same value with FCC (face centred cubic) structure of 0.74 and 12, respectively; but has a different staking sequence of 'ABAB…' comparing with 'ABCABC…' sequence in FCC structure [1]. The physical properties of Mg are listed in Tab.2-1. The density of pure Mg at room temperature is only 1.74 $g\cdot cm^3$ which is almost the same as nylon materials, and is less than almost all of the currently used engineering metals, see in Fig. 2-2. The melting point of pure magnesium is about 650°C.

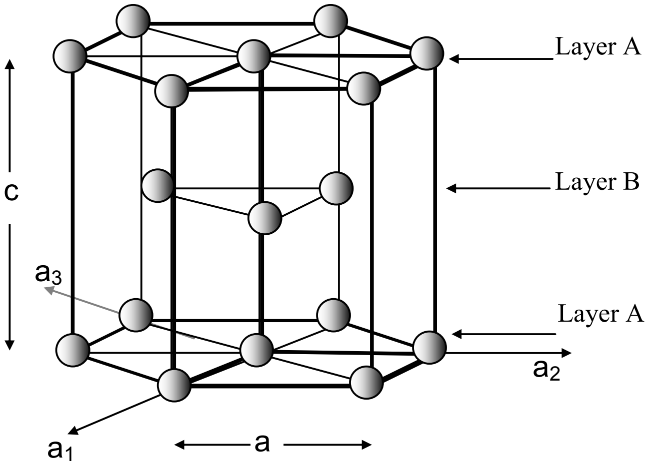

Fig. 2-1 Hexagonal close-packed structure

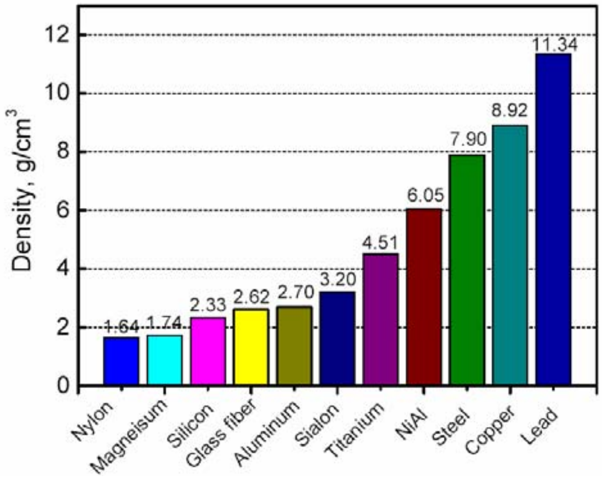

Fig. 2-2 Densities of the currently used engineering materials [2, 4, 5].

Magnesium is the eighth most abundant element and constitutes about 2.1% of Earth's crust. It is the third most plentiful element dissolved in seawater, with a concentration averaging 0.13 percent [2]. Although magnesium is found in over 60 minerals, only dolomite, magnesite, brucite, carnallite, and olivine are of commercial importance. Magnesium and magnesium compounds are produced from seawater, well and lake brines and bitterns, as well as from the minerals noted above [3].

The advantages of magnesium and magnesium alloys are listed as follows [2-5],

- lowest density of all metallic constructional materials;
- high specific strength;
- good castability, suitable for high pressure die casting;
- can be turned/milled at high speed;
- good weldability under controlled atmosphere;
- much improved corrosion resistance using high purity magnesium;
- readily available;
- high damping capacity;
- compared with polymeric materials:
  - better mechanical properties;
  - resistant to ageing;
  - better electrical and thermal conductivity;
  - recyclable.

The disadvantages of Mg are summarized based on the following:

- low elastic modulus;
- limited cold workability and toughness;
- limited high strength and creep resistance at elevated temperatures;
- high degree of shrinkage on codification;
- high chemical reactivity;
- low corrosion resistance in some applications.

Tab.2-1 Physical properties of Mg

Melting point	650 °C±2
Boiling point	1090 °C
Latent heat of fusion	0.37 MJ/kg
Latent heat of evaporation	5.25 MJ/kg
Heat of combustion	25.1 MJ/kg
Specific heat	
at 20°C	1030 $\mathrm{Jkg^{-1}K^{-1}}$
at 600°C	1178 $\mathrm{Jkg^{-1}K^{-1}}$
Electrical resistivity	
at 20°C	4.45 Ωm/cm
Thermal conductivity	
at 25°C	155 $\mathrm{Wm^{-1}K^{-1}}$
Linear coefficient of thermal expansion	
at 20°C	$25.2 \times 10^{-6}\ \mathrm{K^{-1}}$
at 20-300°C	$27\text{-}28 \times 10^{-6}\ \mathrm{K^{-1}}$
Density(solid)	
at 20°C	1.738 g $\mathrm{mm^{-3}}$
at 600°C	1.622 g $\mathrm{mm^{-3}}$
Density above 60°C	
liquid, g $\mathrm{cm^{-3}}$	$1.834\text{-}2.647 \times 10^{-4}\ \mathrm{K^{-1}}$
Standard redox potential	-2.372 V

As a metal, the principal use of Mg is an alloying additive to Al with these Al-Mg alloys being used mainly for beverage cans. Mg is very light as compared with Al, so it is used in several high volume part manufacturing applications, including automotive, astronautive and truck components. In 1957 a Corvette SS, designed for racing, was constructed with Mg body panels [6]. Volkswagen has used Mg in its engine components for many years. For a long time, Porsche used Mg alloys for its engine blocks due to the weight advantage. There is renewed interest in Mg engine blocks, as featured in the 2006 BMW 325i and 330i models [5]. The BMW engine uses an Al alloy insert for the cylinder walls and cooling jackets surrounded by a high temperature mg alloy AJ62A. Another large increasing application of Mg is electronic devices. Due to low weight, good mechanical and electrical properties, Mg is widely used for manufacturing of communication, consumer electronics and computer (3C) products, such as mobile phones, laptop computers, cameras, and other electronic components. Historically, magnesium was one of the main aerospace construction metals and was used for German military aircraft as early as World War I and extensively for German aircraft in World War II. Currently the use of magnesium alloys in aerospace is increasing, mostly driven by the increasing importance of fuel economy and the need to reduce weight. The development and testing of new magnesium alloys notably Elektron 21 which has successfully undergone extensive aerospace testing for suitability in both engine, internal and airframe components.

Though the solubility of alloying elements in magnesium is limited, which restricts the possibility the mechanical properties and chemical behavior, Magnesium can form solid solution or phases with many elements, such as aluminum (Al), zirconium (Zr), lithium (Li), zinc (Zn), manganese (Mn), silicon (Si), copper (Cu), silver (Ag), nickel (Ni), calcium (Ca), cadmium (Cd), thorium (Th), cobalt (Co), tin (Sn), gallium (Ga), and rare earth elements like cerium (Ce), lanthanum (La), yttrium (Y), etc.. The five basic groups of alloy systems, which are currently being commercially produced, are based on the major alloying elements: Al, Zn, Zr, and RE. These are subdivided as follows: Mg-Mn, Mg-Al-Mn, Mg-Al-Zn-Mn, Mg-Zr, Mg-Zn-Zr, Mg-Zr-RE, Mg-Zr-Ag-RE, Mg-Y-Zr-RE, Mg-Th-Zr, Mg-Th-Zn-Zr, etc.

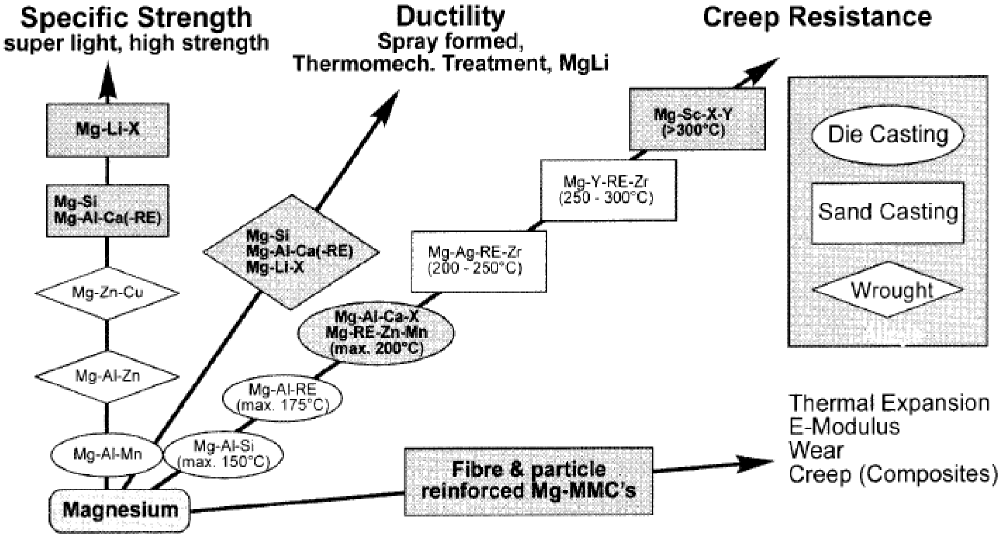

Fig. 2-3 Directions of alloy development in Mg [7].

The fast majority of Mg applications are covered by AZ91, a die-casting alloy. This alloy has insufficient creep resistance for many desirable applications at temperatures above 130ºC

[7]. Fig. 2-3 shows further development of Mg-Al for die-casting Mg-Al-Mn and for wrought alloys Mg-Al-Zn and for sand casting alloys with Mg-Si, Mg-Al-Ca-(RE). The development of Mg-Li-X is a development of super light alloys. A series of high performance Mg-based alloys was developed after discovery of the extremely efficient grain refining action of Zr. This effect results from the formation of high density tiny Zr particles in the melt, which act as potent grain nuclei.

The maximum solubility of Si into Mg is only 0.003 at. %. Fig. 2-4 (a) shows the binary phase diagram of Mg-Si, which indicates that Mg_2Si is the only metallic phase in Mg-Si alloys. The Mg-Si alloys have high potential as structural materials because the existence of an intermetallic compound of Mg_2Si which exhibits a high melting temperature of 1085°C, low density of 1.99 $g{\cdot}cm^3$, high hardness of 4500 $MN{\cdot}m^2$ and a low thermal expansion coefficient of 7.5×10^{-6} K and a reasonably high modulus of 120 GPa [8, 9]. Mg_2Si has the ***fcc*** crystallographic structure with a lattice parameter a=0.6315 nm, as shown in Fig. 2-4 (b). Ingot metallurgy Mg-Si alloys showed very low ductility and strength because of the large Mg_2Si particle size and brittle eutectic phases. Researches indicated that the mechanical properties of Mg-Si alloys could be improved by the applications of advanced processing techniques, such as hot extrusion, rapid solidification, directional solidification and mechanical alloying. Refinement and the homogenization of the Mg_2Si are mainly responsible for the improvement in the mechanical properties [10]. However, these processing methods may lead to the increase of the production cost. It is significant to develop an effective and low costive technique to improve the mechanical property of Mg-Si alloys.

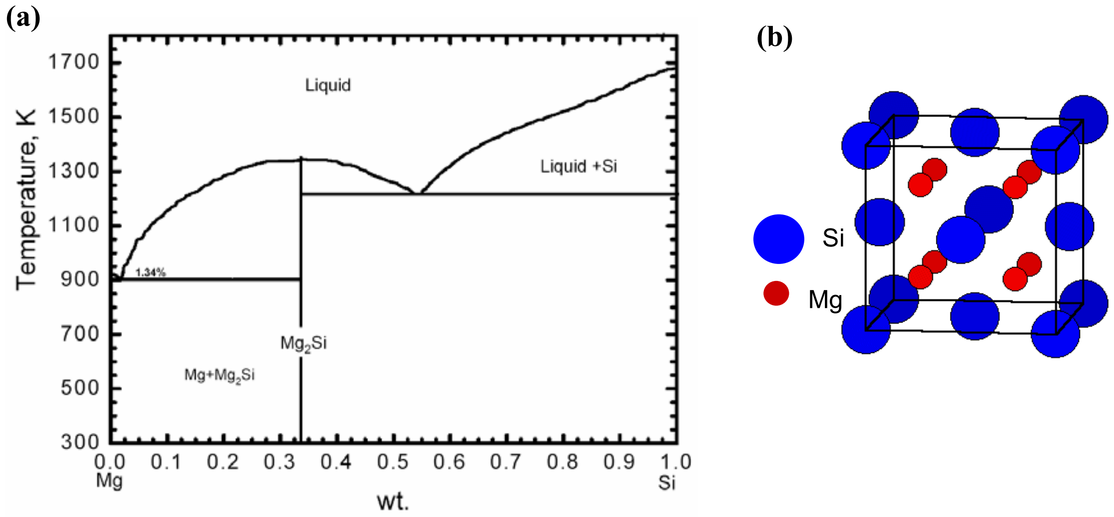

Fig. 2-4 (a) Mg-Si binary phase diagram; (b) crystal structure of the intermetallic compound Mg_2Si [11].

2.2 Deformation modes of Mg

2.2.1 Slip mode

Dislocations in Mg

Detailed explanations on the dislocations in hexagonal structured metals can be found in the earlier studies of Patridge [12]. Some possible Burgers vectors of perfect and partial dislocations are analogously represented in Fig. 2-5 using the notation of Thomson tetrahedron, which is convenient for f.c.c. metals, and the characteristics of corresponding Burgers vectors by Miller-Bravais indices are listed in Tab.2-2, respectively. The dislocations with the Burgers vector ***b*** = 1/3 <11$\bar{2}$0>, so called <***a***> dislocation, allows the deformation on the basal plane, while those with the Burgers vector <***c***> = <0001> are responsible only for the deformation along the **c**-axis. The dislocations with ***b*** = 1/3 <11$\bar{2}$3>, so called <***c+a***> dislocations, have the deformation components along the ***c*** and ***a***-axes. From the energetic point of view in perfect dislocations, the <***a***> dislocations are the most favourable and the <***c+a***> dislocations are the most unfavourable with the longest Burgers vectors. It is dependent on the planar density of each crystallographic plan, which dislocations are really activated during deformation. As mentioned in the previous section the main factors are the c/a-ratio and the possibility of the dissociation to partial dislocations. With the decrease of the c/a-ratio the plane of the highest planar density is changed from basal plane to prismatic plane. This variation explains the basal <***a***> slip in Cd and Zn as the main slip systems, i.e. slip of <***a***> dislocations on the basal plane, and the prismatic <***a***> slip in Zr and Ti as the main slip system.

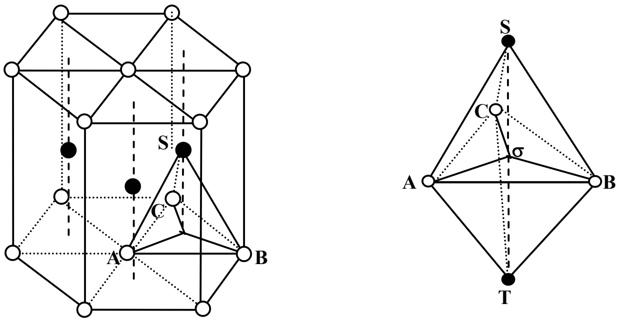

Fig. 2-5 Burgers vectors in the HCP structure on the Thomson tetrahedron.

Tab. 2-2 Some Burgers vectors of dislocations in HCP crystal and their properties.

Type of dislocation (Fig.2-5)	Total number of dislocations	Direction indices (Miller-Bravis)	Magnitude of vector	Relative energies of dislocations
Perfect dislocations				
AB, <c>	6	1/3 <1 1 $\bar{2}$ 0>	$\|a\|$	$\|a\|^2$
ST , Ts	2	<0 0 0 1>	$\|c\|$	$\|c\|^2 = 8/3\ \|a\|^2$
ST+AB, <c>	12	1/3 <1 1 $\bar{2}$ 3>	$\sqrt{\|a\|^2+\|c\|^2}$	$11/3\ \|a\|^2$
Imperfect dislocations				
Aσ, Bσ, <c>	6	1/3 <1 0 $\bar{1}$ 0>	$\|a\|/\sqrt{3}$	$1/3\ \|a\|^2$
σS, σT, <c>	4	1/2 <0 0 0 1>	$\|c\|/2$	$2/3\ \|a\|^2$
AS, BS, <c>	12	1/6 <2 0 $\bar{2}$ 3>	$\sqrt{\|c\|^2/4+\|a\|^2}$	$\|a\|^2$

According to Von Mises criterion, a polycrystal requires five shear systems to undergo homogeneous strain without change in volume; a slip system is independent of others provided its operation produces a change in crystal shape that cannot be produced by a suitable combination of amounts of slip on those other systems. The 6 types of slip system available in hexagonal metals are listed in Tab. 2-2, acting simultaneously but independently, will provide a total 4 independent slip modes. The slip system includes the basal and prismatic <***a***>, prismatic type I and Π <***c***> and pyramidal planes <***a***> and <***a+c***>. The predominated activated slip system in Mg is the basal plane <***a***> slip. As describe by Schmid law,

$$\sigma_s / \sigma_n = \cos\varphi \cos\lambda \qquad \text{(Eq. 2-1)}$$

where, σ_s is the shear stress resolved on the slip or twin plane and in the slip or twinning direction, σ_n is the applied stress, φ and λ are the angles between the stress axis and slip or twin plane normal and slip or twinning direction, respectively. σ_s must attain a critical value, called the critical resolved shear stress (CRSS), before slip happens. CRSS of different activation slip system has been earlier reported in single crystal Mg. According to the reported data, the CRSS of a basal slip system at room temperature is approximately 1/100 those of non-basal slip systems on prismatic and pyramidal planes. Therefore, plastic deformation in polycrystalline alloys has been thought to occur almost entirely by basal plane slip. If this is the case, the basal slip system provides only two independent slip system, far fewer than the necessary five independent systems for homogeneous deformation. The next easiest slip systems that are necessary are a $\{10\bar{1}1\} < \bar{1}2\bar{1}0 >$ first-order pyramidal slip system with an ***a***-axis slip direction, a $\{10\bar{1}1\} < \bar{1}\bar{1}23 >$ first-order pyramidal plane slip system with a <***c+a***> slip direction, and a $\{11\bar{2}2\} < \bar{1}\bar{1}23 >$ second-order pyramidal slip system with a <***c+a***> slip direction. Earlier researches has shown that h.c.p. metals like Mg and Zn was only slightly temperature-dependent below room temperature, while in Mg there was an increase by two orders of magnitude in the CRSS for prismatic slip when the temperature was lowered from 300 to 196°C. More activations of the non-basal plane sliding and twining are widely investigated in Mg and its alloys. The activation of the non-basal slip system was enhanced with increasing Y concentration in the grains in Mg-Y binary alloys [13]; and the forest dislocation hardening due to activation of the non-basal slip system played an important in the strengthening of Mg-Y alloys.

Among non-basal slip systems, the second-order pyramidal slip, $\{11\bar{2}2\}\ 1/3 < \bar{1}\bar{1}23 >$, is important. Yoo et al. [14, 15] investigated the stability of <***c+a***> dislocations and their mobility in h.c.p. metals. Identification of <***c+a***> dislocations in Mg was made by TEM. Simulation analysis and texture measurements demonstrated that the <***c+a***> dislocations play an important role in the texture evolution of Mg alloys. Investigation on the texture evolution during tensile test of the extruded AZ31 from room temperature up to 250°C showed that direct evidence for the high activity of the <***c+a***> slip system for temperatures ≥ 200°C [16]. A possible source mechanism for no-basal <***c+a***> slip dislocation was proposed based on the deformation of an attractive junction between glissile <***a***> and sessile c dislocations from the prismatic plane into a pyramidal plane by Yoo and his co-workers [17]. Researches on tensile deformation of the ECAP-processed fine-grained AZ31 and subsequent annealing by Koike etc. indicated that a major deformation mechanism from all non-basal slip systems in AZ31 alloy is <***c+a***> dislocation systems in pyramidal slip system [18]. The activity of non-basal slip systems also plays an important role in dynamic recovery of Mg alloys, which has been experimentally proved to be contributed to the improvement of the ductility of Mg alloys [18]. Experimental results of the high ductility or superplasticity behaviour of the fine-grained Mg alloys showed that grain boundary sliding is the main deformation mechanism; and accommodation of stress concentration around triple point of grain boundary is necessary if grain boundary sliding continues without any fracture [19]. Dislocation slip and diffusion are considered to be the main accommodation mechanism during the superplastic deformation of Mg alloys.

Tab. 2-3 Independent slip systems in ***hcp*** metals [12].

Slip plane	**Slip direction**	**Number of slip systems**	
		Total	**Independent**
Basal (0001)	a type, $<11\bar{2}0>$	3	2
Prism type I, {10-10}	a type, $<11\bar{2}0>$	3	2
Prism type I, {10-10}	c type, <0001>	3	2
Prism type II, {11-20}	c type, <0001>	3	2
1st order pyramidal type I, {10-11}	a type, $<11\bar{2}0>$	6	4
2nd order pyramidal type II, {11-22}	c+a, $<11\bar{2}3>$	6	5

2.2.2 Twinning mode

Twinning systems in Mg

Twinning is an important mode of plastic deformation in h.c.p. metals. It contributes to texture evolution by reorienting the twinned areas of the grains. Furthermore, the strain hardening behavior of Mg alloys can also be influenced by twinning. The crystallographic elements for twin and shape changes produced by $\{10\bar{1}2\}$ twin which normally occurs in Mg are described in Fig. 2-6 [12]. There are two planes that remain undistorted by the twinning shear (K_1 and K_2). While the twinning plane K_1, containing the twinning shear direction η_1, does not change its position, K_2 displaces to K_2' by the twinning shear. The cross-sections between the plane of shear and K_2 (K_2') are denoted by η_2 (η_2'), Fig. 2-6 (a). The twinning shear S varies with c/a-ratio, the acute angle φ between K_1 and K_2 is related to the amount of twinning shear *S*, as following;

$$S = 2\cot\varphi \qquad \text{(Eq. 2-2)}$$

The crystal shape changes followed by $\{10\bar{1}2\}$ twin produce the 4° tilting of $(\bar{1}012)$ K_2 plane and simultaneously 86° rotation of basal plane, shown in Fig 2-6 (b) and (c), respectively. Because the c/a-ratio in Mg is slightly smaller than the ideal case, the symmetry conditions require the second undistorted plane, K_2, to be tilted clockwise; in reverse case the K_2 plane rotates counter-clockwise. This has an effect of lengthening the crystal inside the twinned volume in a direction perpendicular to basal plane. That is, the tensile stress perpendicular to basal plane, or compression parallel to basal plane, favours $\{10\bar{1}2\}$ twinning in Mg. The indices of crystallographic planes and directions after twinning can be deduced in a mathematical way. If $K_1 = (H\ K\ L)$ and $\eta_2 = [U\ V\ W]$ (or alternatively K_2 and η_1, respectively), then the directional Miller indices [*u v w*] in the matrix transform to [*u′ v′ w′*] in the twinned volume according to;

$$\begin{aligned} u' &= u(HU + KV + LW) - 2U(Hu + Kv + Lw) \\ v' &= v(HU + KV + LW) - 2V(Hu + Kv + Lw) \\ w' &= w(HU + KV + LW) - 2W(Hu + Kv + Lw) \end{aligned} \qquad \text{(Eq. 2-3)}$$

Planar indices (*h k l*) in the parent matrix transform to (*h′ k′ l′*) in the twin according to :

$$h' = h(HU + KV + LW) - 2H(Uh + Vk + Wl)$$
$$k' = k(HU + KV + LW) - 2K(Uh + Vk + Wl)$$
$$l' = l(HU + KV + LW) - 2L(Uh + Vk + Wl) \qquad \text{(Eq. 2-4)}$$

It is apparent from these equations that basal plane in matrix transfoms to $(\bar{1}010)_{twin}$ after $\{10\bar{1}2\}$ twinning. The relative positions of planes and directions before and after twinning is also described in the standard stereographic projection as 86° rotation of the basal pole.

The twinning deformation is characterized in general as following;

- Twinning can be activated only under uni-directional sense;
- The amount of plastic shear by twinning is small;
- Twinning causes mostly large rotation of crystal;
- Twin boundary acts as a barrier for dislocation glide.

Despites of the limited contribution of twinning itself to plastic shear, an importance of twinning lays on the fact that the unfavourably oriented crystals for dislocation glide can be rotated to favourable direction, so that the dislocation slip can contribute to further deformation.

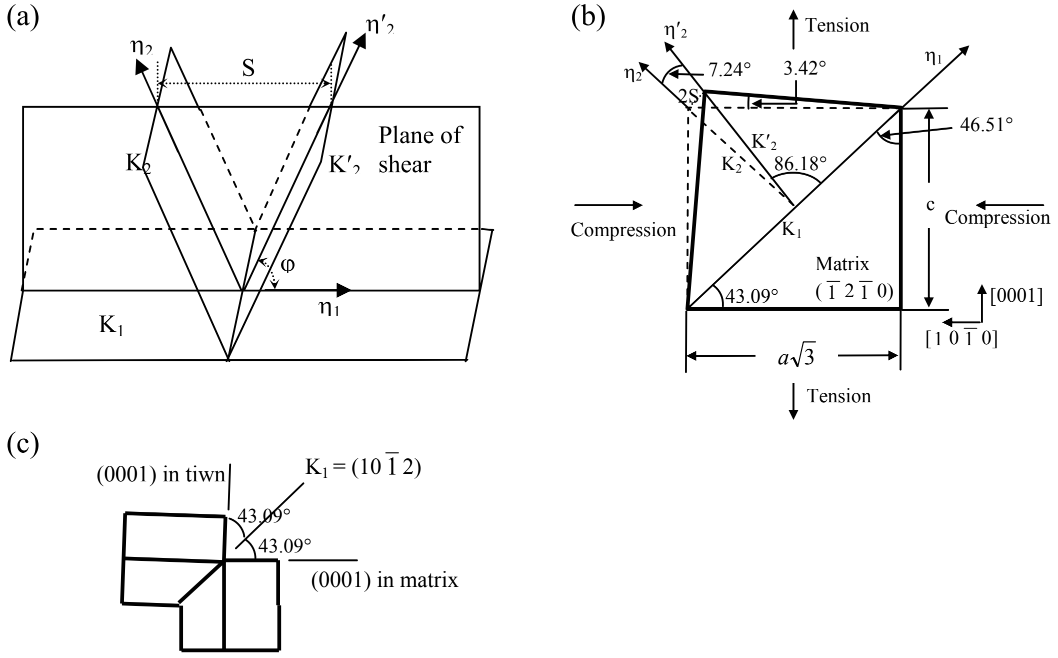

Fig. 2-6 (a) Spatial illustration for the crystallographic elements of twin. (b) Shape change produced by $\{10\bar{1}2\}$ twinning in Mg in viewpoint of twin elements, and (c) in viewpoint of basal plane, thick lines stand for the crystal.

The twin modes observed in Mg are listed in Tab. 2-4. The smaller amount of twinning shear and more simple of atomic shuffling, the larger possibility for activating the twin is expected. The twinning interface energy plays an important role, which should be low for easy activation. Additionally, the grain size in initial material has a relation to the twinned volume. Three types of twins are frequently reported in Mg alloys: extension twins, contraction twins and double twins. Extension twins $\{10\bar{1}2\} < 1\bar{1}01 >$ are preferred when there is an extension strain component parallel to the *c*-axis or when contraction is being applied perpendicular to the *c*-axis of the principle component. This tensile twinning gives extension along the *c*-axis in Mg and its alloys, which appears to increase the uniform elongation seen in tensile tests of the extruded AZ3 [20, 21]. Contraction twinning, including $\{10\bar{1}1\}$ $<10\bar{1}2>$, $\{30\bar{3}4\}$, and $\{10\bar{1}3\}$, on the contrary, can accommodate compression along *c*-axis. It is activated when there is a contraction strain component parallel to the *c*-axis or when macroscopic extension is being applied perpendicular to the *c*-axis. These twins are believed to form the compression bands in rolled polycrystals, and are important deformation mechanisms which determine the cold workability of Mg and its alloys [22]. In addition to primary twinning, secondary twinning can take place within the reoriented primary twins. This is known as double twinning. Generally, $\{10\bar{1}1\}$ and $\{10\bar{1}3\}$ contraction twins form first, after which $\{10\bar{1}2\}$ extension twins are propagated within the original contraction twins. The sequence of $\{10\bar{1}1\}$ - $\{10\bar{1}2\}$ double twinning is illustrated in Fig. 2-7, where the basal planes are reoriented at an angle of 37.5° from their original positions in untwined matrix. In a similar manner, after $\{10\bar{1}3\}$ - $\{10\bar{1}2\}$ double twinning, the basal planes are reoriented at an angle of 22°. Double twins leas to a net contraction along the *c*-axis [23]. The CRSS for the $\{10\bar{1}2\}$ $<1\bar{1}01>$ twins and the $\{10\bar{1}1\}$ $<10\bar{1}2>$ twins are 2 and 76-153MPa, respectively [24]. Hence, the tensile twinning occurs much easily, compared with the compression twinning and the mechanical anisotropy is more related to the tensile twinning.

Tab. 2-4. Twin systems observed in Mg, their elements, amount of twinning shear and complexity of atomic shuffling.

K_1	K_2	η_1	η_2	S	q
$\{10\bar{1}2\}$	$\{\bar{1}012\}$	$<10\bar{1}\bar{1}>$	$<\bar{1}01\bar{1}>$	0.130	4
$\{10\bar{1}1\}$	$\{10\bar{1}\bar{3}\}$	$<10\bar{1}\bar{2}>$	$<30\bar{3}2>$	0.137	8
$\{11\bar{2}1\}$	(0001)	$<11\bar{2}\bar{6}>$	$<11\bar{2}0>$	0.616	2
$\{11\bar{2}2\}$	$\{11\bar{2}\bar{4}\}$	$<11\bar{2}\bar{3}>$	$<22\bar{4}3>$	0.260	6

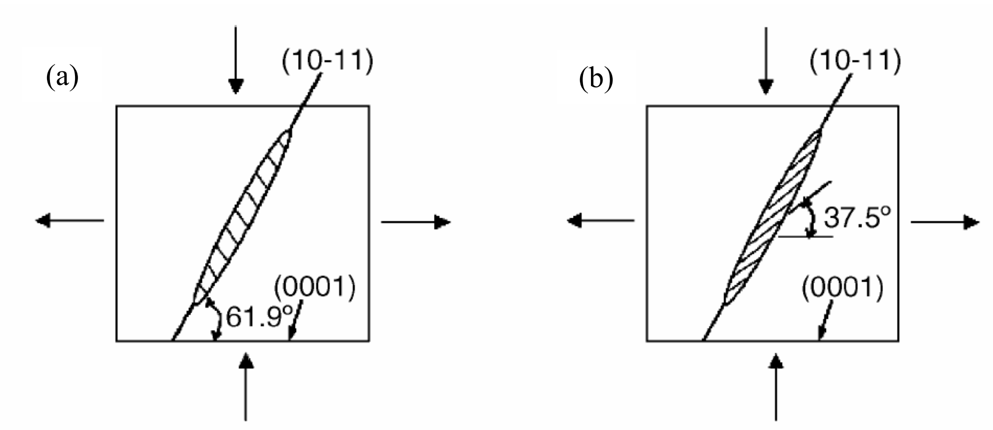

Fig. 2-7 Schematic diagram showing the $\{10\bar{1}1\}$ - $\{10\bar{1}2\}$ double twinning process: (a) twinning on $(10\bar{1}1)$ reorients the (0001) basal plane by 61.9°; (b) this is followed by 37.5° from its original position in the untwined matrix [25].

Factors that influence the activation of twinning are wildly investigated, such as the deformation temperature, strain rate, grain size, orientation of the grains, existence of second phase, and so on. At low temperatures (< 200°C) Mg exhibits a strong tendency for mechanical twinning [26]. Grain size plays a key role in the activation of twinning, while it is still on debating about the critical grain size [27]. Generally, in the small sized grains the stress concentration at grain boundary is higher than in the larger grains, so that the twinning nucleation is easier, but the high internal strain obstructs the growth of twin. As a consequence, the twinning evolutions are observed practically in a large grained microstructure. The influence of the grain size on the flow stress of extruded AZ31with grain size varying between 3 and 23μm in compression tests was examined by Barnett and his co-workers [28]. It can be deduced from the experimental results that approximate the twinning transition from slip to twinning for AZ31 for grain size in the range 2 to 400 μm at temperature between 100 and 400°C for strain rates between 0.01 and 10 s^{-1}. Investigations on the tensile-compression tests in the as-extruded AZ31 showed that the mechanical anisotropy was closely related to generation of $\{10\bar{1}2\} < 1\bar{1}01 >$ twin, and the mechanical anisotropy decreased with increasing temperature, which was attributed to reduction in twin generation at elevated temperature. Results also indicated that texture strongly affected the mechanical anisotropy because twin generation was enhanced when the (0002) plane was strongly distributed parallel to the compressive testing direction, and the mechanical anisotropy was reduced by grain refinement, which was due to the suppression of twin generation.

2.3 Equal channel angular pressing/extrusion

Severe plastic deformation

Processing by severe plastic deformation (SPD) can be defined as those metal forming procedures in which a very high strain is imposed on a bulk material without the introduction of any significant change in the overall dimensions of the solid and leading to the production of exceptional grain refinement so that, typically, the processed bulk solids have 1000 or more grains in any sections [29]. Many different SPD processing techniques have been proposed, developed and evaluated till now. These techniques include, as shown in Fig. 2-8, ECAP [30, 31], high pressure torsion (HPT) [32, 33], repetitive corrugation and straightening (RCS) [34, 35], accumulative roll-bonding (ARB) [36, 37], multi-directional forging [38], twist extrusion [39], cyclic-extrusion-compression [40], friction stir processing(FSP) [41] and submerged friction stir processing (SFSP) [42]. All of these processing techniques are capable of introduction large plastic straining and significant microstructural refinement in bulk materials. Some of these techniques, such as ECAP, HPT, and ARB are already well established methods for producing ultra-fined grains.

Equal channel angular pressing

ECAE/ECAP was invented in 1972 and first described by V. M. Segal and his co-workers [43]. At that time, intensive researches were performed at the Physical Technical Institute Academy of Sciences of Byelorussia, Minsk in the former Soviet Union on development and applications of ECAP technology to different materials science and industrials problems [44]. In the early 1990s with changing interest in ultra-fine and nano-structural materials, ECAP became the object of considerable efforts and researches on this severe plastic deformation (SPD) process has greatly increased. Of these various procedures, equal-channel angular pressing is an especially attractive processing technique for several reasons. Firstly, it can be applied to fairly large billets so that there is the potential for producing materials that may be used in a wide range of structural applications. Secondly, it is a relatively simple procedure that is easily performed on a wide range of metals and, except only for the construction of the die, so processing by ECAP uses equipment that is readily available in most laboratories. Thirdly, ECAP may be developed and applied to materials with different crystal structures and many materials ranging from precipitation-hardened alloys to intermetallics and metal-matrix composites. Fourthly, reasonable homogeneity is attained through most of the as-pressed billet provided the pressings are continued to a sufficiently high stain. Fifthly, the process maybe scaled-up for the pressing of relatively large samples. These various attractive features have led to many experimental studies and new developments in ECAP processing over the last decades.

2.3.1 Principles of ECAP

There is large number of reports describing the fundamental process of materials flow during ECAP [30-32, 45-47]. The typical ECAP die is schematically shown in Fig. 2-9, two identical channels intersecting at an internal angle of Φ and an out curvature angle of Ψ. Φ angle of 90º is widely used as well as 60 º and 120 º. The strain imposed on the billet during ECAP is significantly affected by the value of Φ and Ψ. Three conditions are shown in Fig. 2-10, where in case of Ψ= 0 º, Ψ= π-Φ, and an arbitrary angle between them. The strain is estimated by assuming a well lubricated sample as that frictional effect is neglected. For the situation Ψ= 0 º, as shown in Fig. 2-10 (a), a small square element in the entrance channel, labelled abcd, passes through the theoretical shear plane and becomes distorted into the parallelogram labelled a'b'c'd'. It can be shown from first principle that the shearing strain γ, is given by [45] as follows,

$$\gamma = 2\cot\left(\frac{\Phi}{2}\right) \qquad \text{(Eq. 2-5)}$$

Using the same approach for Fig. 2.2 (b), when Ψ= π-Φ,

$$\gamma = \phi \qquad \text{(Eq. 2-6)}$$

and a similar analysis for Fig. 2.2 (c) leads to the general equation

$$\gamma = 2\cot\left(\frac{\Phi}{2}+\frac{\Psi}{2}\right) + \Psi \cos ec\left(\frac{\Phi}{2}+\frac{\Psi}{2}\right) \qquad \text{(Eq. 2-7)}$$

Finally, the equivalent strain after N passes, ε_N , can be expressed in a general form of

$$\varepsilon_N = \frac{N}{\sqrt{3}}\left[2\cot\left(\frac{\Phi}{2}+\frac{\Psi}{2}\right) + \Psi \cos ec\left(\frac{\Phi}{2}+\frac{\Psi}{2}\right)\right] \qquad \text{(Eq. 2-8)}$$

Four basic processing routs in ECAP are summarized in Fig. 2-11, in which route A the sample is pressed without rotation, in route B_C the sample is rotated by 90° in the same sense (either clockwise or counter clockwise), in route B_A the sample is rotated by 90° in alternate direction between consecutive passes, and in route C the sample is rotated by 180° after each pass. Various combinations of these routes are also possible, such as combing routes B_C and C by alternating rotations through 90º and 180º after each pass, but in practice the experimental evidence obtained to now suggests that these more complex combinations lead to no additional improvement in the mechanical properties of the as-pressed materials [48].

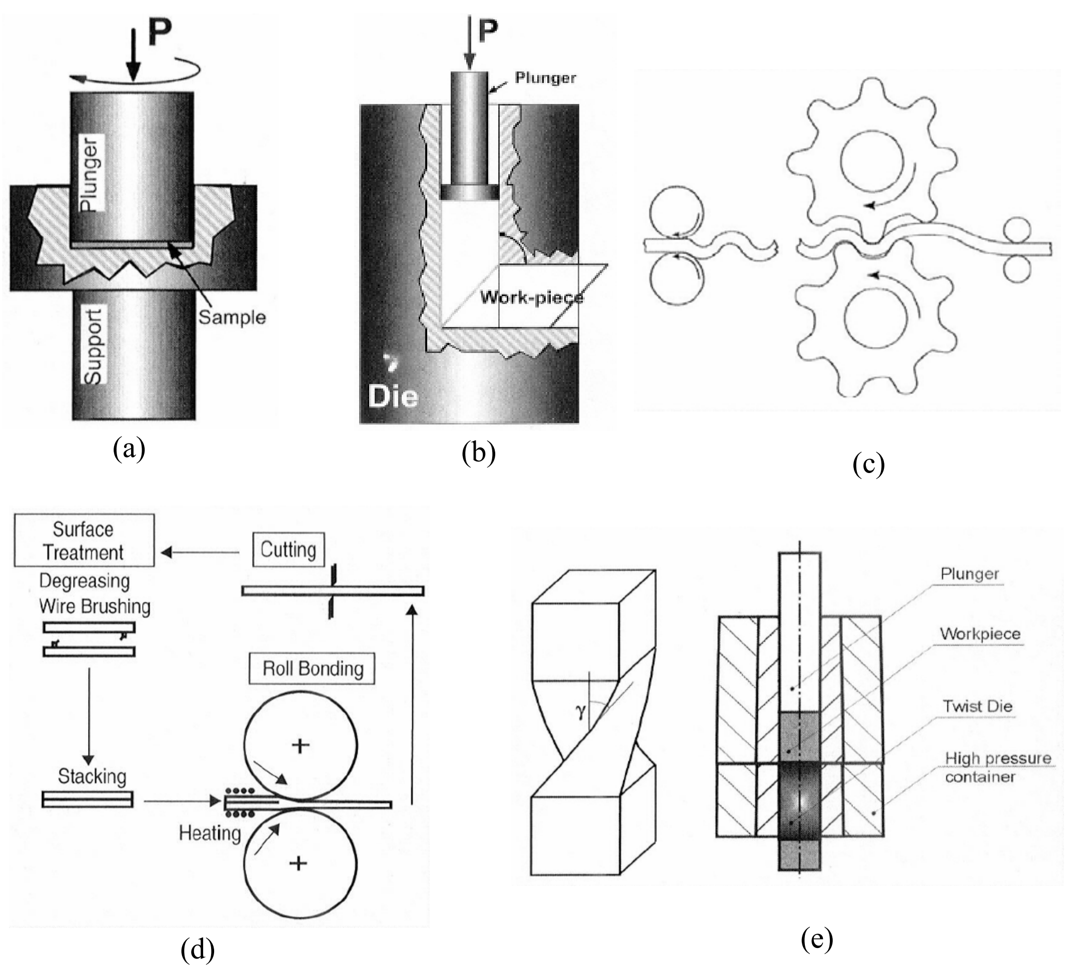

Fig.2-8 Current SPD technologies: (a) High pressure torsion , HPT; (b) Equal channel angular extrusion/pressing, ECAE/ECAP; (c) Repetitive corrugation and straining, RCS; (d) Accumulative roll-bonding, ARB; (d) Twist extrusion, TE.

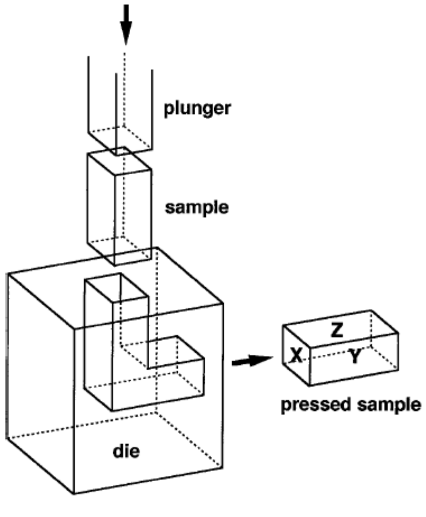

Fig.2-9 Schematic shows the typical ECAP die: the X, Y and Z designate the transverse plane, flow plane and longitudinal plane, respectively [46].

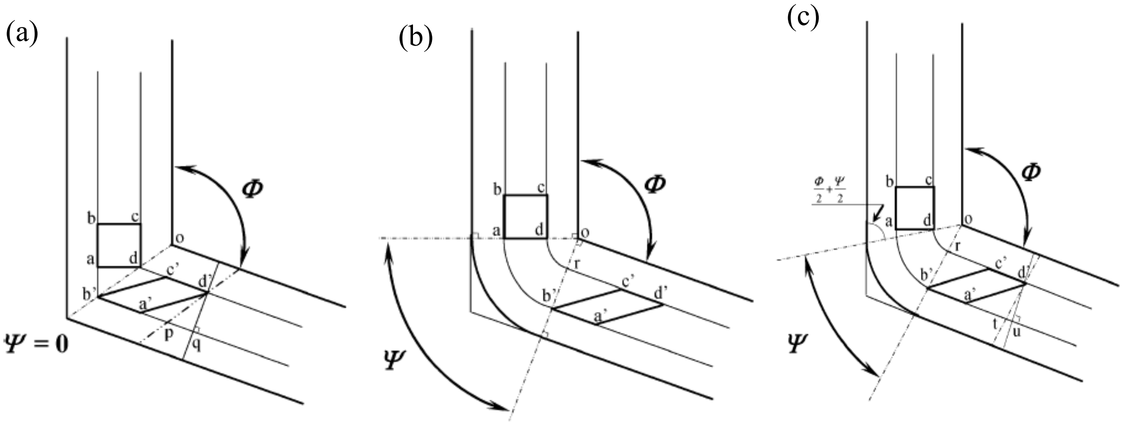

Fig. 2-10 Three conditions of Ψ for calculation of the imposed strain, (a) $\Psi = 0^\circ$, (b) $\Psi = \pi - \Phi$, and (c) an arbitrary angle $\Psi = 0^\circ$ and $\Psi = \pi - \Phi$ [45].

Different slip systems associated with these four processing routes are described and systematically shown in Fig. 2-12, where the X, Y and Z planes correspond to the three orthogonal planes shown in Fig. 2-9. A theoretical shearing plane with an angle of 45 º to Z plane was formed after 1 pass processing. With furthering pass processing, the shearing plane intersects with an angle of 90 º at each consecutive pass with route A, while via route C the shearing plane continue on the same plane but in a reversed direction. It is apparent that route B_C and C are redundant strain processes which part of strain can be cancelled during the following pass processing. Further implications of these shearing systems by Furukawa et al. [50] are illustrated in Fig. 2-13, where a cubic element was used to describe its distortion vied on three orthogonal X, Y and Z planes from 1 pass to 8 passes. With route A, for example, the cubic element appears compressed when viewed in the X plane after a single passage through the die and tends to be a line after 8 passes; and the cubic was gradually elongated along the 45º direction to the extrusion vied on Y plane while there was no distortion vied on Z plane. It can be found that the shearing characteristics of route Bc is similar to route C, in which the cubic element is restored after 4n passes in route Bc and 2n passes in route C (n is an integer).

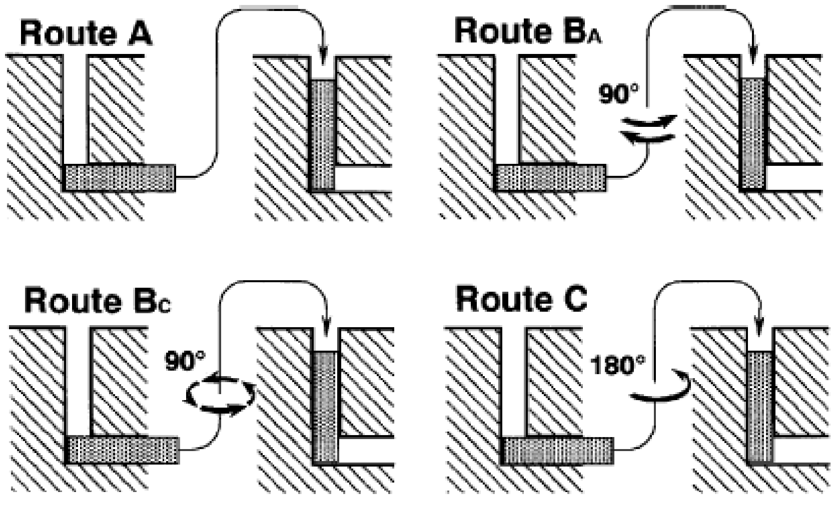

Fig.2-11 Four fundamental processing routes in ECAP [47].

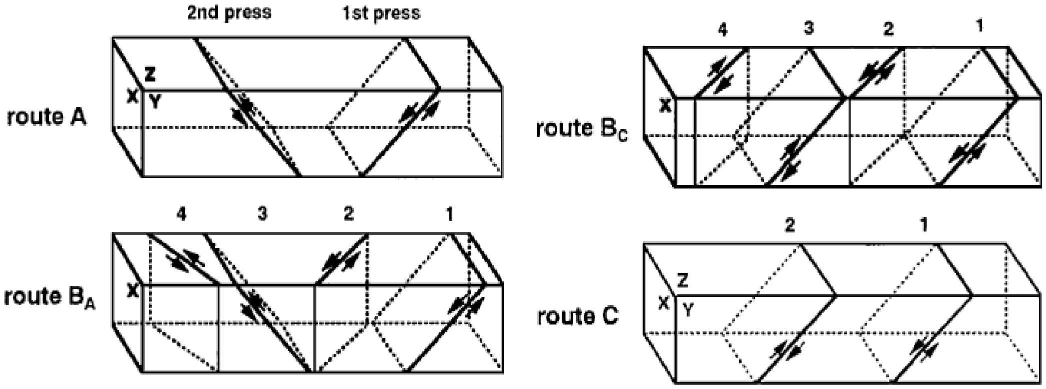

Fig. 2-12 Schematic illustration of the slip system of four processing routes for consecutive pass [49].

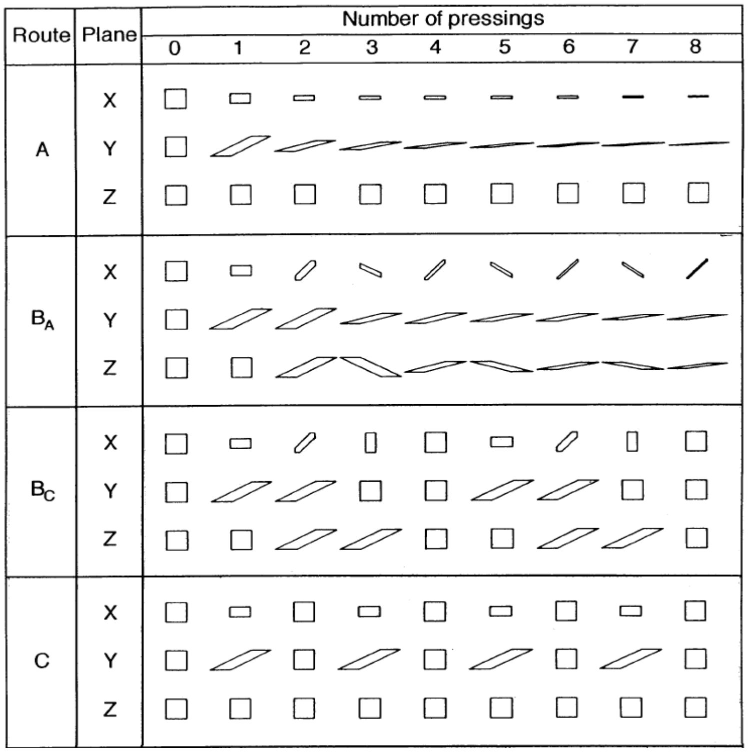

Fig. 2-13 The distortions introduced into cubic elements when viewed on the X, Y, and Z planes for processing routes A, B_A, B_C and C from 1 pass to 8 passes [50].

2.3.2 Factors influencing ECAP processing

Similar as the normal extrusion or rolling deformation, several factors influence the deformability and the microstructures of the as ECAP-processed materials billets. These factors fall into three distinct categories. Firstly, the factors are associated with the die design, such as the values of the angles within the die Φ and at the outer arc of curvature Ψ. Secondly, these factors are related to the ECAP processing regimes where some maybe varied with different experimentalist, such as the processing temperature, the speed of pressing, the lubrication condition of die and the absence or presence of any back-pressure. Thirdly, the inner factors of the pressed materials such as the ideal crystal structure and its deformability, and most important is the real crystallographic structure. It has been proved that cubic structural metals like Al, Fe and Cu are easily to be deformed, while Mg, Ti and some intermetelics are hard to ECAP at low temperature.

The channel angle, Φ, is the most significant experimental factor since it dictates the total strain imposed in each pass, as described by the Eq. 2-8, and thus it has direct influences on the nature of the as-ECAP-processed microstructure. Φ angle of 90º is widely used, and there are still some investigations with die angle of 60º and 120º for some easier and harder to pressed materials [51, 52]. The main purpose using different channel angles is to make the hard to deform materials ECAP, but it seems that there is generally little or no attempt to make any significant comparison between the results obtained when using dies having different channel angles. ECAP processing of pure Al with different channel angles of 90º, 112.5º, 135º and 157.5 º by Nakashima and his colleagues showed that the total cumulative strain is not the important factor in determining the microstructure in ECAP but rather it is important to ensure that a very high strain is imposed on each separate pass [53]. This means in practice that the ideal ECAP die will have a channel angel close to 90º and it implies also that similar microstructures cannot be attained with other techniques like conventional extrusion using multiple passes, where small incremental strains are imposed in each separate pass [54]. Since the strain imposed increases with the decrease of channel angle, it may be advantageous to perform ECAP using a die channel Φ < 90º. However, high pressure or high temperature is required to successfully press the billet without any introduction of cracks. Hence, it is reasonable to conclude that a channel angle of 90º represents the optimum configuration for an ECAP die [29, 50, 55].

The angle at the out curvature of the two channels Ψ has a great influence on the deformation modes and the materials flow of the billet during ECAP though it plays a minor role on in determining the imposed strain on the sample. Researches have shown that the lesser shearing zone was greatly related to the angle Ψ [56 -58]. A deformation dead zone will occurre in ECAP through the use of FEM modeling and many of these analyses incorporate an evaluation of the signification of the curvature angle of Ψ [55, 58]. FEM simulation with the die angle of 90º and different Ψ of 0º, 45º and 90º indicated that with the increase of Ψ=45º to 90º, the lesser sheared zone in the bottom region of the work piece increases [55]. It should also be noted that the round out curvature angle not only reduces the overall shearing deformation but also intensify the strain in homogeneity. An optimized corner angle on the inner surface where the two channels intersects was proposed by Luis Perez [59], but from a practical view it is very difficult to machine such a die which having a equal curvature angle at outer and inner surface of the two channels. Therefore, as suggested by Valiev and Langdon that the most promising approach is to construct a die with a channel angle of Φ = 90º, with an out angle of curvature of Ψ ≈ 20º and with no arc of curvature the inner point of intersection of the two parts of the channels [29].

The processing temperature is a key factor that controls the ECAP processing, which plays an important role in optimization of grain size and the grain boundary conditions. Detailed investigation of the influence of temperature on ECAP processing of Al alloys was carried out by Yamashita et al. [60]. Two important trends were revealed by this experiment. First, there was an increase in the equilibrium of grain size with increasing of temperatures. Second, it was concluded that from the an examination of the SAED patterns that the fraction of low-angle grain boundaries increased with increasing of temperature, which maybe due to the faster rates of recovery at the higher temperature that lead to an increasing annihilation of dislocations within the grains and a consequent decrease in the numbers of dislocations absorbed into the sub-grain walls. The tendency for larger grains or sub-grains to form at the higher temperatures was confirmed in several investigations [61-63]. It has been generally concluded that the smallest grain size and the highest fraction of high-angle boundaries can be obtained by lowering the pressing temperature.

Processing speed is also a controllable factor that may influence the equilibrium size of the ultra fine grains formed via ECAP. ECAP of pure Al and Al-1%Mg alloy at ram speeds from 10^{-2} to 10 mm s^{-1} was investigated by Berbon et al. [64]. The results indicated that the pressing speed had no significant influence on the equilibrium size of the ultra-fined grains formed by ECAP but, since recovery occurs more easily when pressing at the slower speeds, these lower speeds produce more equilibrated microstructures. And the subsequent tensile testing at room temperature showed that the strength increased with the increasing numbers of pass through the die, the tendency to saturate after $N \approx 4$ passes and the lack of any dependence on the pressing speed. However, temperature variation and the subsequent effect on the microstructure are related to the processing speed, especially for the materials which have strong dynamic recrystallization behavior.

There is an increasing interest in using back-pressure during ECAP processing in recent years. It has been revealed that an important advantage in imposing a back-pressure is that it leads to a very considerable improvement in the workability of the processed billets [65, 66]. For example, ECAP processing of Cu without back-pressure it is generally found that cracks appear on the surface of the billet, while the same billet remains integral without any cracking even after 16 or more passes when imposing a back-pressure of only 30 MPa [66]. Another important advantage of back-pressure is the visible enhancement introduced in the uniformity of the metal flow during the ECAP operation. As has mentioned above, a dead zone occurs due to the outer angle of die, especially in easily strain hardening materials, there is also a change in the shape of the deformation zone from a pure shear line to a fan shape within the die. However, the application of a back-pressure leads to a filling of this outer corner, and a consequent removal of the dead zone, regardless of the character of the materials strengthening. Furthermore, the deformation zone becomes closer to a localized shear band which is typical of a rigid perfectly- plastic body [67]. The influence of back-pressure on the degree of grain refinement was investigated in Cu with an imposed back-pressure of 400 MPa [68]. The experimental results showed the grain size was reduced from 0.24µm without any back-pressure to 0.18 µm with back-pressure. It is still not clear that whether this additional grain refinement is a consequence of the change in the metal flow pattern during the processing operation or whether the applied pressure directly influences the processes of micro structural evolution. More works are required to evaluate the role a back-pressure with different kinds of materials [69, 70].

2.3.3 Characteristic features of the ECAP-processed Mg and its alloys

The most significant advantage of ECAP is to refine the grains of wide range of materials. However, as has been discussed above, the characteristics of the as-pressed microstructures are influenced by several variables which has summarized above. Efforts are still undertaken to achieve excellent microstructures after ECAP leading to exceptionally high strength and good mechanical properties by optimizing the processing parameters or selecting the materials. ECAP processing of Mg is more attractive because of the increasing trend of global researches on Mg alloys. And most important is that Mg has the h.c.p. crystallographic crystal structure which could have different features after ECAP comparing to cubic structure metals. The uniform microstructures and as well as the improved properties of the ECAP-processed Mg is increasingly investigated and reported recently. ECAP of Mg-Al (addition of Ca or Mn) (AZ31, AZ61, AZ91, AZ80), Mg-(Zn)-Zr (ZK60, AM80), Mg-Li (Al), Mg-Ni, Mg-Zn-Y-Zr et al. are widely investigated.

ECAP of AZ31 was successfully performed up to 8 passes at temperatures as low as 100°C with the application of a back-pressure [71]. Results showed that the grain size was significantly refined to much finer than 1 μm after 4 passes at 150 °C and 4 passes at 100 °C. The microstructure was initially not uniform with a 'bimodal' grain size distribution but became increasingly homogeneous with further ECAP passes. A bi-modal grain structure consisting of large deformed and small recrystallized grain fractions were also obtained in ECAP-processed ZK60 [72]. And the fraction of small grains increases with the number of passes and the decrease of ECAP temperature, the grain structure was no longer bi-modal but was rather uniform and fine-grained after 8 passes. A two-step ECAP processing was successfully applied to control the microstructure and mechanical properties of the AZ31 alloy by lowing the processing temperature to 453K [73]. The ultra-fined grain of 0.5 μm has been obtained, and both the ductility and strength of the alloy were improved significantly after the processing, which can be explained by grain refinement as well as incomplete dynamic recovery and recystallization during the processing. Processing by ECAP up to 8 passes at 623 K has produced a grain size of about 3.5 μm in the cast Mg-4.3wt.%Zn-0.7wt.%Y Mg alloy. Experiments showed that the coarse eutectic quasicrystalline phases were broken and dispersed in the alloy. Experimental results of the ECAP processing of the as-extruded super-light Mg-14%Li-1%Al alloy at room temperature showed that the grains of the matrix β phase (matrix phase, solid solution of Mg in bcc Li lattice) were substantially refined, with the mean size decreasing from 60 μm to 200 nm. And the distribution of the α precipitates (solid solution of Li in hcp Mg lattice), which were embedded in the β grains, and the ternary MgLiAl2 phase coexisting with the α precipitates were homogenized by ECAP [74].

Tensile testing at 523K and 623K reveals the enhanced ductility in the ECAP-processed Mg-Zn-Y alloy, with maximum elongations of about 200% and 600%, respectively [75]. A maximum elongation of 1320% at 473K using an initial strain rate of 3.3×10^{-4} s^{-1} in the extrusion plus ECAP-processed AZ61 was obtained by Miyahara and his co-workers [76]. A negative slope of tensile yield stress versus square root of grain size $d^{-1/2}$ in the ECAP-processed as-extruded AZ61 at 275°C was observed and explained by the gradual transition of the texture during repetitive ECAP to control the grain size; and the significant increase of ductility was mainly attributed to the modification of texture during ECAP, which the basal poles were close to 45° from the extrusion and transverse directions using EBSD observation [77].

It should be mentioned from the above documentation of the current researches on the ECAP processing of Mg alloys that the grains can be greatly refined to sub-microns. But it is still difficult to obtain the nano-grains in Mg alloys by ECAP even after 16 or more passes processing, which is thought to be mainly due to the relatively high processing temperature that makes the recovery or grain growth easily. An attractive feature of the ECAP-processed Mg is the development of uniform texture, which the orientation of the basal planes can be modified by using different processing routs. It could be primarily concluded that the ductility of Mg alloys after ECAP can be greatly improved. Hence, ECAP processing of Mg can be adopted as a pre-deformation for the following deformation or production. Researches on normal extrusion or rolling deformation before or after ECAP have shown that both of the strength and ductility can be improved [78]. Micro-gear extrusion was successfully performed on ECAP-processed AZ31 Mg alloys with fine grain size by Kim and his co-workers [79]. Their results showed that high strength gears could be produced by using ECAP combined with the extrusion method: ECAP refines the microstructure while direct extrusion restores the ECAP-processed texture to the original state before ECAP. Hence, combination of ECAP with other deformation techniques is a candidate method to obtain the desirable microstructures [80].

2.4 Textures developed in Mg and its alloys

2.4.1 General description on texture

A large number of polycrystalline materials, both manmade and natural, display preferred orientation of crystallites. Preferred orientation of the crystallites, called crystallographic texture or texture, is an intrinsic feature of metals, ceramics, polymers and rocks and has an influence on physical properties such as strength, electrical conductivity, magnetic susceptibility, light refraction and wave propagation, particularly in the anisotropy of these properties. The directional characteristics of many polycrystalline materials were first recognized not in metals but in rocks and were described as 'texture'. In the 20th century texture was largely pursued by metallurgist and later in polymers, earth science and ceramics [81]. The texture may undergo evolution during casting, processing, deformation, welding, as well as heat treatment. The relation of the materials properties to this preferred alignment of the crystallites in certain sample direction is one of the key problems in materials science for the optimisation of properties.

Descriptions on texture characterization and measurement technology have been systematically done by the pioneer on texture analysis, Prof. H.J. Bunge, in his books or published papers [82, 83]. The texture is represented as the orientation distribution of crystallites. For describing the orientation distribution two of coordinate systems are introduced. As a coordinate system fixed in sample, K_A = (X, Y, Z), the exterior shape is generally used, e.g. normal, transverse and rolling direction in case of rolled sheet. The second coordinate system for each crystal is defined, K_B = (X', Y', Z'), which is fixed in the crystal-axes, e.g. $[10\bar{1}0]$, $[11\bar{2}0]$ and [0001] in case of hexagonal structure. These two coordinate systems are related to each other with an orientation g as following,

$$K_B = g \cdot K_A \qquad (K_A \text{———} \; g \longrightarrow K_B) \qquad \text{(Eq. 2-9)}$$

i. e. the K_A is transformed by g into the K_B. The orientation g can be presented in some different ways, for example, by Miller-indices ($h\ k\ i\ l$) [$u\ v\ t\ w$] or by Euler angles {φ_1, Φ, φ_2}, as shown in Fig. 2-14. The indices ($h\ k\ i\ l$) stand for a crystallographic plane perpendicular to plate-normal direction and [$u\ v\ t\ w$] is for the crystallographic direction parallel to rolling direction, in case for a rolled plate. The Euler angles are defined by rotation angles around 3 fixed axes, by which the crystal coordinate system becomes matched with the sample coordinate system. The crystal coordinate system is firstly rotated about the Z'-axis through the angle φ_1, then about the X'-axis (in its new orientation) through Φ and, finally, once again Z'-axis (in its new orientation) through the angle φ_2 [82].

The Euler angles are represented in three-dimensional Cartesian coordinate, so called Euler space, Fig. 2-15. Each point in the Euler space indicates an orientation g, that is to say, the entirety of all crystals in the Euler space is called as texture. Again, the texture is defined in general as the volume-distribution of certain crystals (orientations) in the Euler space.

$$f(g) = \frac{dV(g)/V}{dg}, \qquad \text{(Eq. 2-10)}$$

$$g = \{\varphi_1, \Phi, \varphi_2\} \qquad \text{(Eq. 2-11)}$$

In the above definition, orientation distribution function (f(g), ODF) is given as the multiple of the random distribution (m.r.d.), i.e. $f_{random} = \oint f(g)dg = 1$, (Eq. 2-12)

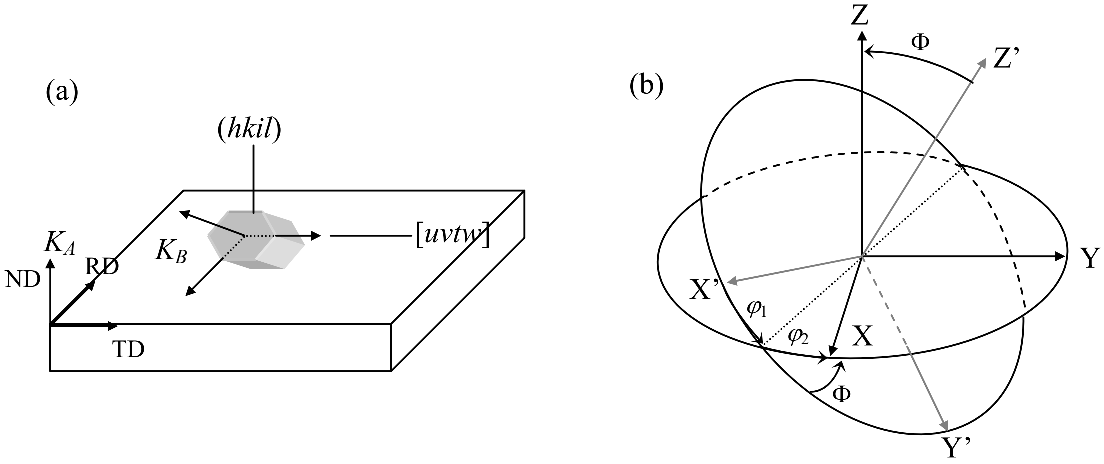

Fig. 2-14 Two methods for representing the orientation *g,* (a) Miller indices and (b) Euler angle, a coordinate system is presented as Z-axis and its X-Y plane for sample; Z' and X'-Y' plane for crystal.

One can represent the ODF in a reduced Euler space, when the crystal- and sample symmetries are considered. The whole Euler space is given in range of 0° ≤ φ_1 ≤ 360°, 0° ≤ Φ ≤ 180° and 0° ≤ φ_2 ≤ 360°, without consideration on the symmetry. However, after consideration on the both symmetries, ODF needs to be given only in the asymmetric unit in Euler space. The reduced Euler space for hexagonal structured materials is shown in Fig. 2-15. In most case ODF is calculated from measured pole density distribution functions (P_{hkl} (α,β), pole figures), called pole figure inversion. A pole figure represents the probability of lattice plane poles in different sample directions. The probability is contoured on a sphere, relative to sample coordinate and projected on a plane, using equal area or stereographic projection. Pole figures can be directly measured by some diffraction techniques, e.g. laboratory X-ray, neutron and synchrotron diffraction facilities. However, the coverage of such measurements is often incomplete and the measured pole figures have non-normalized intensities. More importantly, the pole figures provide the orientation distribution in 2-dimension so that some of different orientations appear on a same domain. These are the reasons why ODF is preferred for a quantitative representation and analysis.

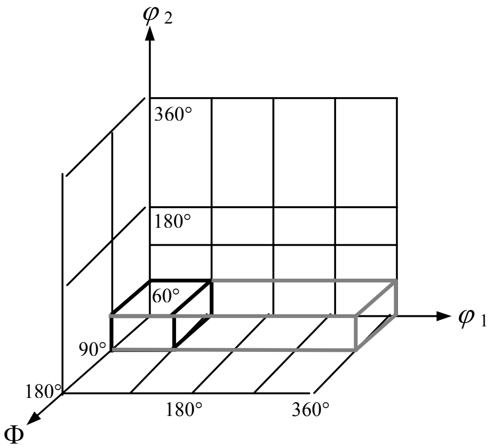

Fig. 2-15 The Eulerian space with {φ_1, Φ, φ_2} .

The mathematical ways for ODF calculation has described by many authors, Bunge and Roe [82, 84] introduced the series expansion method and Matthies [85] used WIMV (Williams-Imhof-Matthies-Vinel) method. In the present work the series expansion method by Bunge is used. In Bunge's formalism, a pole figure is expanded in a series of spherical harmonic function;

$$P_{hkl}(\alpha,\beta) = \sum_{l=0}^{l_{\max}} \sum_{\nu=1}^{N(l)} F_l^{\nu}(hkl) \cdot \dot{k}_l^{\nu}(\alpha,\beta) \qquad \text{(Eq. 2-13)}$$

$$F_l^{\nu}(h\,k\,l) = \int_{\alpha=0}^{\pi/2} \int_{\beta=0}^{2\pi} P_{hkl}(\alpha,\beta) \cdot \dot{k}_l^{*\nu}(\alpha,\beta) \quad \sin\alpha \; d\alpha \;\; d\beta \qquad \text{(Eq. 2-14)}$$

where, *l* is series expansion degree, *F* are the pole figure coefficients, and *k* are the symmetrized spherical harmonic functions. The *F* coefficient can be calculated by the integration of the experimentally achieved pole density distribution, pole figure inversion, in this case the normalized pole figure intensities are used;

The above equations show how the unknown *C* coefficients of the orientation distribution function can be calculated from the known *F* coefficients. Once the *C* coefficients are known, the ODF expanded in series of generalized spherical harmonics can be achieved;

$$f(g) = f(\varphi_1 \; \Phi \; \varphi_2) = \sum_{l=0}^{l_{may}} \sum_{\mu=l}^{M(l)} \sum_{\nu=l}^{N(l)} \; C_l^{\mu\nu} \cdot \ddot{T}_l^{\mu\nu}(\varphi_1 \; \Phi \; \varphi_2) \qquad \text{(Eq. 2-15)}$$

$$F_l^{\nu}(h\,k\,l) = \frac{4\pi}{2l+1} \sum_{\mu=1}^{M(l)} C_l^{\mu\nu} \cdot \dot{k}_l^{*\mu}(h\,k\,l) \qquad \text{(Eq. 2-16)}$$

In the Eq. 2-13 to 2-16, the symbol '*' denotes the complex conjugate, and the dots over the harmonic functions denote the symmetrization of the functions. M(*l*) and N(*l*) are the number of independent values for each expansion degree, *l*, after the sample- and crystal symmetrizations, respectively.

For representing the texture of hexagonal materials the ODF has been used not very frequently used, but the texture representation by measured $\{10\bar{1}0\}$ and/or (0002) pole figures. It is attributed not only the fact that more measured pole figures are needed for the calculation, but also the fact that the qualitative texture analysis has brought sufficient results. Though it is fact that both pole figures support important information and fast insight for the simple extrusion or rolling texture, ODF gives more detailed information in three-dimensional space for the quantitative and qualitative texture analysis, as above mentioned. Moreover, ODF can be directly used as an input for calculating the properties and for simulation works, since ODF itself is a mathematical function that includes the distribution of all crystal-orientations in whole sample directions.

2.4.2 Measurement of texture

Interpretation of textures has to rely on a quantitative description of the orientation characteristics. Two types of preferred orientations are distinct: the lattice preferred orientation or texture and the shape preferred orientation. They are not correlated in many cases, for example, in a rolled cubic metal the grain shape depends on the deformation rather than on the crystallography. Many methods have been used to measure the preferred orientation. Optical method has been extensively applied by geologists, using the transmission light microscope equipped with a universal stage to measure the orientation of morphological and optical direction in individual grains [86]. Metallurgists have used a reflection light microscope to determine the orientation of cleavages and etched pits [87]. With the advances in image analysis, optical methods can be automated.

Today diffraction techniques are most widely used to measure the crystallographic preferred orientation. X-ray diffraction with a pole-figure goniometer is a routine method. For some applications synchrotron x-ray provides unique opportunities. Neutron diffraction offers some distinct advantages, particularly for bulk materials and non-destructive measurement. Electronic diffraction method using TEM or SEM is gaining interesting, because it can correlate the microstructures and neighbouring conditions with textures.

There are two distinct ways to measure orientations. Usually one measures an average over a large volume of a polycrystalline aggregate. A pole figure collects a sum of lattice plane reflection signals from a large number of crystals. In the pole figure, one lost spatial information (for examples the orientations of the neighbours), and also the local position of grains (such as how x, y, and z-axes of individual crystallites correlate). The second method is to measure the orientations of individual crystal either by diffraction or optical techniques. This is a direct measurement of the orientation distribution and a map of the microstructure in individual grain. Individual grain mapping gives the relationship with neighbours and the position of the grain. But compared to the bulk methods, the statistics of such measurements are limited.

X-ray diffraction

X-ray diffraction was first employed by Wever (1924) to investigate preferred orientations in metals, but only with the introduction of the pole figure goniometer and did it became a quantitative method (Schultz, 1949). Bragg's Law for monochromatic radiation is applied. The principle is simple: in order to determine the orientation of a give lattice plane, *hkl*, of a single crystallite, the detector is first set to the proper Bragg angle, 2θ of diffraction peak of interest, then the sample is rotated in a goniometer until the lattice plane *hkl* is in the reflection condition (i.e. the normal to the lattice plane or diffraction vector is the bisectrix between incident and diffracted beam), as shown in Fig. 2-16. In the case of a polycrystalline material, the intensity recoded at certain sample orientation is proportional to the volume fraction of the crystallites with their lattice planes in reflection geometry. Determination of texture can be done on a sample of large thickness and a plane surface on which x-ray are reflected, or on a thin slap that can be penetrated by x-ray. Because of the defocusing effects as the flat sample surface is inclined against the beam, variations in the irradiated volume and absorption intensity corrections are necessary, particularly in reflection geometry. In reflection geometry only incomplete pole figures can be measured, usually to a pole distance of 80° from the samples surface normal.

Synchrotron diffraction

Conventional x-ray tubes produce a of relative low intensity. A powerful new tool for texture research is synchrotron radiation. In a synchrotron a nearly parallel high intensity beam of x-ray with broad spectrum can be produced. The unique advantages of high intensity, small bean size and a free choice of wavelength open a wide range of new possibilities. Synchrotron diffraction images recorded by CCD detectors almost instantaneously display the presence of texture expressed in systematic intensity variations along Debeye-Scherrer rings. Synchrotron analysis is valuable for compounds with weak scattering (e.g. polymers and biomaterials) and for investigating local texture variants. Other applications are in-situ observations of textures evolution during deformation, heat treatment and other experimental conditions.

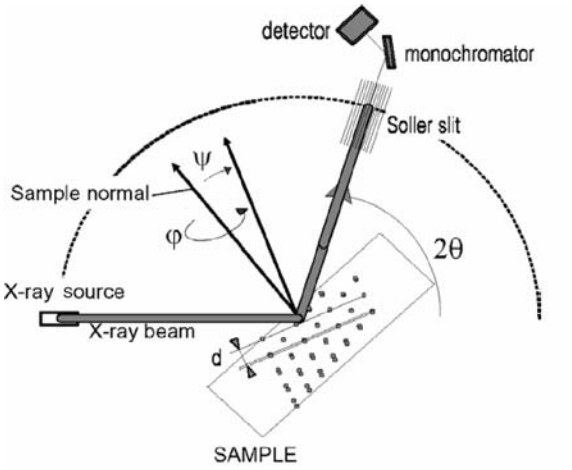

Fig. 2-16 Geometry of a pole figure goniometer equipped with Soller slit and monochromator. Bragg's Law applies to lattice plane. The sample is rotate about an axis that is perpendicular to the surface.

Neutron diffraction

Neutron diffraction analysis is almost as old as the pole figure goniometer. It was first applied by Brockhouse (1953) in an attempt to determine the magnetic structure of nickel. Neutron diffraction texture analysis is done either at reactors with a constant flux of thermal neutrons, or with pulsed neutrons at spallation sources. The wavelength distribution of thermal neutrons is a broad spectrum with a peak at 1-2Å, similar to x-rays. Non-destructive bulk texture analysis on nearly un-prepared materials is one of the greatest advantages by neutron diffraction [88]. Neutron diffraction is also an efficient tool for measuring multi-phasesed materials [89]. The main advantage due to a high penetration is the measurement of complete pole figure. A disadvantage of neutrons is that the interaction of neutrons with material is low, and long counting time is required. Weak interaction is also a great advantage because it provides high penetration and low absorption, making neutrons suitable for bulk texture investigations of large sample volumes. Because of the low absorption, environmental stages (heating, cooling and deformation) can be used for in-situ observation of textures evolution. Neutrons are also sensitive to measure the orientation of magnetic dipoles, but though this was the original incentive of Brockhouse, to today no satisfactory magnetic pole figures have been measured.

Conventional neutron texture equipment at a reactor uses monochromatic radiation produced with a single crystal monochromator. A goniometer rotates the sample to cover the entire orientation range, analogous to an x-ray goniometer. To improve efficiency position-sensitive detectors (PSD) have been used that record 2θ spectrum with many peaks simultaneously. With the advent of the pulsed neutron source it has become customary to use a polychromatic neutrons and a detector system that can identify the energy neutrons by measuring the time-of -flight (TOF).

Transmission electron microscope

The TEM offers excellent opportunities to study textural details in fine grained materials. TEM not only provides information about orientation, but also about grain shape and, more important, about dislocation microstructures that indicate the activated deformation mechanism. There are many applications of Kikuchi patterns for orientation analysis, and the indexing procedure has been automated.

Scanning electron microscope

Local orientations can be also measured by SEM and this technique is becoming popular. Unlike TEM, SEM is not restricted to the thin areas along the edge of a hole, but enables crystal orientations to be determined on surfaces of considerable extent. Interaction of the electron beam with the uppermost surface layer of the sample produces electron back-scatter diffraction patterns (EBSPs or EBSD) that are analogous to the Kikuchi patter in TEM. EBSPs are captured on a phosphor screen and recorded with a low intensity video camera or CCD device. The sample is translated using a high precision mechanical stage or sample locations are reached by beam deflection in increments as small as 1 μm. At each position an EBSP is recorded. Back-scattered electrons are converted to light with a phosphor screen; this signal is transformed into a camera. The digital EBSP is then entered into a computer and indexed. Sample coordinates, crystal orientation, parameters describing the pattern quality and a parameter evaluating the pattern match are recorded. Then the sample is translated to the next position and the procedure is repeated. A spatial resolution of less than 0.4 μm can be reached on a SEM equipped with a field emission gun.

Briefly, the optimal choice of texture measurements depends on many variables, such as availability of equipment, material to be analyzed and data requirements. For routine metallurgical practice and many other applications in materials science and geology, an x-ray pole figure goniometer in reflection geometry is generally adequate. It is fast, easily automated and inexpensive both in acquisition and maintenance. While in geological samples and ceramics, x-ray diffraction is therefore generally limited to single phase aggregates of orthorhombic or higher crystal symmetry. Synchrotron –rays are used for in-situ experiments at high pressure and temperature, generally of very fine-grained materials. Texture changes can be recorded in real time. With neutron diffraction bulk samples rather than surfaces are measure, coarse-grained materials can be characterized, environmental cells (heating, cooling, and deformation) are available and angular resolution is better than for an x-ray pole figure goniometer because no defocusing occurs. It is possible to measure complex polyphase composites with many closely spaced diffraction peaks. Neutron diffraction data analysis is rather complex and requires considerable expertise form the user, and access to facilities is limited. There are limitations for samples with many lattice defects with EBSPs. But this technique has already proved to be essential in the study of recrystallization and grain growth in metals upon annealing, as well as grain fragmentation upon plastic deformation.

2.4.3 Textures in Mg and its alloys

Textures in hexagonal structural materials have attracted significant interest over the years because of the use of Zr alloys for cladding of nuclear reactor fuels, Ti alloys for structural materials in aerospace and aircraft industry [90]. Because of economical reasons the research activities on the Mg had received less attention since the end of the world war, then the texture of these alloys were discussed mainly as for a tool comparing with other hexagonal metals. In what follows, the typical textures observed in hexagonal materials, especially in Mg are reviewed.

Fiber texture

A fiber texture is presented with a maximum at the $<10\bar{1}0>$ position, in a way such that all the basal planes normal directions <0001> are perpendicular to the extrusion axis. This is termed as the 'cylindrical texture', commonly observed in extruded rods of hexagonal materials. The inverse pole figures standing for possible fiber-textures in Mg and Mg-alloys are presented in Fig. 2-17. Pure Mg shows the ring type fiber-texture, Fig. 2-17 (a), in which all crystallographic directions in basal plane can be laid parallel to extrusion direction. $<10\bar{1}0>$ fiber-texture was observed in Mg alloys with Al, Mn and Zn after extrusion over

450°C, while Mg alloy with 2 wt. % of Mn showed a double fiber-texture with $\langle 10\bar{1}0\rangle$ + $\langle 11\bar{2}0\rangle$, as shown the inverse pole figure in Fig. 2-17 (d) [90].Variation between different types of fibers is dependent on the alloying elements and their composition, deformation temperature as well as deformation methods. Hydrostatic extrusion of AZ31 at different temperatures and as well as cooling method showed that twinning plays a role before or during dynamic recrystallization, leading to an increase in the <10.0> pole intensity between 225 ºC and 250 ºC whereas no further changes were obtained at 300 ºC; and air cooling leads to a decrease in the <10.0> pole density as well as an increase in the <11.0> pole density [91]. However the comprehensive explanations on the mechanism for these variations are still lacked.

<0001> fiber-texture, in which basal plane normal aligned parallel to deformation axis, has been observed after compression (upsetting) of an extruded rods along the extrusion direction, in this case the inverse pole figure seems similar with Fig. 2-17 (e). This large rotation of crystallites, about 90°, relates strongly with activation of $\{10\bar{1}2\}$ $\langle 1\bar{1}01\rangle$ twinning. Additionally, the development of strong <0001> fiber-texture was reported after physical vapor deposition of various Mg alloys [92].

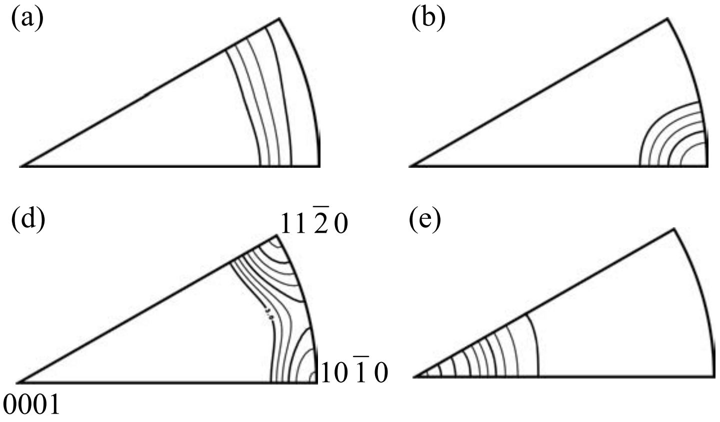

Fig.2-17 Examples of fiber-type texture in Mg and its alloys (inverse pole figures in the main deformation direction).

Rolling texture

The textures of rolled hexagonal metals can be categorized roughly into three groups according to their c/a–ratio, namely materials with c/a rations greater than, approximately equal to, and less than the ideal value of 1.633. The simulated (0002) and $(10\bar{1}0)$ pole figures for the rolled sheet textures with three different c/a categories are schematically illustrated in Fig. 2-18, respectively. Metals and alloys with c/a rations approximately equal to the ideal c/a ration of 1.633, such as Mg tend to form basal fiber textures during rolling, as shown in Fig. 2-18 (a). The origin of such textures maybe understood in terms of the slip systems operating on basal planes. Metals and alloys with c/a rations above the ideal, such as Zn (1.856) and Cd (1.885), tend to exhibit textures with basal poles tilted ±15-25° away from the normal direction toward the rolling direction. Such textures are due to the combination of basal slip and large-scale twinning. Finally, the metals and alloys, processing c/a less than 1.633 such as Zr (1.589) and Ti (1.587), tend to form textures with basal poles tilted ±20-40° away from the normal direction toward the transverse direction, in which slip on prismatic planes is largely responsible for textures of these types with basal pole spreading.

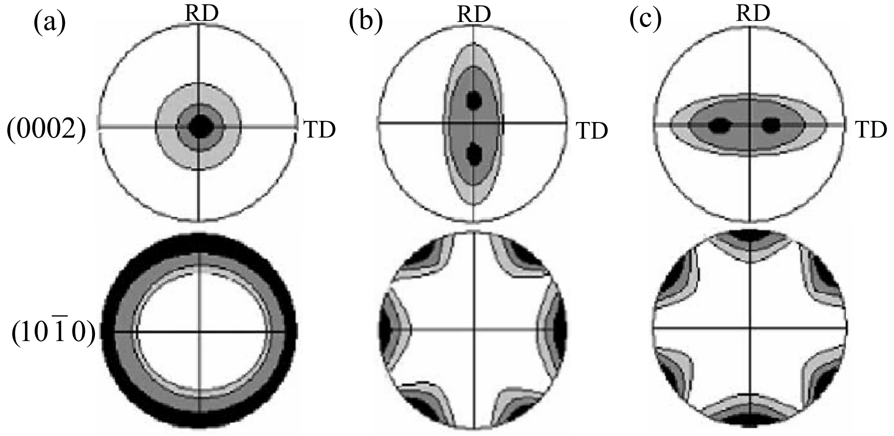

Fig. 2-18 Simulated textures in h.c.p. metals with different c/a ratios of (a) c/a ≈ 1.633 (Mg, Co), (b) c/a > 1.633 (Zn, Cd), and (c) c/a < 1.633 (Ti, Zr) [90].

In general, the c/a ratio reflects the activation of the different slip systems. However, this crude approach is not always applicable in Mg alloys. A rather crude approach because many of other factors influence on the texture development, e.g. strain rate, temperature and chemical composition etc. All those factors have direct or indirect relation with activity of a deformation mode, and the large variety of deformation textures in hexagonal metals are actually due to the fact that the different combinations of slip and/or twinning modes cause the different textures. For this reason many researchers have made an effort for disclosing the relationship between deformation modes and texture.

Texture obtained by x-ray diffraction in the cold rolled AZ31 at room temperature showed two fibers, representing double peaks in basal pole tilted ±15° from the normal direction to the rolling direction [93]. Further texture modeling with a viscoplastic Taylor model indicated that a combination of <***a***>- basal, <***a***>- prismatic, <***c+a***>- pyramidal slip systems can better form this cold rolling texture. Texture evolution during large strain hot rolling of an AM60 alloy with an initial random texture has been studied by optical microscopy and *X*-ray diffraction [94]. Results indicated that a double-peak (slightly off-basal) texture develops during large strain hot rolling texture intensity increases with growing thickness reductions. The appearance of this texture is attributed to the increasing activity of non-basal <***c+a***> -slip. Cross-rolling of AZ31 produced the (0002) basal texture exhibiting a low intensity and a narrow spread of basal planes to rolling direction [95]; and a reduction of anisotropy in the width-direction strain and the thickness-direction strain was found and attributed to activation of prismatic <***a***> slip and pyramidal <***a* + *c***> slip originated from the texture modifications.

Asymmetric hot rolling of AZ31 by S. Kim showed that the sheets exhibited a texture gradient, where the intensity of (0002) basal textures decreased from the upper surface through the center to the lower surface [96]. Followed by subsequent annealing the intensity of (0002) components was reduced significantly throughout the thickness and the grains were fined possibly by discontinuous recrystallization.

Recrystallization texture

Recrystallization shares several common characteristics as phase transformation in the replacement of deformed materials by the nucleation and growth of recrystallized grains, both can lead to changes in texture. The principal difference are (i) the 'nuclei' during recrystallization are regions that already exist in the deformed microstructure; and (ii) recrystallization does not lead to precise orientation relationship between the deformed and recrystallized materials in contrast to the case of phase transformation [97]. Although there might be some approximate orientation relationship present in-between the recrystallized and parent grains, there have been no reports in making quantitative predictions for recrystallization texture based on such approximated orientation relationships. It should also note that recrystallization does not always lead to changes in texture, particularly when a large volume fraction of second-phase particles are present.

Texture evolution during annealing of an as-rolled AZ31 with through-thickness texture gradient which basal and $\{11\bar{2}0\}$ prismatic components predominate in the outer surfaces, basal, $\{10\bar{1}0\}$ and $\{11\bar{2}0\}$ prismatic components predominate basal in the mid-layer was investigated [98], results indicated that upon annealing normal grain growth occurred in the mid-layer and secondary recrystallization started in the outer surfaces, leading to a homogeneous $\{11\bar{2}0\}$ texture throughout the thickness.

ECAP texture

It is recognized that ECAP offers the potential to induce unique deformation texture and that these textures could have a significant impact on the material properties. Conventional processing of Mg alloys results in a very limited range of texture possibilities. ECAP offers materials a range of possible textures to explore, which may enhance different properties and applications. There have been a number of studies of ECAP texture development focused on cubic metals, such as Al, Cu and Fe, and their alloys. And also there are increasing researches on hexagonal metals such as Ti, Mg and Zr and their alloys. Investigations have shown that textures developed during ECAP are greatly related to not only the die geometry but also the processing parameters, such as processing temperature, processing route, initial texture, number of processing pass, and et al. [99-101].

Effect of alloying additions and processing routs on texture evolution on Mg alloys after ECAP processing has been systematically investigated by S. R. Agnew and his co-workers [102]. The measured (0002) and $(10\bar{1}0)$ pole figures are shown in Fig. 2-19, in which indicated that ECAP tends to produce a certain class of textures regardless of the alloy or processing route. This class of textures was defined as <0001> fiber textures. However, the orientation and strength of the <0001> fiber texture was strongly affected by alloying additions and processing histories, that was to say, the AZ alloys tend to develop textures with <0001> highly inclined (~55°) to the extrusion axis, while ZK alloy develops a primary fiber closer to 90° and along with secondary <0001> fibers, either normal to the flow plane or within the flow plane. Texture development of the rod extruded AZ61 after ECAP processing via route Bc from 1 pass to 8 passes was investigated by W. J. Kim and his colleagues [103]. The measured $(10\bar{1}0)$ and (0002) pole figures are illustrated in Fig. 2-20, in which the texture of the as-extruded ED // $<10\bar{1}0>$ fiber texture was rotated by about 10º around the normal direction to ED-TD plane after 1 pass, and the tilting angle and the maximum intensity in (0002) pole figure varied with the following pass processing.

It can be found that the ECAP-processed Mg texture has common feature as a basal fiber with its fiber axis variation to the samples' coordination system [102-104]. There is still unclear of the formation mechanism of this texture.

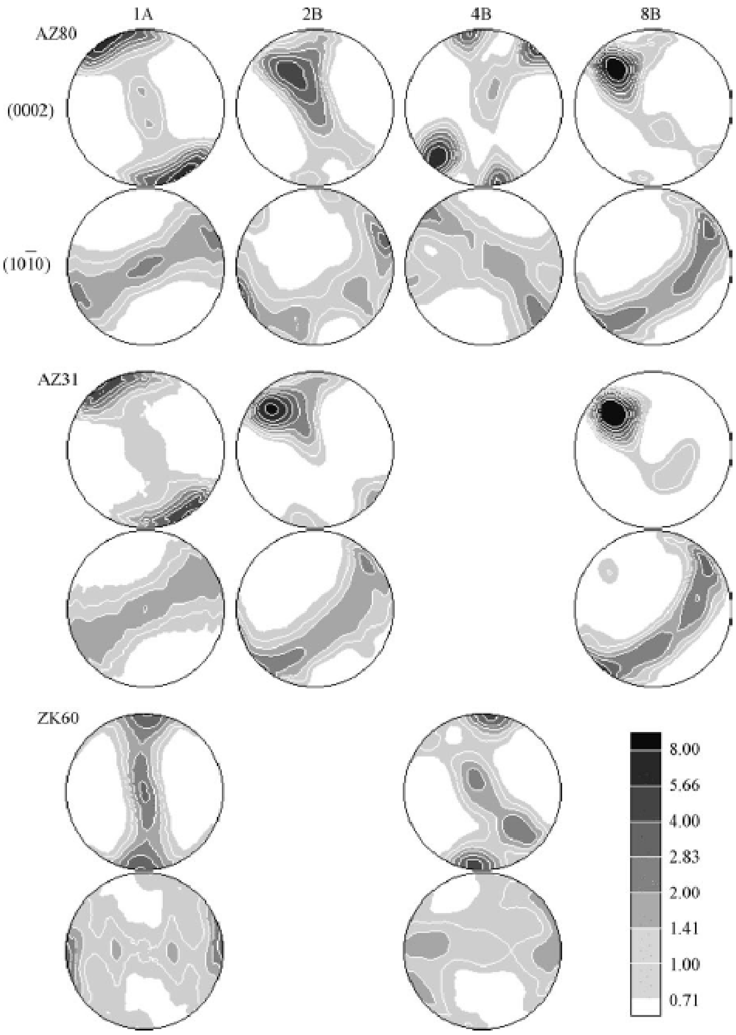

Fig. 2-19 (0002) and $(10\bar{1}0)$ showing the ECAE textures after 1 pass and 2, 4 and 8 passes by route Bc for alloys AZ80, AZ31 and ZK60. the extrusion direction is to the top [102].

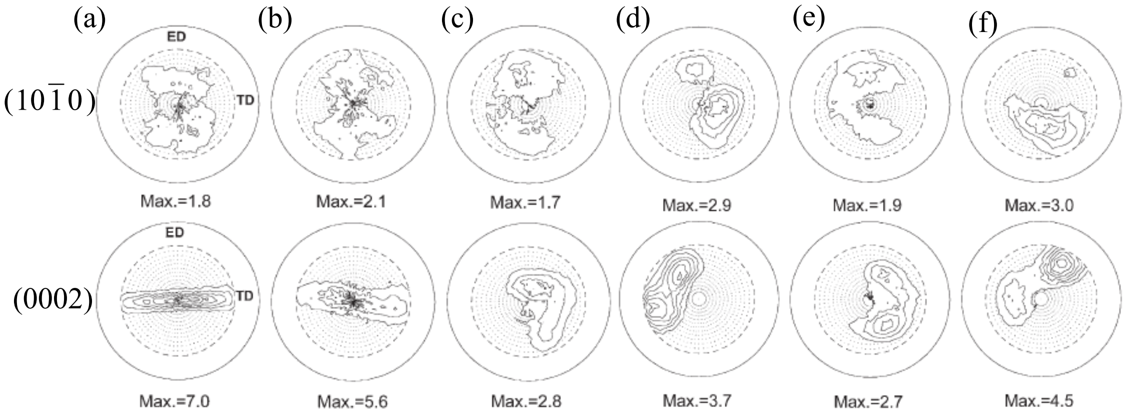

Fig. 2-20 $(10\bar{1}0)$ and (0002) pole figures of (a) the rod extruded and ECAP-processed AZ61 by route Bc of (b) 1 pass, (c) 2 passes, (d) 3 passes, (e) 4 passes, and (f) 8 passes [103].

2.5 Simulation of deformation texture

Deformation of polycrystal is a very complicated heterogeneous process. When an external stress is applied to the polycrystal, it is transmitted to individual grains. Dislocations move on slip systems, dislocations interact and cause ‘hardening’, grains change their shapes and orientations, thereby interacting with their neighbors and caused local stress that need to be accommodated.

Polycrystal plasticity and texture development of polycrystalline materials are characterized by the variety of active deformation modes present in each grain, non-negligible twinning activity accompanied by a substantial fraction of grain reorientation, and highly directional grain interactions. Polycrystal plasticity simulation can be used to help determine the physical processes that cause different alloys within a class to exhibit distinct deformation behavior. There are two extreme assumptions. Taylor suggested that in modeling plastic deformation, straining could be partitioned equally among all crystals [105]. In the Taylor model, high stresses are required to activate slip systems, even in unfavorable oriented grains, and the model is known as an upper bound model. In contrast to the Taylor hypothesis, origin suggested by Sachs that all crystals in a polycrystal can be required to exhibit identical stress, given that their behavior is rate-dependent at the slip system level. With the Sachs approach only the most favorable slip systems are activated, and therefore, stresses are low. This approach is known as a lower bound model. Molinari et al. has developed the viscoplastic self-consistent (VPSC) for modeling the heterogeneous deformation of highly anisotropic polycrystals [106, 107]. Another modeling approach is to employ finite element methodologies to compute deformations of aggregates of polycrystals. In this case local heterogeneity can be taken into account, particularly if grains are discretized with many elements. It can be concluded that the essential characteristic of a model is the assumption (or criterion) for relating the strain and stress in a crystallite with those in outer boundary, and therefore, for determining the possible deformation modes.

2.5.1 Taylor model

Due to the great practical interest in the large deformation polycrystalline theory, a lot of efforts have been devoted to different approximate theories. The most popular one, the Taylor approach, assumes the plastic strain in each grain is identical to the macroscopic plastic strain which has been developed by Taylor, Bishop, Hill and Bunge. Usually, at large deformations, the elastic deformation is neglected. This Taylor approach has been often successful in the prediction of texture evolutions for both f.c.c. and b.c.c. materials.

The Taylor assumption of uniform strain throughout the polycrystal aggregates ensures automatically the strain compatibility at grain boundaries and provides an upper bound solution of the stress. Under a loading condition, some possible sets of slip systems in a crystallite can be chosen by which the same strain value is resulted with that of outer boundary. From this condition a set of linear simultaneous equations was achieved, in which 5 independent strain components are linked to the shear stains caused by chosen slip systems, (one of the strain components is dependent variant from the condition of no dilation during plastic deformation; $d\varepsilon_{11} + d\varepsilon_{22} + d\varepsilon_{33} = 0$). Since numerous combinations of slip systems are existent for fulfilling the above condition, a second assumption is necessary. Taylor suggested that the preferred set of slip systems will be that for which the sum of the shears on each system is resulted in the minimum value, called principle of minimum (internal) plastic work which the rate of internally dissipated frictional work is minimal. In this case the done work, dW, during an increment of plastic strain is written;

$$dW = \sum_{S=1}^{n} \tau_C^S \left| d\gamma^S \right| = \min. \qquad \text{(Eq. 2-17)}$$

where, $d\gamma^S$ denotes the shear strain on s'th slip system in total n slip systems. From Eq. 2-17, in general, 5 solutions for values of γ^S can be achieved by assuming the same τ_C for all slip systems.

Bishop and Hill [108] suggested a different approach, based on the principle of maximum (external) plastic work, for solving the above problem. They used the yield criterion of single crystals, in which the active stress status is that gives the maximum work in polycrystal. In other words, the stress state (σ_{ij}) relevant for the maximal work can be determined during the plastic deformation with given strain status (ε_{ij}), Eq. 2-18.

$$dW = \sum_{i}^{3} \sum_{j}^{3} \sigma_{ij} \varepsilon_{ij} = \max. \qquad \text{(Eq. 2-18)}$$

Van Houtte [109] was proved that the Taylor's and Bishop-Hill's approaches give always the same solution. Therefore, the calculation using one of both models is called altogether TBH method. The TBH model shows difference to the real state due to its too strict condition for maintaining the strain compatibility (full constraint model, FC). For this reason modification of this model was proposed by Honneff and Mecking. Following their observation of the heavily stretched grains after rolling, they assumed that 1~2 shear strain components in 5 external strain components can be freely deformed, so called relaxed constraint model (RC). Fig. 2-21 shows the resulting shape changes under FC and RC conditions. Since all of 5 strain components are fixed in case of FC model, 5 active slip systems can be determined. On the other hand, in the RC model reduced number of slip systems can be determined. When the normal direction is corresponding to 33 and the rolling direction to 11 in Fig. 2-21, the case of relaxation in $d\varepsilon_{13}$ is called lath model, while the case of relaxation in $d\varepsilon_{13}$ and $d\varepsilon_{23}$ is called pancake model. Even though the strain compatibility at grain boundary is lost by the relaxations, the rolling texture can be better simulated by using the RC than FC method.

TBH approach doesn't provide unique solutions, that is, there are several possible sets of slip systems fulfilling the TBH assumptions (uncertainty of solution). For predicting the mechanical properties this problem is not considerable, because any sets of deformation modes give the same quantity of the done work, i.e. same value of Taylor factor (= σ_{ij}/τ_C, reciprocal of Schmid's factor). Since the rotation of crystallite is differently calculated by different sets of slip systems, many researchers have proposed for getting unique solution. Honneff and Mecking used the average value for all possible slip systems, and Van Houtte proposed the linear programming method for random choice of any arbitrary set. Canova et al. [110] suggested the strengthening of CRSS as a function of strain rate sensitivity, so called strain rate sensitivity model. Following them, CRSS of each slip system varies after an increment of deformation so that only one set of slip systems can be determined. Details on the strain rate sensitivity model will be described with VPSC formulation.

Full constraints (FC) approach imposes the same deformation to every grain, irrespectively of its anisotropy. Though such assumption assures the fulfillment of compatibility, it disregards any possible departure of the grain deformation from the average, so implicitly stating the surroundings dictate the grain deformation, independently of the relative anisotropies. The relaxed constraints (RC) formulation, on the other hand, allows for some of the strain components in the grain to differ from the average ones, but such relaxation is based on grain shape and stress continuity considerations and not in the relative stiffness of grain and matrix.

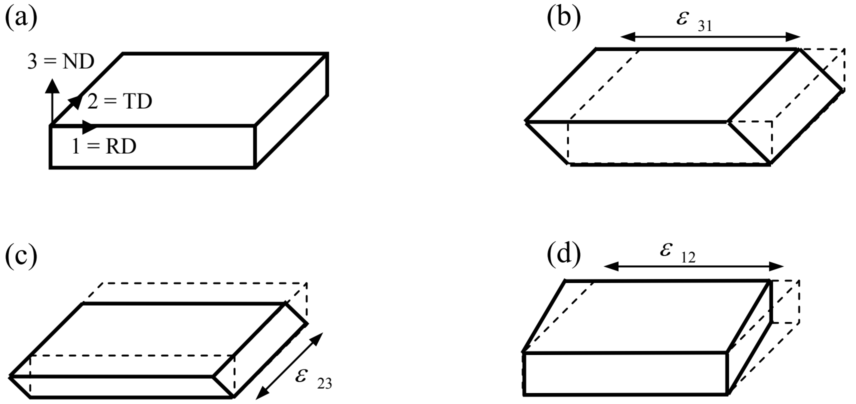

Fig. 2-21 Shape changes of an originally cubic grain deformed under (a) full constraints and (b), (c) and (d) relaxed constraints condition with free shears of, ε_{31} , ε_{23} and ε_{12} , respectively.

2.5.2 Sachs' model

The basic assumption in Sachs' model is that the all crystallites in polycrystal aggregates are under same stress status with that in outer boundary. That is, all crystallites are treated as they can be deformed freely in any direction. A plastic strain can be initiated when resolved shear stress, τ^S , on a slip system 'S' reaches the critical value, τ_C^S, (CRSS for the slip system), which can be written as following;

$$\tau^S = \sum_i^3 \sum_j^3 r_i^S v_j^S \sigma_{ij} = \sum_i^3 \sum_j^3 m_{ij}^S \sigma_{ij} = \tau_C^S \qquad \text{(Eq. 2-19)}$$

Eq. 2-19 shows the Schmid's law generalized for complex stress status, where r_i^S , v_i^S and σ_{ij} are the slip plane normal, slip direction and stress in outer boundary in terms of crystal coordinate system, respectively, the product of the r_i^S and v_i^S is Schmid's tensor m_{ij}^S .

According to this model it can be maintained the stress continuity at grain boundary, but no strain compatibility because each crystallite has different strain values. Moreover the basic assumption itself is contradictory to the fact that stress status should be different in each crystallite in accordance with its orientation. Consequently, the Sachs' model is applicable only for deformation in a single crystal.

2.5.3 Viscoplastic self-consistent (VPSC) model

As has been described in the above section that FC and RC approaches have their limitations, it is necessary to consider the strength of grain-matrix interaction which is neither completely rigid nor fully compliant. This is significant for non-cubic crystal plasticity, primary for the reason of limited number of primary slip systems. An important contribution in this respect is the VPSC model proposed by Molinari et al. [106] and developed by many authors

(Lebensohn, Tome, Bolmaro, Beyerlein, etc.) [111-113]. The basic assumption in VPSC models is that each grain is treated as an inhomogeneous inclusion embedded in the homogeneous effective medium (HEM) represented by the polycystal. HEM has a uniform property and the proper modules, for relating stress to strain, so as to provide the same overall stress-strain response as the real heterogeneous material. This treatment of each grain allows local equilibrium and compatibility to be satisfied, while maintaining computational efficiency. In process solving the interaction between grain and HEM is using the Eshelby approach, in which the deformation of the grains has to fulfil the local stress equilibrium and compatibility. This leads to an interaction equation that linearly relates stress and strain in the grain with the overall stress and strain rate of the effective medium. The condition that the average of stress and strain rate over all the grains has to be consistent with the equivalent macroscopic magnitudes makes for the self-consistent resolution of the problem.

Formulation of VPSC

Constitutive relation

In the VPSC model five dimensional tensors of deviatoric stress and strain rate are use d to present the plasticity.

$$\sigma_k' = \sqrt{2}\left(\frac{(\sigma_{33}-\sigma_{11})+(\sigma_{33}-\sigma_{22})}{2\sqrt{3}}, \frac{\sigma_{22}-\sigma_{11}}{2}, \sigma_{23}, \sigma_{13}, \sigma_{12}\right) \qquad \text{(Eq. 2-20)}$$

$$\dot{\varepsilon}_k = \sqrt{2}\left(\frac{(\dot{\varepsilon}_{33}-\dot{\varepsilon}_{11})+(\dot{\varepsilon}_{33}-\dot{\varepsilon}_{22})}{2\sqrt{3}}, \frac{\dot{\varepsilon}_{22}-\dot{\varepsilon}_{11}}{2}, \dot{\varepsilon}_{23}, \dot{\varepsilon}_{13}, \dot{\varepsilon}_{12}\right) \qquad \text{(Eq. 2-21)}$$

The resolved shear stress, τ_r^s and strain rate associated with the shear rate $\dot{\gamma}^s$ on S'th system are given by,

$$\tau_r^s = m_k^s \sigma' \qquad \text{(Eq. 2-22)}$$

$$\dot{\varepsilon}_k = m_k^s \dot{\gamma}^s \qquad \text{(Eq. 2-23)}$$

The shear rate induced in (s) by given applied stress is described by a rate sensitive criterion, which formally amounts to assuming a non-linear viscous response,

$$\dot{\gamma}^S = \dot{\gamma}_0\left(\frac{\tau_r^S}{\tau_C^S}\right) = \dot{\gamma}_0\left(\frac{m_j^S \sigma_j'}{\tau_C^S}\right)^n \qquad \text{(Eq. 2-24)}$$

where $\dot{\gamma}_0$ is a reference rate, τ_C^S is a threshold stress (linked to τ_r^S), n is the inverse of the rate sensitivity given by,

$$n = m^{-1} = \left(\frac{\ln(\sigma_2/\sigma_1)}{\ln(\dot{\varepsilon}_2/\dot{\varepsilon}_1)}\right)^{-1} \qquad \text{(Eq. 2-25)}$$

when n >> 1 the activity of the system is negligible unless τ_r^S is very close to τ_C^S, and the later can be identified with the CRSS characteristic of the Schmid criterion. Each grain of the polycrystal is described by means of a rate sensitive constitute law of the form when replacing Eq. 2-24 in Eq. 2-23,

$$\dot{\varepsilon}_K = \dot{\gamma}_0 \sum_{s=1}^{S} m_K^S \left(\frac{m_j^S \sigma_j'}{\tau_C^S}\right)^n \qquad (K=1, 5) \qquad \text{(Eq. 2-26)}$$

where the sum is carried over the complete set of systems in the grain. Eq. 2-26 describes the response of single grain in non-linear way, and it consists of 5 equations with 10 unknowns (5 elements for strain rate an 5 for deviatoric stress). Within the FC or RC approaches, the system is solved for each grain separately. Since the underlying assumption is that the grain 'following the dictates' of the polycrystal, both schemes give good results when dealing with materials of low plastic anisotropy. In VPSC approach the strain and the stress in each grain are coupled with the average strain rate and the average stress in the polycrystal, so providing another set of 5 equations.

Following Hutcinson, Eq. 2-26 is rewritten in a pseudo-liner form

$$\dot{\varepsilon}_i = \{\dot{\gamma}_0 \sum_{s=1}^{S} \frac{m_i^S m_j^S}{\tau_C^S} \left(\frac{m_k^S \sigma_k'}{\tau_C^S}\right)^{n-1} \} \sigma_j' = M_{ij}^{c(\sec)}(\sigma')\sigma_j' \qquad \text{(Eq. 2-27)}$$

where $M_{ij}^{c(\sec)}$ are the secant visco-plastic compliance moduli of the grain. Except for n=1, $M_{ij}^{c(\sec)}$ depends on the stress and the validity of the linear relation between stress and strain rate is limited to the precise point $\sigma' - \dot{\varepsilon}$ that describes the grain state. A linear relation valid in the vicinity of the point $\bar{\sigma}' - \dot{\varepsilon}$ is obtained by doing a Taylor expansion of Eq. 2-27 around $\bar{\sigma}'$, which defines the tangent modulus $M^{c(tg)}$ and the back extrapolated term $\dot{\varepsilon}^0$ by,

$$\dot{\varepsilon}_i = \frac{\partial \dot{\varepsilon}_i}{\partial \sigma'}\Big|_{\sigma'=\bar{\sigma}'} + \dot{\varepsilon}_i^0 = M_{ij}^{c(tg)}(\bar{\sigma}')\sigma_j' + \dot{\varepsilon}_i^0 \qquad \text{(Eq. 2-28)}$$

where the tangent modulus $M^{c(tg)}$ and back-extrapolated term $\dot{\varepsilon}^0$ are defined by

$$M_{ij}^{c(tg)} = \frac{\partial \dot{\varepsilon}_i}{\partial \sigma_j'}\Big|_{\sigma'=\bar{\sigma}'} = n M_{ij}^{c(\sec)} \qquad \text{(Eq. 2-29)}$$

$$\dot{\varepsilon}_i^0 = (1-n) M_{ij}^{c(\sec)}(\bar{\sigma}')\bar{\sigma}' \qquad \text{(Eq. 2-30)}$$

At the macroscopic level, the overall polycrystal response is assumed to be described by constitutive equations similar to Eq. 2-27 and Eq. 2-28. If $\dot{E}$ and $\bar{\Sigma}'$ are the polycrystal strain rate and deviatoric stress respectively, the secant relation can be written as

$$\dot{E}_i = M_{ij}^{(\sec)}(\bar{\Sigma}')\bar{\Sigma}_j' \qquad \text{(Eq. 2-31)}$$

while the tangent relation, valid also in the vicinity of $\bar{\Sigma}'$, adopts the form

$$\dot{E}_i = M_{ij}^{(tg)}(\bar{\Sigma}')\bar{\Sigma}_j' + \dot{E}_i^0 \qquad \text{(Eq. 2-32)}$$

with

$$M_{ij}^{(tg)} = \frac{\partial \dot{E}_i}{\partial \Sigma_j'}\Big|_{\Sigma'=\bar{\Sigma}'} \qquad \text{(Eq. 2-33)}$$

Hutchinson demonstrates that the polycrystal tangent and secant moduli fulfil the same relation derived earlier for the single crystal moduli

$$M_{ij}^{(tg)} = nM_{ij}^{(\sec)} \qquad \text{(Eq. 2-34)}$$

The tangent approximation of Eq. 2-32 amounts to regarding the aggregates as HEM having a visco-plastic compliance $M^{(tg)}$ plus a reference strain rate $\dot{E}^0$, whose behaviour is identical to the overall behaviour of the polycrystal. Each grain, characterized by the visco-plastic compliance $M^{C(tg)}$ plus a reference strain rate $\dot{\varepsilon}^0$, is in turn regarded as an inhomogeneity embedded in the HEM, which disturbs the stress filed locally when a uniform stress is applied to the HEM. The problem of an inhomogeneity embedded in a homogeneous matrix being acted upon by the uniform stress ∑' at infinity can be solved using the Eshelby formalism.

The inclusion formalism

Within Eshleby's approach, the inhomogeneity is replaced by an 'equivalent inclusion' having the same moduli $(M^{(tg)}, \dot{E}^0)$ of the polycrystal but undergoing a fictitious transformation strain rate $\dot{\varepsilon}^*$ that induces the same stress in the inclusion and in the surroundings as the inhomogeneity does. The condition that $\dot{\varepsilon}^*$ has to fulfil within the domain of the inclusion is, after Eq. 2-28 and Eq. 2-32, that

$$\dot{\varepsilon}_k = M_{kl}^{(tg)}\sigma_l^{'} + \dot{E}_k^0 + \dot{\varepsilon}_k^* \qquad \text{(Eq. 2-35)}$$

The deviations of strain rate and stress between in grain and polycrystal are defined by

$$\tilde{\dot{\varepsilon}} = \dot{\varepsilon}_k - \dot{E}_k \qquad \text{(Eq. 2-36)}$$

$$\tilde{\sigma}_l^{'} = \sigma_l^{'} - \Sigma_l^{'} \qquad \text{(Eq. 2-37)}$$

Replacing Eq. 2-37 in Eq. 2-35 and using Eq. 2-32 gives

$$\tilde{\dot{\varepsilon}}_k - \dot{\varepsilon}_k^* = M_{kl}^{(tg)}\overline{\sigma}_l^{'} \qquad \text{(Eq. 2-38)}$$

This equation is formally equivalent to the equation that describes the elastic inclusion problem (once the hydrostatic pressure is accounted for), and that the strain deviation in the inclusion is uniform and given by

$$\tilde{\dot{\varepsilon}}_k = S_{kl}\tilde{\dot{\varepsilon}}_l^* \qquad \text{(Eq. 2-39)}$$

where S_{kl} is the matrix representation of the visco-plastic (instead of the elastic) Eshelby tensor, a function of the shape of the inclusion and the tangent visco-plastic moduli. Replacing the inverse of Eq. 2-39 in Eq. 2-38 gives the classical interaction equation,

$$\tilde{\dot{\varepsilon}}_k = -\tilde{M}_{kl}\sigma_l^{'} \qquad \text{(Eq. 2-40)}$$

where $\tilde{M}$ is the interaction matrix defined as,

$$\tilde{M} = (I - S)^{-1} S M^{(tg)} \quad \text{with tangent compliance moduli} \qquad \text{(Eq. 2-41)}$$

$$\tilde{M} = n(I - S)^{-1} S M^{(\sec)} \quad \text{with secant compliance moduli} \qquad \text{(Eq. 2-42)}$$

So far, the stress and strain rate in each grain with the corresponding magnitudes in the HEM can be related, assuming that the visco-plastic moduli of the grain and of the Hem are known in advance, which is not the case. The assumption that the HEM describes the average behaviour of the aggregate, though, leads to the condition that the weight average of stress and strain rate over the grains has to coincide with corresponding macroscopic magnitudes. The later condition provides an expression from which the overall tensor $M^{(\sec)}$ can be calculated in a self-consistent iterative way. Substituting Eq. 2-27 and Eq. 2-31 in Eq. 2-40 using the condition $<\dot{\varepsilon}>=\dot{E}$, where < > indicates weighted average over all the grains, leads to a simplicity form in terms of the scant moduli,

$$M^{(\sec)} = \left\langle M^{c(\sec)} \frac{(M^{(\sec)} + n(I-S)^{-1} S M^{(\sec)})}{(M^{c(\sec)} + n(I-S)^{-1} S M^{(\sec)})} \right\rangle \qquad \text{(Eq. 2-43)}$$

Using iterative procedure the Eq. 2-27, Eq. 2-40 and Eq. 2-43 are solved, which give the stress in each grain, the compliance tensor of grain and the polycrystal's compliance tensor consistent with the applied strain rate $\dot{E}$.

Therefore, the visco-plastic formulation described above is implemented for the calculation of texture development as follows: the final polycrystal deformation is achieved through successive incremental deformation steps, obtained by imposing a macroscopic strain rate $\dot{E}$ during a time interval Δt. At each step, guess values for the strain rate $\dot{\varepsilon}$ in each grain are proposed: for the first deformation step, a FC guess is used and the stress is calculated solving Eq. 2-26; for the following steps, the strain rate and the stress of the previous step are assumed as starting guess values for the grain. The self-consistent problem is solved by means of two nested iterative procedures. Within the innermost loop, the crystals scant moduli $M^{c(\sec)}$ are calculated for give σ' using Eq. 2-27 and kept fixed. The first estimate of the macroscopic scant modulus $M^{(\sec)}$ is done using a Voigt average: $M^{(\sec)^{-1}} =< M^{c(\sec)^{-1}} >$; for consequent estimates the value derived in the previous step is used. $M^{(\sec)}$ is in turn used to calculate the Eshelby tensor S and the interaction tensor $\tilde{M}$. The iteration is repeat until the average coincides with the input tensor within a certain tolerance, in which case the innermost procedure is terminated, and the $M^{(\sec)}$ is obtained.

Once the stress-strain rate relation is achieved the procedure for reorientation of each grain due to slip and twinning must be performed before attempting the next deformation step. Within the VPSC model the deformation of each grain is different from the matrix and, as a consequence, the reorientation has to include the effect of the local rotation. The lattice rotation for each grain is given by

$$\dot{\varpi}_{ij}^{C} = \dot{\Omega}_{ij} + \dot{\tilde{\Omega}}_{ij} - \frac{1}{2}\sum_{s}^{n}(r_i^S v_j^S - r_j^S v_i^S) d\dot{\gamma}^S \qquad \text{(Eq. 2-44)}$$

where, $\dot{\Omega}$ is the antisymmetric component of the macroscopic rotation rate, and the last term is the antisymmetric component of the plastic distortion rate. The second term $\dot{\tilde{\Omega}}$ represents the local deviation of the macroscopic distortion rate with respect to the average that is calculated using Eshelby tensor S and Eshelby rotation tensor Π,

$$\dot{\tilde{\Omega}}_{ij} = \Pi_{ijkl} S_{ijkl}^{-1} \dot{\tilde{\varepsilon}}_{mn} \qquad \text{(Eq. 2-45)}$$

Twinning model

The contribution of twinning o the grain reorientation is treated according to the predominant twin reorientation (PTR) scheme developed by Van Houtte [109], Tome and Lebenshon et al. [114]. The twinning system is activated in the same fashion as slip according to their CRSS values (albeit only in one direction). Thus twinning system has to associate with two different CRSS values, one describes the threshold value in real shear direction an the other is a very high value that avoids twinning in the opposite direction.

At each deformation step the twinned fraction $\Delta V^{c,t}$ in the c'th grain associated with each twinning system t, is calculated using the shear strain $\Delta\gamma^{c,t}$ to which is contributed by the twinning mode and is accumulated after deformation steps (m).

$$\Delta V^{t,c} = \frac{\Delta\gamma^{t,c}}{S^t} \qquad \text{(Eq. 2-46)}$$

$$V^{m,t,c} = \sum_{m=steps} \frac{\Delta\gamma^{t,c}}{S^t} \qquad \text{(Eq. 2-47)}$$

where S^t is the characteristic shear of the twinning mode. In addition, a sum of the twinned volume fraction is made over all of the crystallites,

$$V^{m.t,all} = \sum_{steps} \sum_{c,t} \Delta V^{c,t} \qquad \text{(Eq. 2-48)}$$

A threshold value for reorientation, $V^{m,t,thr}$, is defined by,

$$V^{m,t,thr} = factor1 + factor2 \frac{V^{m,t,eff}}{V^{m,t,all}} \qquad \text{(Eq. 2-49)}$$

At every deformation step the accumulated twinned fraction of each grain, $V^{m,t,c}$, is checked with a threshold value, $V^{m,t,thr}$. If the $V^{m,t,c}$ of the predominate (the most active) twinning system exceeds the threshold value, the entire volume of the grain is reoriented following the orientation relation of the predominant system. Then this reoriented grain is added to a quantity called the effective twinned fraction, $V^{m,t,eff}$. This process continues until either the all the grains are randomly checked or the value of $V^{m,t,eff}$ exceeds the total twinned volume fraction, $V^{m,t,all}$. As more grains are reoriented by twinning, the threshold value $V^{m,t,thr}$ increases by the increment of $V^{m,t,eff}$. Then, the further reorientation by twinning is inhibited until the $V^{m,t,all}$ catches up with deformation process. The $V^{m,t,eff}$ and $V^{m,t,all}$ tend to remain approximately equal throughout deformation. The $factor1$ and $fractor2$ are given empirically to 0.25. The effect of these constant factors is to delay the reorientation by twinning until the grain exhibits a defined trend and at least 25% of grain has twinned. Once the grains start reorienting, the $V^{m,t,eff}$ increases rapidly and the second term fluctuates around 0.25 after a few incremental steps. Hence, when about 50% of the total grain volume is twinned on a given twinning system, then the grain is reoriented.

The hardening model

Texture simulation can be broadly identify the appropriate ranges of the relative slip system strengths and many attempts were also made to account for the roles of self or latent hardening during the texture simulation. In order to simulate the plastic response of a material, some model of the strain hardening behaviour is needed, in addition to the relative CRSS values. The threshold value responsible for activation of a deformation model, τ_C^S, which appears in Eq. 2-27 is a function of accumulated shear (Γ) in a grain and usually increases with deformation due to strain hardening. An extended form of empirical Voce's hardening law is described by,

$$\tau_C^S = \tau_C^S(\Gamma) = \tau_0^S + (\tau_1^S + \theta_1^S\Gamma)\left(1 - \exp(-\frac{\theta_0^S\Gamma}{\tau_1^S})\right) \qquad \text{(Eq. 2-50)}$$

where, the parameter τ_0 is the initial yield stress, $\tau_0 + \tau_1$ is the back-extrapolated yield stress, i.e. τ_1 acts similar as saturation value, and $\theta_0(\theta_1)$ is the initial (final) hardening rate.

The actual hardening of each mode is accomplished through the following equation at the end of each deformation step, which allows for the incorporation of latent hardening effects.

$$\tau_C^S = \frac{d\tau_C^S}{d\Gamma}\sum_{S} h^{SS'}\Delta\gamma^{S'} \qquad \text{(Eq. 2-51)}$$

The incremental increase of the CRSS, $\Delta\tau$, depends on the amount of shear strain accumulated by each slip system S′. The latent hardening matrix, h^{SS}, provides the possibility for considering the effect of twin boundary. For example, if S′ is a twining mode, then the barrier effect of twin boundary to subsequent twinning and slip can be considered by applying the $h^{SS} = Y$ (values greater than 1).

It should be mentioned that the Eq. 2-50 and Eq. 2-51 express the strain hardening only in a qualitative way, and the dependence of dislocation structure and density on the grain orientation are disregarded. Therefore, the modification for the strain hardening model is being studied by many researches, which accounts for the directionality and actual dislocation structures inside the grain.

3. Experimental procedures

3.1 Materials preparation

The materials used are the commercial cast pure Mg and Mg-Si alloy. The Mg-Si alloy with a chemical composition listed in Tab. 3.1 was fabricated by normal casting method. During casting the pure Mg was firstly melted at temperature of 750 C° followed by the addition of pre-heated Si powder under mixed protective gases of CO_2 and SF_6; and then raising the temperature to 800 C° and holing this temperature for 2h; finally the alloy was cast into a metal die.

Tab. 3.1 Chemical composition of the Mg-Si alloy (in wt. %).

Si	Al	Zn	Mn	Fe	Mg
3.257	0.002	0.028	0.037	0.021	Balance

Hot extrusion of cast pure Mg and Mg-Si alloy was carried out at a horizontal type extrusion machine at 375 C° with an extrusion ratio of 9:1. The outgoing extrusion die is shown in Fig. 3-1(a), which forms two quadratic billets with each a cross section of 15×15 mm^2. The macro-photograph of as-extruded billets is shown in Fig. 3-1 (b). No cracks were observed in the surface of the extruded billet.

The specimen for ECAP has a dimension of 15×15×60 mm^3 which was directly machined parallel to the extrusion direction of the as-extruded quadratic billet. In order to lower the friction effect, each specimen was ground before inserting into the ECAP die.

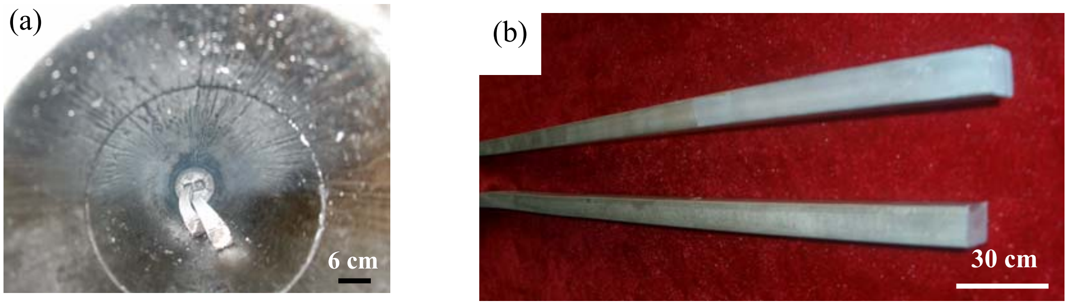

Fig. 3.1 Macro-photograph of (a) the outgoing extrusion die and (b) as-extruded Mg billets.

3.2 ECAP processing

ECAP processing was carried out through a die made of SKD60 with an internal angle ϕ of 90° and an outer curvature angle φ of 37°. The ECAP die includes two parts with a 90° deformation channel totally in one part, as shown in Fig. 3-2 (a) the macro-photograph of the die. Molybdenum disulphide (MoS_2) was used as lubricant. Construction of the whole ECAP die and the pressing machine is shown in Fig. 3-2 (b). A conventional tension-compression machine which can easily control rate was used to produce the pressing load. During ECAP a billet was first inserted into the die and heated to 350°C followed by maintaining this temperature for 30 min., then was pressed under a speed of 20 $mm \cdot min^{-1}$. Three processing routes of A, Bc and C were performed from 1 pass up to 8 passes. The billet for the next pass pressing was pulled out and re-inserted into the die for heating to the desired temperature then maintaining for 30 min. The surface of the ECAP-processed billet will be simultaneously polished if it is not so smooth.

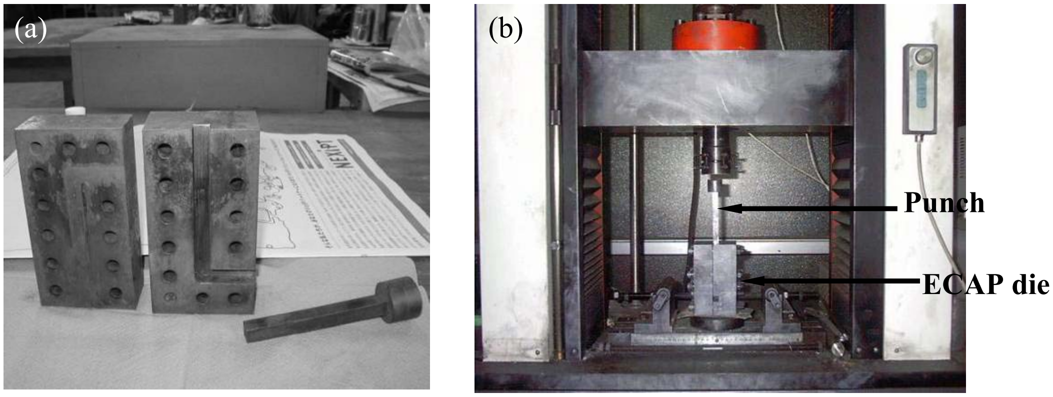

Fig. 3.2 Macro-photograph of (a) geometry of the ECAP die; and (b) construction of the ECAP die and pressing machine.

3.3 Tensile test

Tensile tests were performed at room temperature using an Instron 5569 universal test machine at a constant crosshead speed of 1 mm·min^{-1}. The specimens have a gauge length of 15 mm and cross-sectional areas of 6×2 mm^2 whose size and shape are shown in Fig. 3-3, respectively. The tensile axis was selected to be parallel to the extrusion direction of the conventional extruded and ECAP-processed Mg. Three tensile specimens were tested at the same condition of each ECAP- processed billet.

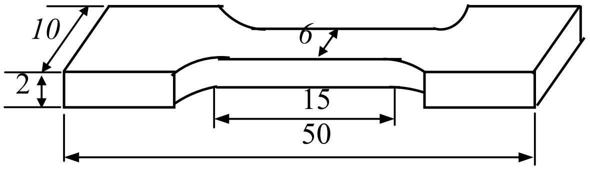

Fig. 3.3 Shape and dimension of a tensile test specimen (mm).

3.4 Microstructures observation

Optical microstructures were obtained by optical microscopy Olympus -PMG3. Hitachi S-4700 and Philips CM12 were used for SEM and TEM microstructure observations. Specimens for microstructures examination were first ground with emery papers followed by final polishing with a suspension of MgO on a cloth. The polished surface was etched by a solution of 10 ml nitric acid, 30 ml acetic acid, 40 ml water, and 120 ml ethanol for 2 ~3 min.. OM microstructures observation plane is parallel to the ED-ND plane, as shown in Fig. 3-4. For TEM, a slice cut from the center part of the ECAP-processed samples, was firstly mechanical ground on both faces down to a thickness around 100 μm, and then punched into 3 mm disc. Finally the disc was thinned by a dual Gatan-600 ion beam thinning apparatus at a voltage of 4.5 kV, a current of 0.5 mA and an incident angle of 7~20°. The operation voltage of the TEM is 120 kV.

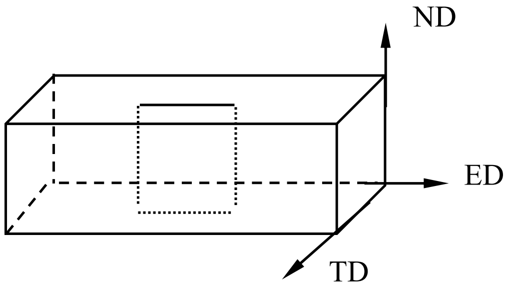

Fig. 3-4 OM microstructure observation position (dash lined cubic) in the ECAP-processed billet.

3.5 Texture characterization

3.5.1 Texture measurement using neutron radiation

The neutron texture measurements were carried out at TEX-2 in GKSS-Research Centre at FRG-1 in Geesthacht, Germany. The measuring time was controlled through the fixed thermal neutron flux for one measuring point, not by fixed time that is generally used for X-ray measurements. For doing such measurements a secondary neutron detector should be installed in between beam shutter and incident slit, so called monitor. That is, once a predetermined neutron count is reached at the monitor the sample moves to the next measuring position of $\{\psi, \varphi\}$. This measuring concept provides the method by which the influence from the fluctuating reactor efficiency can be diminished [88, 89]. 'ψ' stands for the sample tilting and 'φ' for the sample rotation angle. The specimen was glued in a vanadium pin. A pole figure measurement is performed at stationary 2-θ diffraction angle for ($h\ k\ i\ l$) lattice plane in interest, and it is completed by 360° rotation of the sample at each of tilting position from 0° to 90°, as shown in Fig. 3-5 the measured ECAP-processed Mg on the Euler-Cradle.

Despite of the complex shapes of the samples, four of complete pole figures from $\{10\bar{1}0\}$, (0002), $\{10\bar{1}1\}$ and $\{11\bar{2}0\}$ reflexes were obtained, as indicated in Fig. 3-6 the 2-theta scan diffraction pattern of the as-cast Mg-Si alloy. Due to the high penetration depth of thermal neutrons, a posterior intensity-correction is not necessary in neutron technique and as well the absorption effect. Single ^{3}He point detector was applied to the measurements, and the used wavelength was 1.239 Å delivered from graphite monochromator.

The measured pole figure has 679 points distributing regularly in an equal area grid, and then for calculating the ODF, these should be interpolated into an equal angular grid of 5° × 5° with 1368 points. The ODF calculations were performed using the iterative series expansion method with positive correction, and a series expansion degree $L_{max} = 20$ was applied.

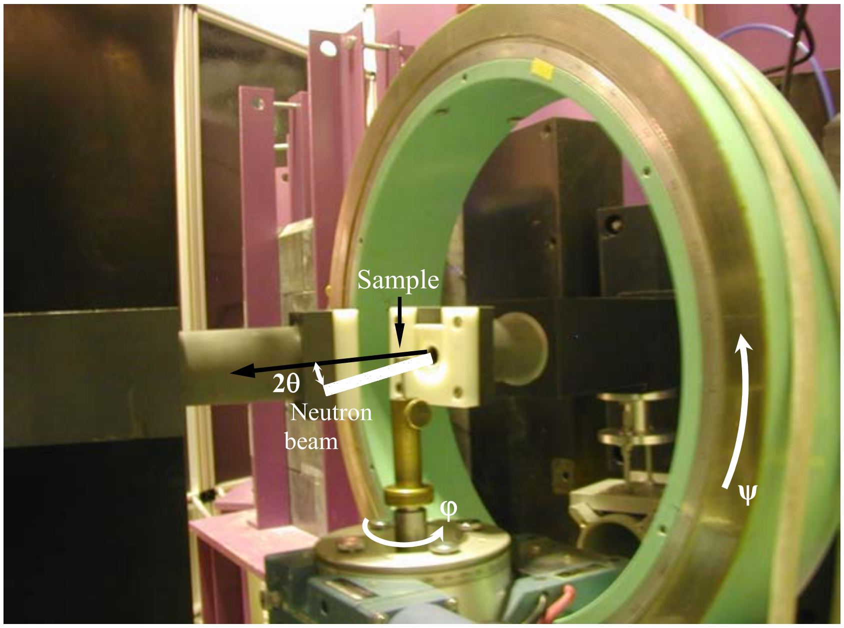

Fig. 3-5 Euler-cradle at TEX-2 in GKSS-Research Centre, Geesthacht. An ECAP-processed sample is located on a sample holder.

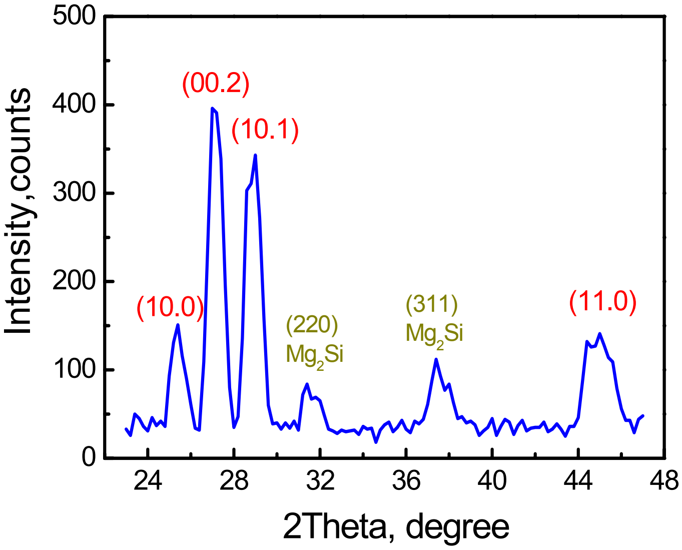

Fig. 3-6 2-theta scan of the as-cast Mg-3.26wt. % Si with neutron diffraction (λ= 1.239 Å).

3.5.2 Texture measurement using synchrotron diffraction

Local texture development in the ECAP-processed Mg was analyzed by synchrotron radiation at energy of 100 keV and a wavelength of 0.1245 Å at HARWI-II-W2, Hamburg. The setting of the machine is shown in Fig. 3-7. The measured samples are stacked together. The sample was rotated in the Euler-cradle through -90° to 90° in 5° each step for a complete pole figure measurement without any sample symmetry, at each of which, Debye-Scherrer patterns were collected for the $\{10\bar{1}0\}$, (0002), $\{10\bar{1}1\}$, $\{10\bar{1}2\}$ and $\{11\bar{2}0\}$ planes from the area detector images, as shown in Fig. 3-8, a complete Deby-Scherrer diffraction pattern of a pure Mg powder. MAR345^{TM} image plate detector was applied to record Debye-Scherrer patterns with 2000 × 2000 pixels (= 300× 300 mm^2 of recording area with a spatial resolution of 150 μm) and the distance of sample to detector is 1762 mm. The incident beam-size of 1×1 mm^2 was used for all measurements, and the recorded intensities were corrected according to the decay of primary beam's intensity during the pole figure evaluations (after the data reduction). Same as in the neutron case, ODFs were calculated using the iterative series expansion method with a series expansion degree $L_{max} = 10$.

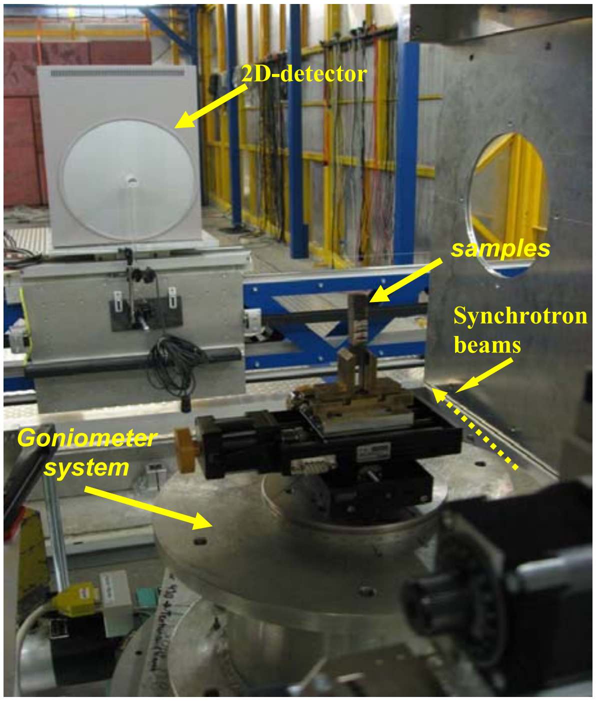

Fig. 3-7 Setting of the machine for texture measurement by synchrotron diffraction at DESY.

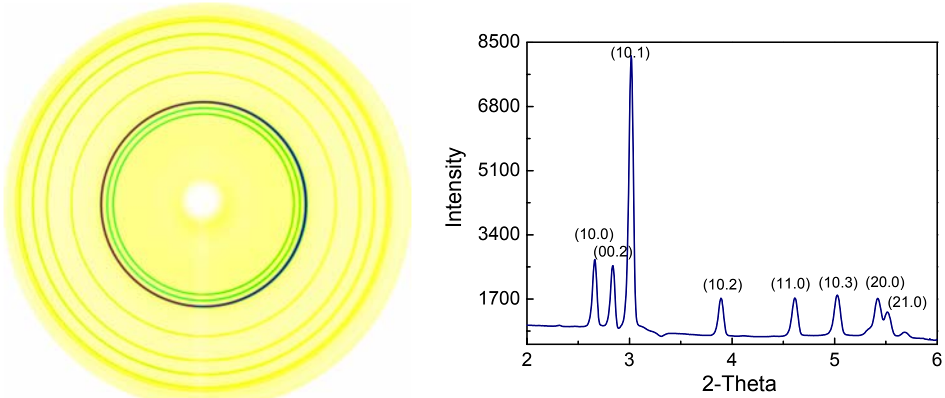

Fig. 3-8 Image plate picture (MAR345) of a pure Mg powder (left) and its sum diffraction pattern (right).

4. Microstructures evolution during ECAP

4.1 Pure Mg

OM microstructure

Optical microstructure evolution of the ECAP-processed as-cast pure Mg from 1 pass up to 8 passes via three routs of A, Bc and C is shown in Fig. 4-1, respectively. The starting as-cast pure Mg has coarse grains of about 900 μm. Grain size is decreased to a bi-modal distribution which some large about 120 μm are surrounded by small grains of about 30 μm, which are due to the dynamic recrystallization (DRX) after 1 pass. DRX is one such process that is commonly observed during elevated temperature deformation of Mg and its alloys [71, 75. 96]. Formation of subgrains during conventional DRX is attributed to the dislocation climb controlled by self-diffusion at elevated temperatures. Repetitive or continuous DRX during deformation leads to the refinement of grains. The microstructure is still very inhomogeneous. Additional decrease of the grain size after 2 passes processing is observed via all three routes processing. However, no distinct decrease or even a slight increase of the grain size is obtained followed by 4 passes up to 8 passes processing, which indicates the growth of grains with the increase of processing pass.

An average grain size of about 38 μm is obtained after hot extrusion at 350 °C. Microstructure evolution of the extruded pure Mg followed by ECAP from 1 pass up to 4 passes via three routes of A, Bc and C is shown in Fig. 4-2, respectively. After 1 pass processing grain size is further decreased to 24 μm comparing with the as-extruded condition. A slight decrease of grain size is obtained after 2 passes with all three routes, which was mainly due to the DRX. Further detailed observation indicated that the microstructure after 2 passes via rout Bc process is more homogeneous than those with other two routes A and C processing, which should be attributed to the accumulated alternate shear effect during each 90° rotation [48-50]. There is no additional decrease of the grain size with the following 3 passes and 4 passes processing which is similar as those as-cast pure Mg after ECAP processing.

It is noted that though the grain size is decreased about 1/10 of the initial size, the grain refinement for pure Mg is still limited with ECAP processing after 2 passes no matter that the starting material is as-cast or as-extruded, in which the main reason could be due to the relatively high processing temperature that makes the grains easy to grow. This result indicates that ECAP can effectively refine the grains at first several processing passes under current construction. ECAP processing of pure Mg at low temperature is thereafter proposed to obtain fine grains. However, cracks will occur on the surface of the billet or the whole work piece will be broken when lowering the processing temperature, experimentally. A bi-model characterization of the microstructure with some significantly larger grains presented in each ECAP-processed condition. The grain shape is nearly spherical, which should be greatly elongated due to large shear during ECAP. Moreover, the forms of the grains, that are not always convex, are clear indications of the occurrence of DRX. In addition, there is no obvious difference in the microstructures with these three routes processing. Grains size in ECAP-processed pure Mg from initial as-extruded material is always smaller than those from initial as-cast material.

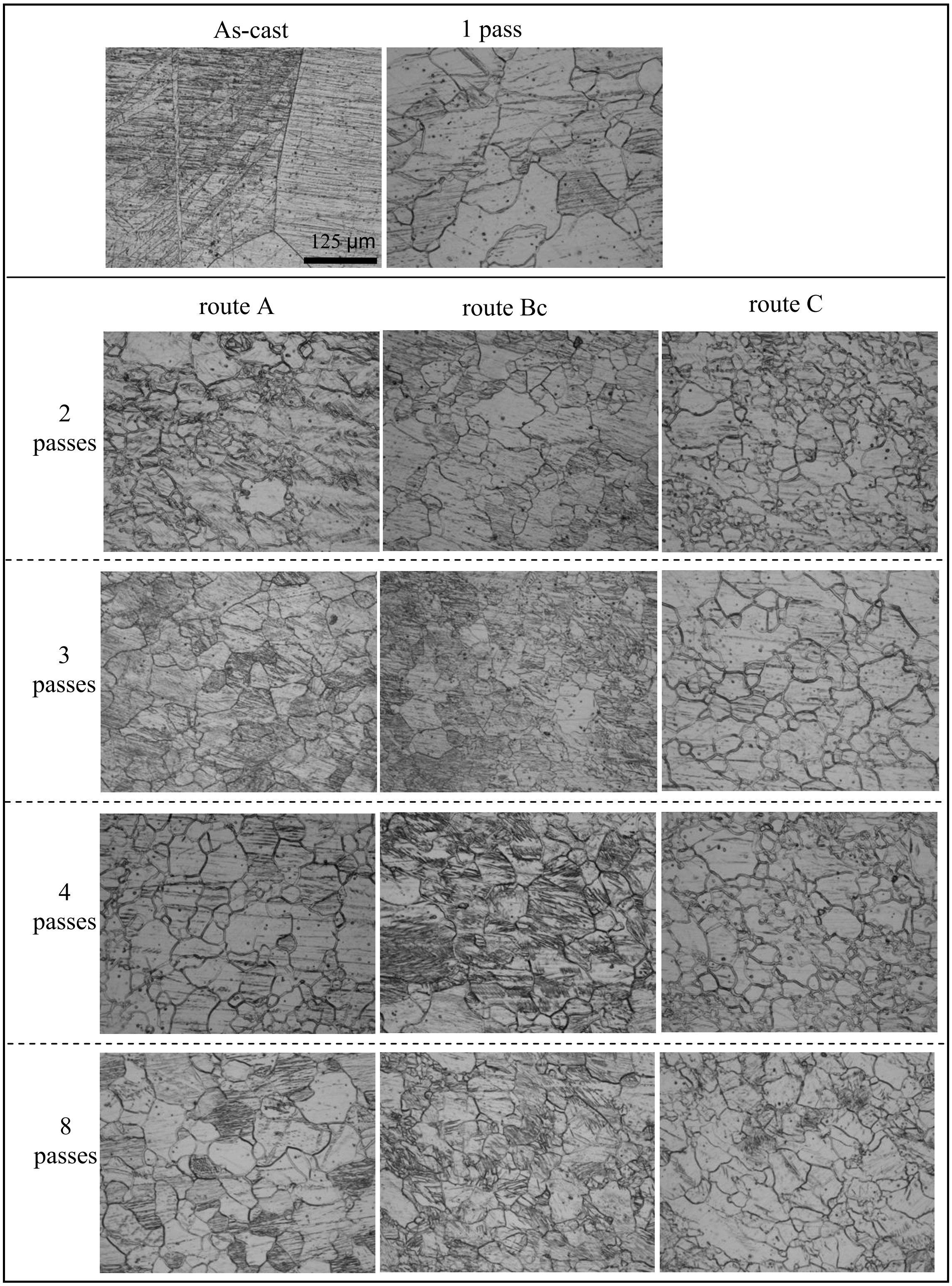

Fig. 4-1 OM microstructures evolution of the ECAP-processed as-cast pure Mg from 1 pass up to 8 passes with three routes of A, Bc and C.

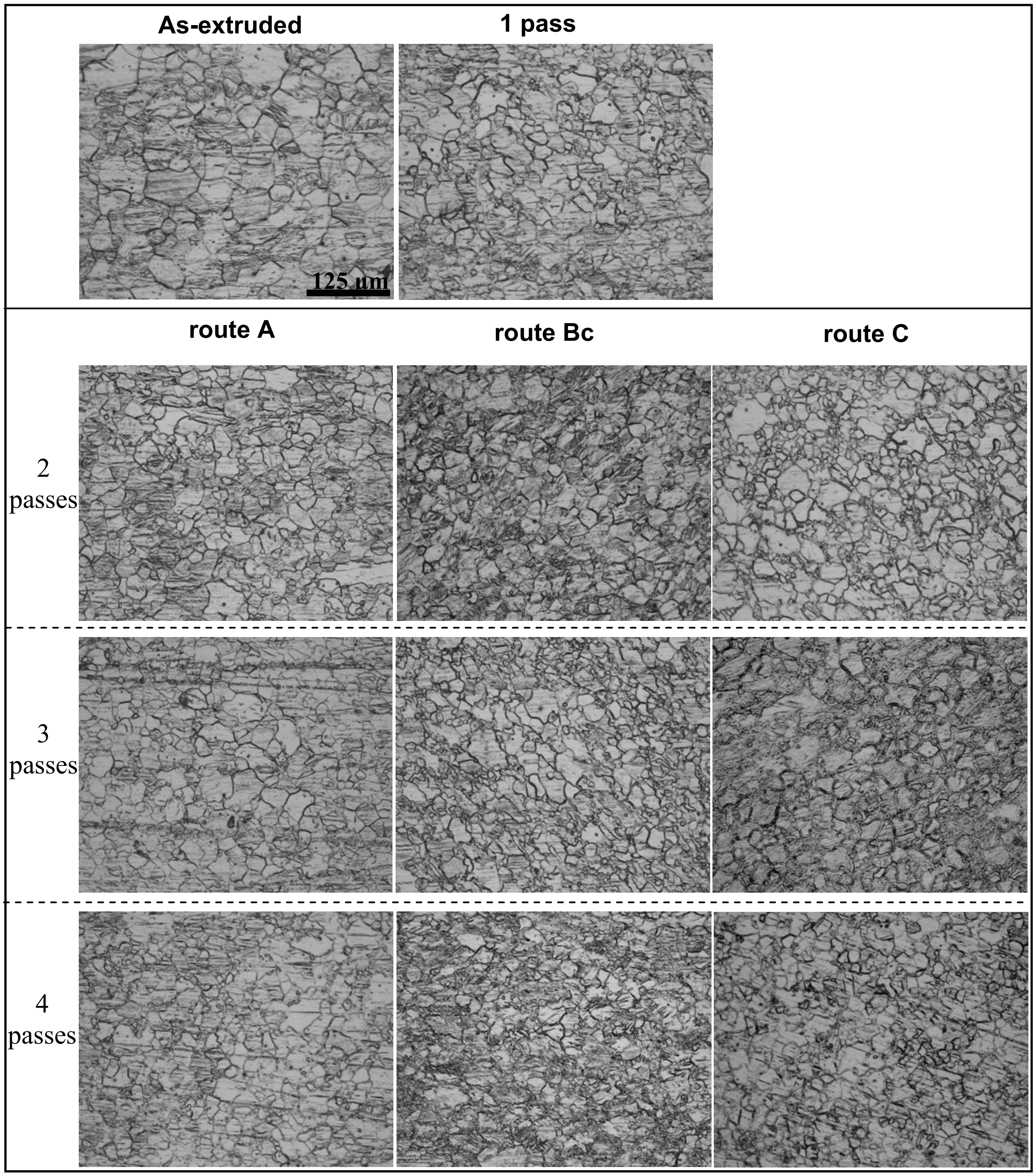

Fig. 4-2 OM microstructures evolution of the ECAP-processed as-extruded pure Mg from 1 pass up to 4 passes with three routes of A, Bc and C.

TEM microstructures

TEM images of pure Mg after extrusion and 4 passes ECAP with three routes of A, Bc and C are shown in Fig. 4-3, respectively. Deformation twining can be clearly observed in each route, as shown in Fig. 4-3 (a), (b) and (c). The selected area diffraction pattern (SADP) was obtained at the boundary between twin and matrix grain which was indicated by an arrow in Fig. 4-3(a) and its indexing are illustrated in Fig. 4-4, respectively. Result indicates that the twin is a $\{10\bar{1}2\}<10\bar{1}1>$ tensile or extension twin which is introduced by a tensile strain parallel to the ***c***-axis or a compression strain normal to the ***c***-axis. Twinning is therefore still one of an important deformation mode in the ECAP-processed billet after 4 passes since that there exists great number of large grains.

Large numbers of sub-grains with high dislocation intensity were observed, as shown in Fig. 4-3 (d), (e) and (f) which were designated with A. Pile up of dislocations at grain boundaries was obtained which designated by the arrows in Fig. 4-3 (d), (e) and (f). A very important feature of the grain boundaries which are not straight but curved or wavy has been widely investigated in the severe plastic deformed materials [80]. There are also grain boundaries with poor TEM images and diffraction contrast inside grains is inhomogeneous and often undergoes complex changes. This indicates a high level of internal stresses and elastic distortions of the crystal lattice. Such a complex contrast observed inside the grains containing lattice dislocations and the grains having no defects indicates that grain boundaries are sources of internal stresses. Pile-up of dislocations around grain boundaries in the ECAP-processed Mg is therefore attributed to the combination effect of the elastic stress during recovering. Recrystallized sub-grains in which few or even free of dislocations and with straight grain boundaries which is caused by DRX were also observed as shown in the figure named B.

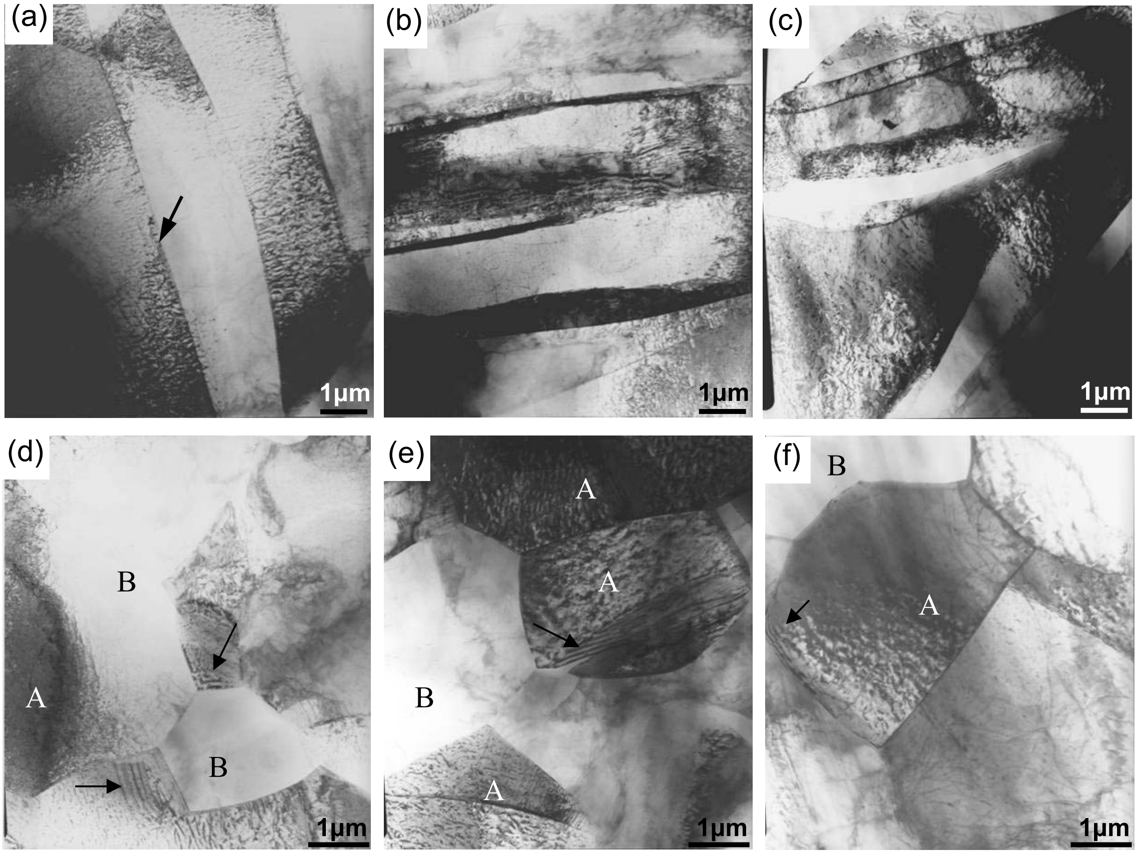

Fig. 4-3 TEM images of pure Mg after extrusion and 4 passes ECAP with route A (a) and (d), route Bc (b) and (e), and route C (c) and (f) (A and B indicate the grains with high an low intensity of dislocations, respectively).

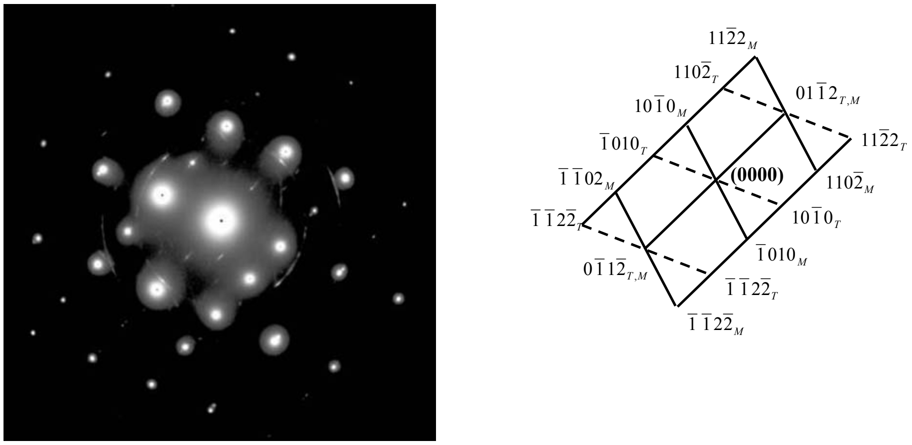

Fig. 4-4 SADP at the twin boundary indicated by an arrow in Fig. 4-3a (left) and the indexing of SADP (right).

4.2 Mg-Si alloy

Fig. 4-5 shows the Mg-Si binary phase diagram in which red line indicates the content of 3.2 wt. % Si. A eutectic recrystallization process during cooling of Mg-Si alloy is evident. OM microstructure of as-cast Mg-3.24 wt.% Si is shown in Fig. 4-6; and the 2-theta scan obtained with x-ray diffraction indicates that there are Mg and Mg_2Si two phases in the as-cast material. Two types of morphologies of the intermetallic phase Mg_2Si are observed in the as-cast material, one is primary solidified polygonal particles (Type-I) which have an average size of about 30 μm; and another is dendritic or fish-bone figuration eutectic Mg_2Si (Type-Π) in the coarse matrix grains. The primary precipitated Mg_2Si polygonal particles are inhomogeneously clustered or accumulated. A very small free Type-Π Mg_2Si occurs around pre-precipitated Type-I Mg_2Si coarse particle, as shown in Fig. 4-6.

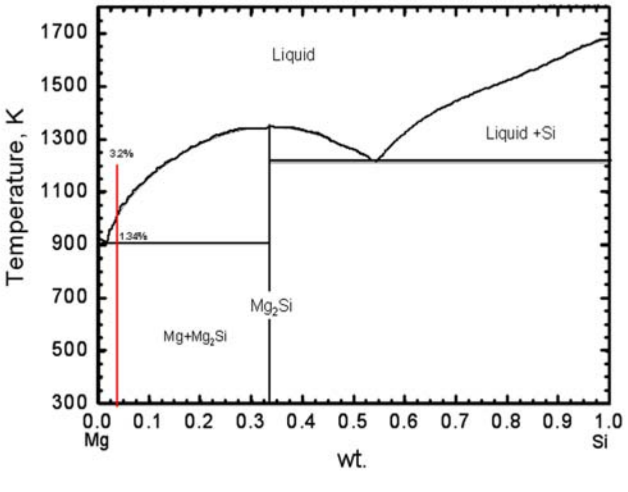

Fig. 4-5 Mg-Si binary phase diagram.

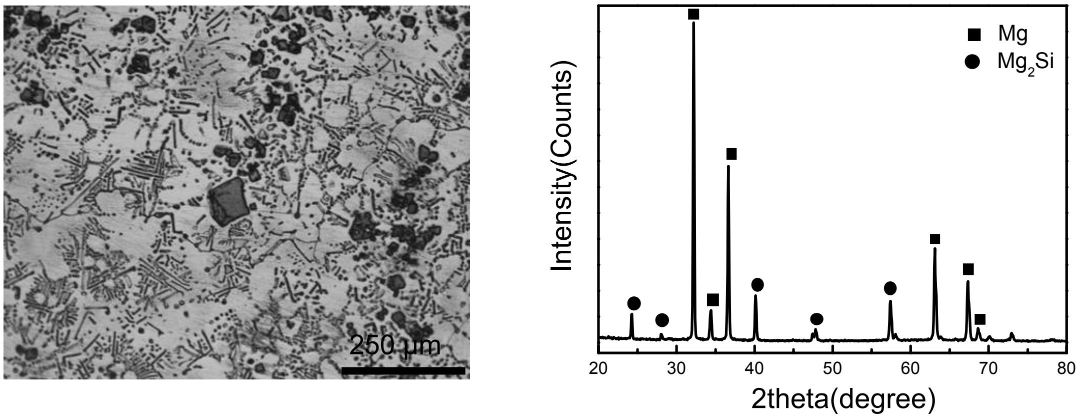

Fig. 4-6 OM microstructure of as-cast Mg-3.24wt%Si (left) and its x-ray diffraction pattern (right).

OM microstructures with low and high magnifications of as-cast Mg-Si alloys under ECAP from 1 pass up to 8 passes via three routes of A, Bc and C are shown in Fig. 4-7 and Fig. 4-8, respectively. After 1 pass the grain size of Mg matrix is decreased from the initial about 250 µm into 70 µm which is led by DRX during deformation. Limited numbers of coarse Type-I Mg_2Si particles are broken to small particles having an average size of < 25 µm. While the dendritic Type- Π Mg_2Si is greatly broken into a great number of small particles and re-distributed with an angle of about 45° to the ECAP direction. The microstructure is still inhomogeneous after 1 pass.

Followed by 2 passes up to 8 passes with three different routes processing the hard and more or less round Type-I Mg_2Si particles rotate with the material flow of the matrix without any distinct deformation. There still exits many large Mg_2Si particles of > 25 µm even after 8 passes. Clustering of Type-I Mg_2Si is still existed. It is therefore difficult to further refine these Type-I Mg_2Si particles, in which the main reason could be due to a very high hardness of the Mg_2Si comparing with the matrix pure Mg. This is a typical effect of the co-deformation in composite with very hard particles in a soft matrix (e.g. Ni in Al or SiC in Mg and Al, et al.). Hardness of Mg is extremely lower than that of Mg_2Si at high temperature [10, 12], so the shearing stress that enforced by the matrix was not enough to break the Mg_2Si particles. Hence, stress concentration around Mg_2Si particles easily occurs which will contribute to the easy activations of twinning, as can be seen in Fig. 4-9 (b) many twins are observed between or around Mg_2Si particles.

As for the Type- Π Mg_2Si, observations show that they are gradually broken and re-distributed with an angle of 45° to the ECAP direction with each pass by different rotation. Much more homogeneous distribution of the refined particles is obtained after 8 passes. However, clustering of the fine particles along the shear deformation is still observed. Small recrystallized Mg grains are observed around Mg_2Si particles; but there still exits some large elongated Mg grains surrounded by Mg_2Si small particles. The grain size of Mg after 8 passes processing is similar as that after 4 pass processing, which could be due to that the Mg_2Si hard particles hinders the grains growth of the matrix pure Mg. It is noted that the primary precipitated large polygonal Mg_2Si particle was broken into several smalls round ones under the shearing stress which being enforced by the shear stress of the matrix, as shown in Fig. 4-9, the former large Mg_2Si particle was broken into four small Mg_2Si particles which designated by a, b, c and d in Fig. 4-9 (a), respectively.

In order to investigate the influence of the input microstructure, ECAP of the as-extruded Mg-Si alloy was also performed. OM microstructures at low and high magnifications of the hot extruded Mg-Si alloy followed by ECAP processing with route A, Bc and C up to 8 passes are shown in Fig. 4-10 and Fig. 4-11, respectively. After hot extrusion the Mg_2Si particles are re-distributed parallel to the extrusion direction (designated by an arrow) together with a great refinement of the matrix grains. Many twins are observed around Mg_2Si particles, which indicates that hard Mg_2Si particle contributed to the initiation of twinning.

After 1 pass more refined grains are obtained due to DRX. No distinct size decrease of the Type-I Mg_2Si particles was observed excepting the much more homogeneous distribution of the broken Type-Π Mg_2Si particles. More Type-Π Mg_2Si particles are still distributed parallel to the ECAP direction instead of a 45° angle orientation. This distribution was remained till 2 passes by all three routes processing. However, a 45° distribution of the Type-Π Mg_2Si particles started to occur followed by 4 and 8 passes, as shown in Fig. 4-10.

4.3 Discussion

The most attractive of ECAP is to refine the grains of various materials. However, the fundamental study of grain refinement mechanism of the ECAP process still remains to be investigated, especially in ***hcp*** structure materials. Though it is generally accepted the grain refinement mechanism involves the combination of mechanical shear, accumulation of strains and/or dynamic recrystallization during ECAP, it remains arguable and unclear given that the existing modes may not be directly applicable in all situations of the process. In addition, construction of ECAP device has different designs although retaining similar key parameters. Several grain refinement mechanisms were proposed in ***fcc*** materials. Segal et al. [30, 31, 43] proposed a grain refinement model based the formation of shear bands and subgrain rotation. The model proposed by Zhu and Lowe [47] was based on various works on ECAP, concluding that grain refinement was primarily the result of the interaction of shear plane with texture and crystal structure in which a secondary role of redundant shear strain from multiple ECAP passes was considered. Xu et al. [136] studied ECAP-processed Al alloy deformed at room temperature and proposed a model where the grain refinement process was due to the mechanical shearing of grains, and equiaxed grains were formed when the elongated arrays of grains were subsequently shear in other directions. All these models are more suitable for the cubic materials with inherently high formability and ductility which deforms primarily by dislocation slip. As for ***hcp*** system materials in which twinning play an important role, the grain refinement mechanism can not considered solely on a mechanical or geometric approach while neglecting the recovery and recrystallization process involved at their respective processing temperature.

In this work of the ECAP processing of pure Mg, the above microstructures observations have shown us the existence of twinning, recovered or recrystllized grains in each condition processing. And also the limitation of grain refinement is obtained. It is obvious that processing temperature plays a key role on the grains refinement in ECAP processing of Mg. More recently, Su et al. [137] studied the microstructures evolution in ECAP-processed AZ31 at 200 °C; and the results showed that the grain refinement mechanism for AZ31 during ECAP was by a combination of mechanical shearing and subsequent continuous recovery, recrystallization and growth of grains and subgrains into cells to produce refined and equiaixed grains within one pass. The grains refinement procedure can be described as: firstly the initial coarse grains was immediately deformed along shear plane with the formation of shear band and dislocations piles-up; continuous recovery leading to the rearrangement of dislocations and formation of subgrains; and finally static growth from heating leads to formation of high angle boundaries from subgrains and recrystallized grains. The dwell time after which the billet passes through the die controls the grain growth. This is also related to the pressing speed which is difficult to estimate considering different die constructions and materials. DRX and grain growth are then compete with each other during ECAP. Therefore, in order to effectively refine the grains of Mg by ECAP, it is proposed that gradually decrease the processing temperature and increase the pressing speed on condition that no materials fracture is happened.

It is noted that the grain size in 1 pass ECAP-processed as-cast Mg-Si alloy is around 10~50 μm comparing with that in pure Mg about 50~100 μm. Since the same processing temperature was used, this distinct difference of grain size should be attributed to the existence of Mg_2Si particles. Matrix grain size is further decreased or some are remained similar in Mg-Si alloy followed by the next pass processing, while the grain growth happens in pure Mg. Grain refinement mechanism in composite by co-deformation between second phase and matrix grains has been widely discussed. Effect of these two Mg_2Si on matrix grains refinement should be different. It is clear the interface stress between eutectic Mg_2Si and matrix grains is much stronger than that between Type-I and matrix. Though few Type-I Mg_2Si were broken, their size were still large which was obstacle to the matrix deformation. Great numbers of twinning were therefore observed around large Mg_2Si particles. As for the dendritic Type-Π Mg_2Si, several microns of the refined particles will strengthen the mechanical stress of the matrix flow which contributes to the refinement of matrix grains. Hence, it is effective to have the small Mg_2Si particles in Mg-Si alloy. Since it is difficult to refine the coarse Type-I Mg_2Si particles by ECAP processing, it is proposed an effective use of Si grain refiner to reduce the volume fraction to obtain only Type-Π Mg_2Si.

4.4 Summary

(1) Coarse grains of about 900 μm in as- cast pure Mg are refined to a bi-model distribution with some large about 120 μm surrounded by small grains of about 30 μm after single pass ECAP. Grains size remained no obviously change followed by the next passes ECAP processing. As for the initial as-extruded pure Mg, the starting grains of about 38 μm was decreased into about 24 μm after single pass. More homogeneous distribution of grains was obtained via route Bc processing.

(2) Grain refinement for pure Mg was still limited by ECAP after 2 passes no matter that the starting material was as-cast or as-extruded, in which the main reason could be due to the relatively high processing temperature that made the grains easy to grow. It is proposed here gradually decrease processing temperature with the increase of processing pass under primes of no occurrence of cracks in the billet. No distinct difference of the microstructures was found among using three different routes. More twins were observed when the input grains were large.

(3) The polygonal Type-I Mg_2Si particles can not be effectively broken and homogeneously redistributed during ECAP no mater the initial material is as-cast or as-extruded under the present work, in which was due to their almost round morphology and the huge difference of the hardness between Mg_2Si intermetallic phase and matrix Mg. The dendritic Type-Π Mg_2Si was gradually broken and homogeneously redistributed in matrix with the increase of processing pass.

(4) Existence of small Mg_2Si particles hindered the growth of matrix Mg grains and also contributed to initiation of twinning. It is proposed from the present study that it is effective for the use of Si to form only the eutectic Mg_2Si phase to prepare Mg-Si alloy or so called the in-situ Mg_2Si/Mg composite.

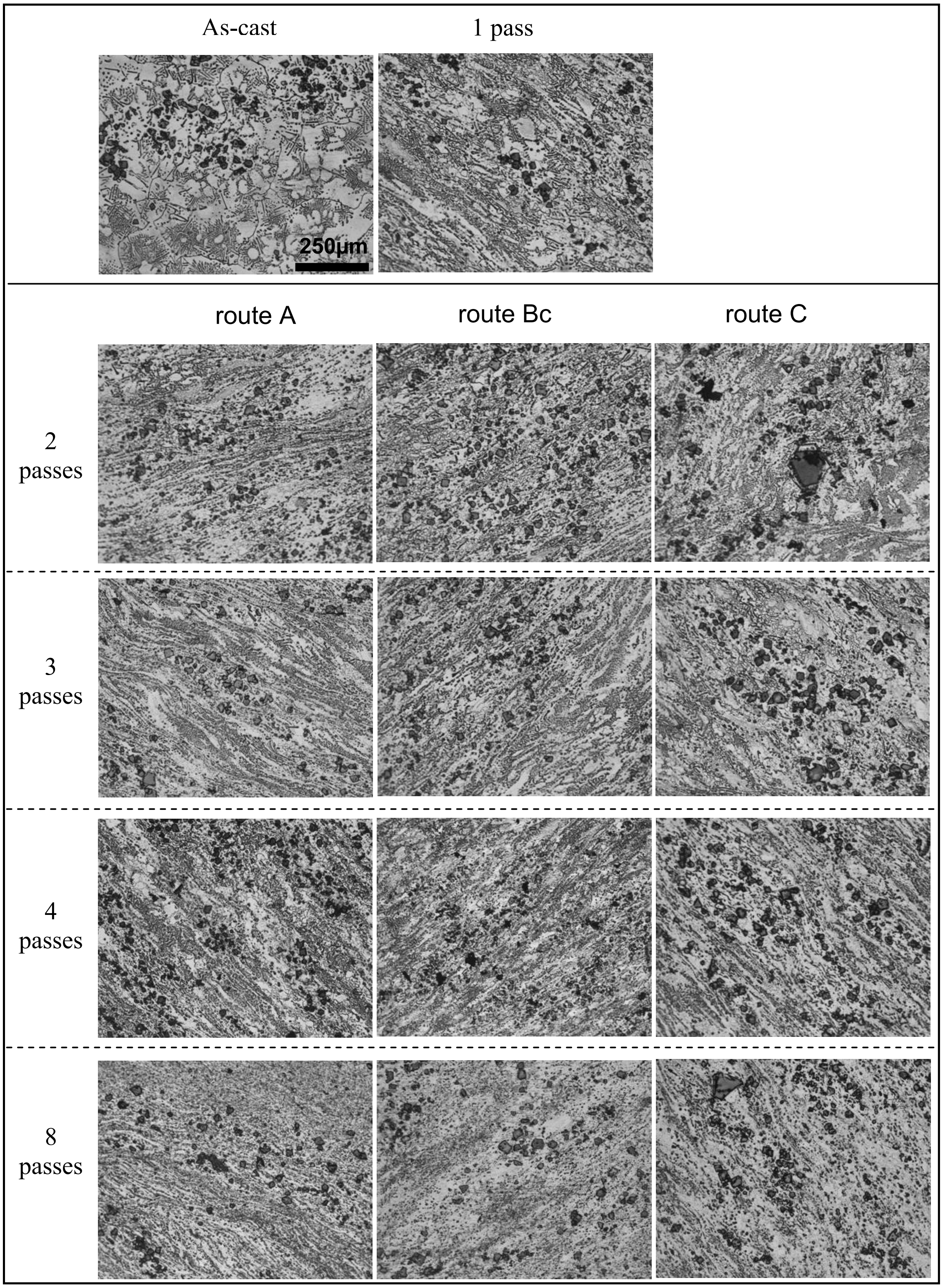

Fig. 4-7 OM microstructures evolution at lower magnification of the ECAP-processed as-cast Mg-Si from 1 pass to 8 passes with three routes of A, Bc and C.

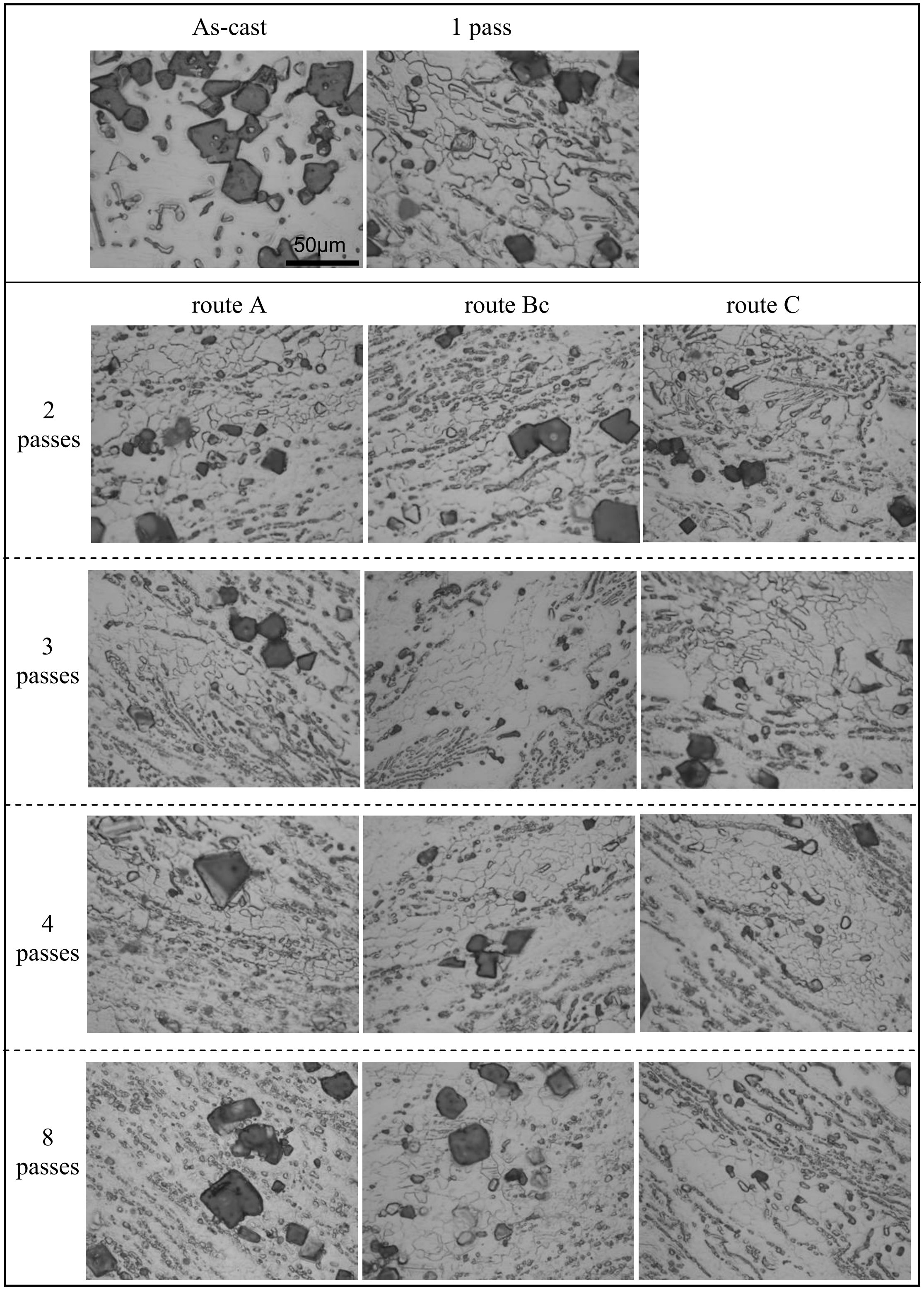

Fig. 4-8 OM microstructures evolution at higher magnification of the ECAP-processed as-cast Mg-Si from 1 pass to 8 passes with three routes of A, Bc and C

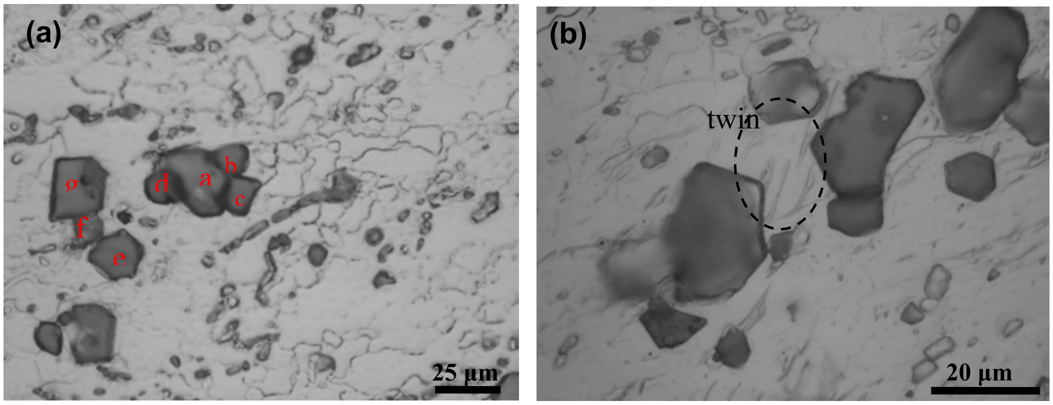

Fig. 4-9 OM microstructures of the ECAP-processed as-cast Mg-Si after (a) 4 passes and (b) 8 passes processing.

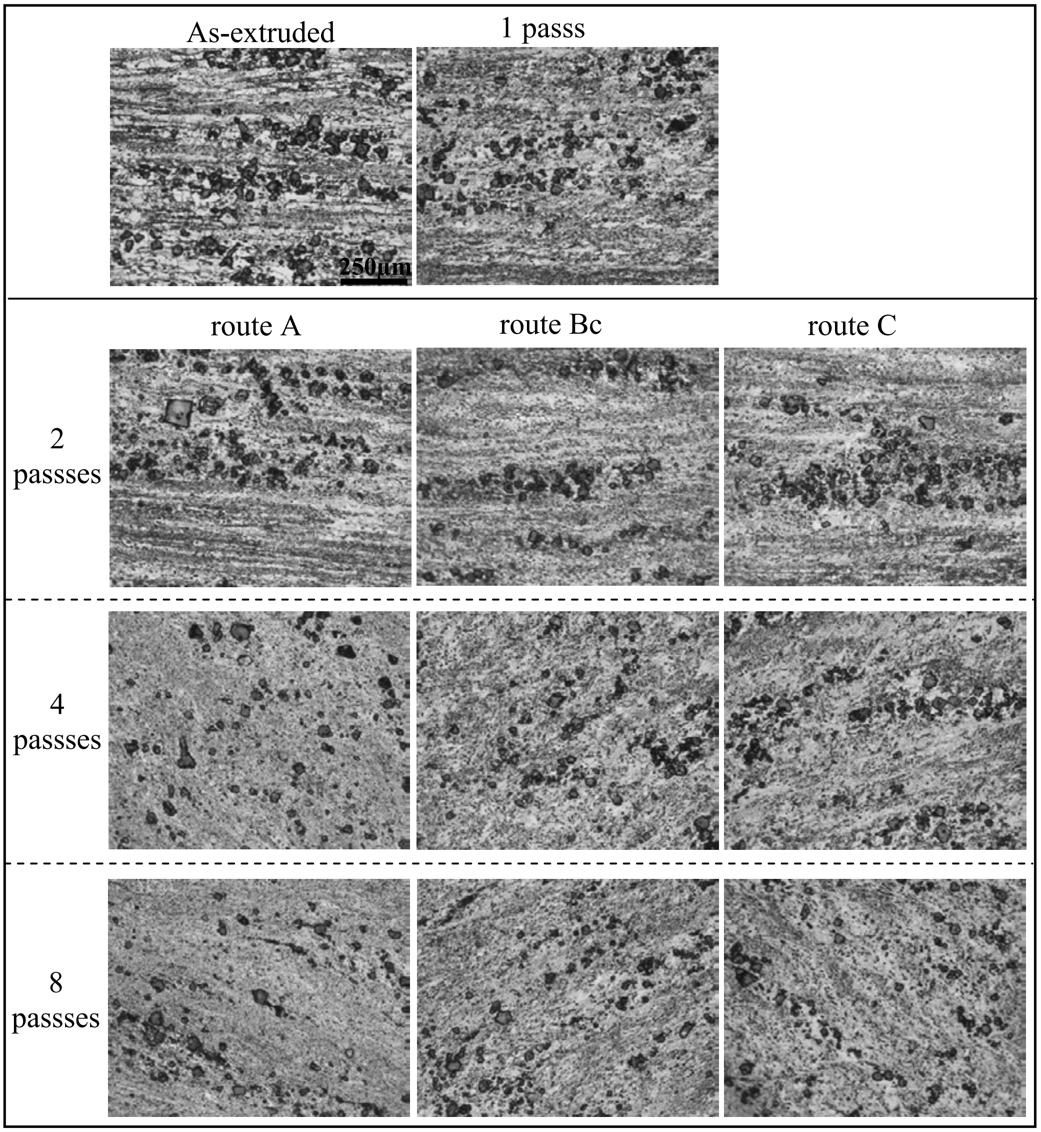

Fig. 4-10 OM microstructures evolution at lower magnification of ECAP-processed as-extruded Mg-Si from 1 pass to 8 passes with three routes of A, Bc and C.

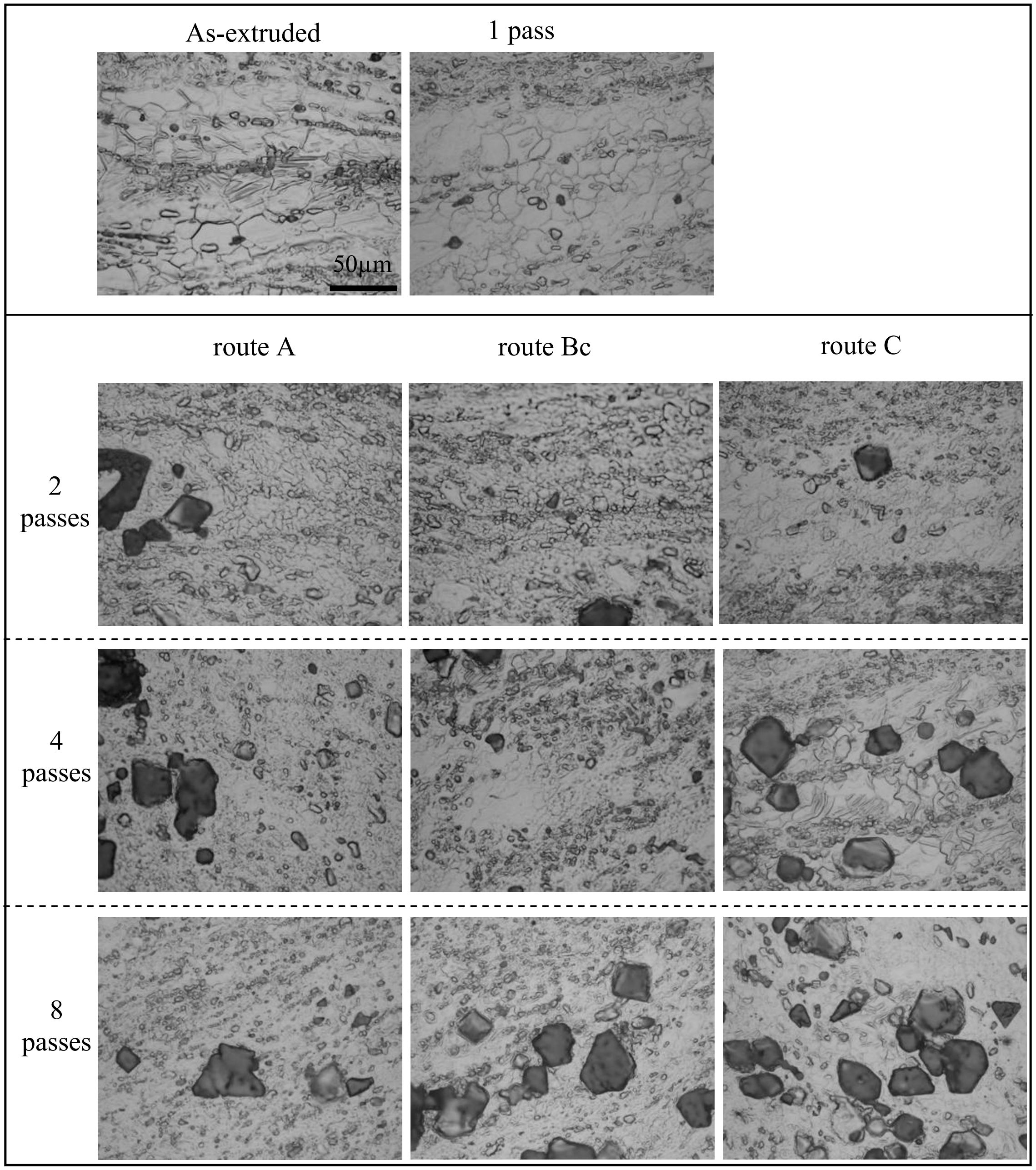

Fig. 4-11 OM microstructures evolution at higher magnification of the ECAP-processed as-extruded Mg-Si from 1 pass to 8 passes with three routes of A, Bc and C.

5. Texture development during ECAP

5.1 Pure Mg

In order to characterize the symmetry of deformation process, sample coordination system in pole figure is defined in Fig. 5-1, where ED, TD and ND are the extrusion, the transverse, and the normal direction of the ECAP-processed work piece, respectively. Projections on plane ED-ND and plane ND-TD were mostly used in published papers [102, 103, 118, 138]. To clearly characterize the symmetry of pole figure around different sample's direction and compare the present results with the published works, two projection plans are applied to plot the pole figure (seen in Fig. 5-1) in which the ED-ND projection (plane 1) and the ED-TD projection (plane 2). The theoretical simple shear plane 3 which has an angle of 45° to the extrusion plane 2 can be easily described in the projection plane 1 (the dashed line in pole figure).

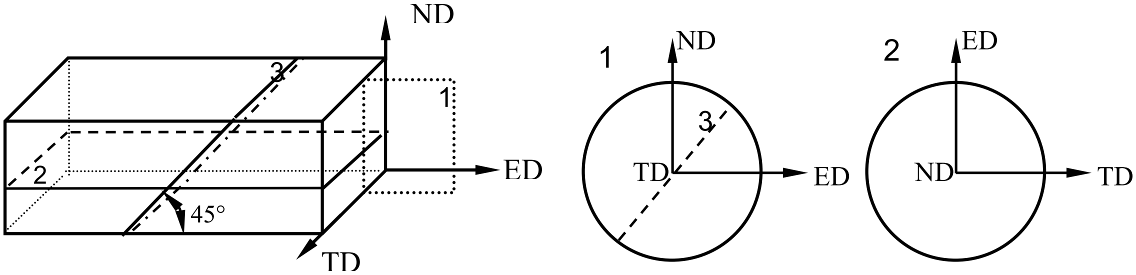

Fig. 5-1 Definition of the projection plane for characterization of pole figure.

ECAP texture of as-cast pure Mg

Fig. 5-2 shows the (0002) and $(10\bar{1}0)$ complete pole figures on projection plane 1of as-cast pure Mg and after 1 pass ECAP processing, respectively. No preferred orientation is obtained in as-cast pure Mg though several strong maxima points are observed in pole figures. These maximums come from the diffraction of several single grains since the as-cast pure Mg has relatively huge grains. After 1 pass processing a <00.2> basal fiber with its fiber axis rotating about 30° to the ND was formed. Looking on projection 2 an asymmetry around the ED was found and basal planes in most grains orientated at about 42° to the ED with a splitting maxima. Two reasons are contributed to the formation of these double maxima. It is known that basal slip and twinning are the main deformation mechanisms in the coarse grained Mg. The fist one is related to the activation of double or triple twinning modes for accommodation the strain along the ***c***-axis, suggested by Couling and Wonsiewicz [23]. Researches on the hot rolling of coarse grained Mg-Al alloy by Jin et al. [115] showed that twinning accommodated most of the strain at the initial stage of rolling; and a basal texture originated from the $\{10\bar{1}2\}$ twinning mode was proposed. The second explanation is based on the high activation of <***c+a***> slip modes, which was suggested by Agnew et al. A clear explanation on the mechanism of basal poles' splitting is still in doubt; however, it is sure that the both of mentioned mechanisms are necessary for the strain accommodation.

When studying texture, microstructure or mechanical properties after multiple ECAP passes, an understanding of the influence of the sequence of billet rotations (i.e. the route) is fundamental. Apart from the strain path change during ECAP, each billet rotation is accompanied by a rotation of the texture, which determines the initial texture for the subsequent pass. This initial texture is of major importance for the subsequent textural and structural evolution. Previously, comparisons between textures after different routes have been made, based on experimental and modeled textures. However, the authors did not look into detail in the role of the texture rotation between passes. Since the existed texture has a strong effect on the following deformation behavior, input texture for the following EACP with different rotation routes are illustrated before each pass. Detailed rotation of the input texture is illustrated in Fig. 5-3. The defined sample coordination system is fixed on projection plane 1, the ECAP-processed billet is firstly rotated around the TD for the next pass input and then is rotated with 0°, 90° and 180° around E´D´ in the new coordination system (from Fig. 5-3 (a) to (b), (c) and (d)) which indicates routes A, Bc and C, respectively. The rotated pole figure is also projected on plane 1. The compression direction is therefore parallel to ND. Fig. 5-4 shows the input and output (0002) and $(10\bar{1}0)$ complete pole figures on projection plane 1of ECAP-processed pure Mg from 2 passes to 4 passes with three different routs. With route A processing, the compressive direction ND has an angle of about 42° to the ***c***-axis when starting the 2 passes ECAP. After 2 passes the <00.2> fiber is strengthened with its fiber axis an oft angle of 20° to the ND. Asymmetry around the ED is still observed when looking on projection plane 2 but at an inverse direction. Followed by 3 and 4 passes, this fiber is remained with a gradually movement of the maxima to the pole figure center. Obtaining of a high maximum as 9.0 mrd (mrd- multiples of the random distribution) is noted after 4 passes.

With route Bc 90° rotation of the input texture makes the compression axis orientate nearly normal to the ***c***-axis, the <00.2> fiber is also obtained after 2 passes. Similarly, compression normal to ***c***-axis for following 3 passes was happened. Reorientation of the basal planes normal to the ND direction leads to the formation of <00.2> fiber along the ND. Same procedure goes for 4 passes; it is interesting to find that a weak maximum is found in the 4 passes ECAP-processed billet which should come from the input texture.

With route C processing a 180° rotation of input texture, the compressive axis is nearly normal to the ***c***-axis. It can be seen that nearly a symmetric <00.2> fiber around ND is formed after 3 and 4 passes. Obvious increase of maxima with the increase of processing pass is obtained. With deformation process, more and more grains are rotated with their ***c***-axis parallel to the compression stress. Therefore, the basal texture is progressively strengthened. Maxima as 11.3 mrd rolling or compressing texture is formed after 4 passes when looking on projection plane 2.

Remarkable is that the present ECAP texture is similar as those obtained by compression or rolling which produce basal preferred orientation instead of the theoretically simple shear texture using a 90° die. Large number of investigations has shown that hot compression or rolling of Mg can produce a texture with the (0002) plane vertical (or the ***c***-axis parallel) to compression or rolling direction [94, 95, 116, 117]. Shearing effect is less or not found no mater what rotation route is applied. What one can obtain is that the basal planes are nearly 90° re-oriented after each pass which was caused by the device. In order to have a direct reviewing of the input and output texture component, evolution of an ***hcp*** cell is schematically shown in Fig. 5-6. It can be found that the compression direction is nearly normal to the ***c***-axis via each rotation routes. And the output texture after each pass has a similar basal distribution which the compression is parallel to the ***c***-axis. Therefore, the basal planes in each grain is rotated about 90° when pass through the 90° channel with less shear. Detailed reason will be discussed thereafter.

ECAP texture of as-extruded pure Mg

(0002) and $(10\bar{1}0)$ complete pole figures on projection plane 1and 2 of the pure Mg after hot extrusion and followed by ECAP processing from 1 pass up to 4 passes via different routes of A, Bc and C are shown in Fig. 5-7 and Fig. 5-8, respectively. Texture in the quadratic extruded pure Mg consists of a central component visible inside the (0002) pole figure and a girdle distribution along the TD. Two weak shear components are observed in pole figure which should be attributed to the mismatched material's flow speed at four corners of the quadratic die.

After 1 pass processing the <00.2> basal fiber with its axis about 10° oft to the ND is formed, which is similar as that obtained in the as-cast Mg after 1 pass ECAP. The center maximum pole intensity is moved to the center and the asymmetry around the ED is still observed when looking on projection plane 2. After 4 passes with route A the oft angle of fiber axis is changed into 20°. While with route Bc the fiber axis remains but with a small decrease of the maxima. Most basal planes were re-oriented normal to the ND by route C.

Comparing the textures developed in ECAP-processed as-extruded pure Mg with those correspondingly developed in as-cast pure Mg, it can be found that similar basal fiber is produced. Remarkable is the texture intensity in ECAP-processed as-extruded pure Mg is weaker than those in as-cast conditions. The main reasons could be due to the grain size effect. Obviously fine grains in ECAP-processed as-extruded pure Mg is obtained, which has been illustrated in the formed chapter. More rotations of fine grains can randomize the texture. Stain hardening behavior could also different in as-cast and as-extruded pure Mg which affect correspondingly the deformation behavior during ECAP.

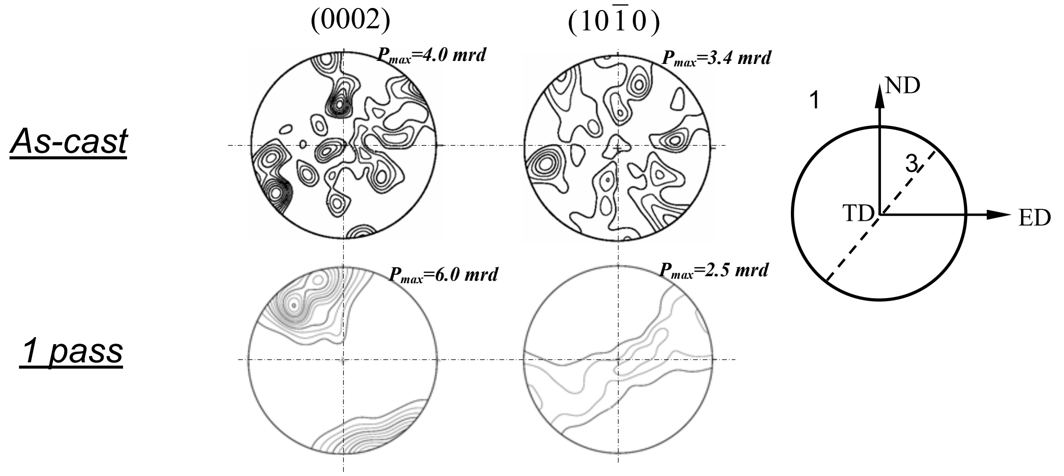

Fig. 5-2 Complete pole figures on projection plane 1 of cast pure Mg and after 1 pass ECAP.

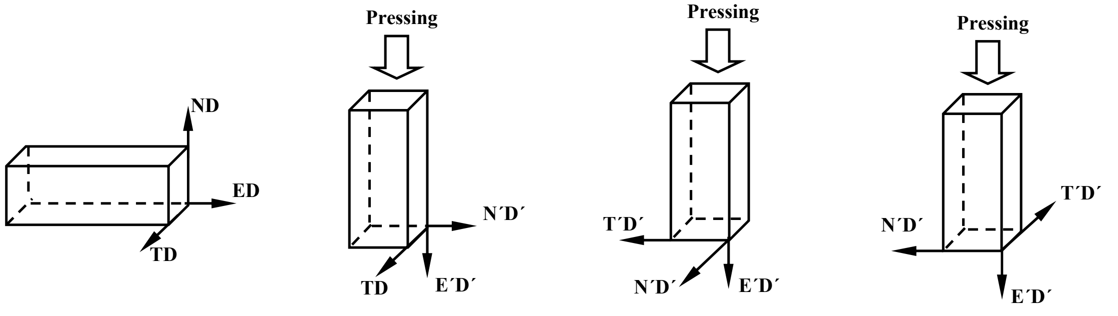

(a) Billet after ECAP

(b) Input billet without rotation

(c) Input billet with 90° rotation

(d) Input billet with 180° rotation

Fig. 5-3 Schematically showing the rotation of billet between two ECAP pass by different routes.

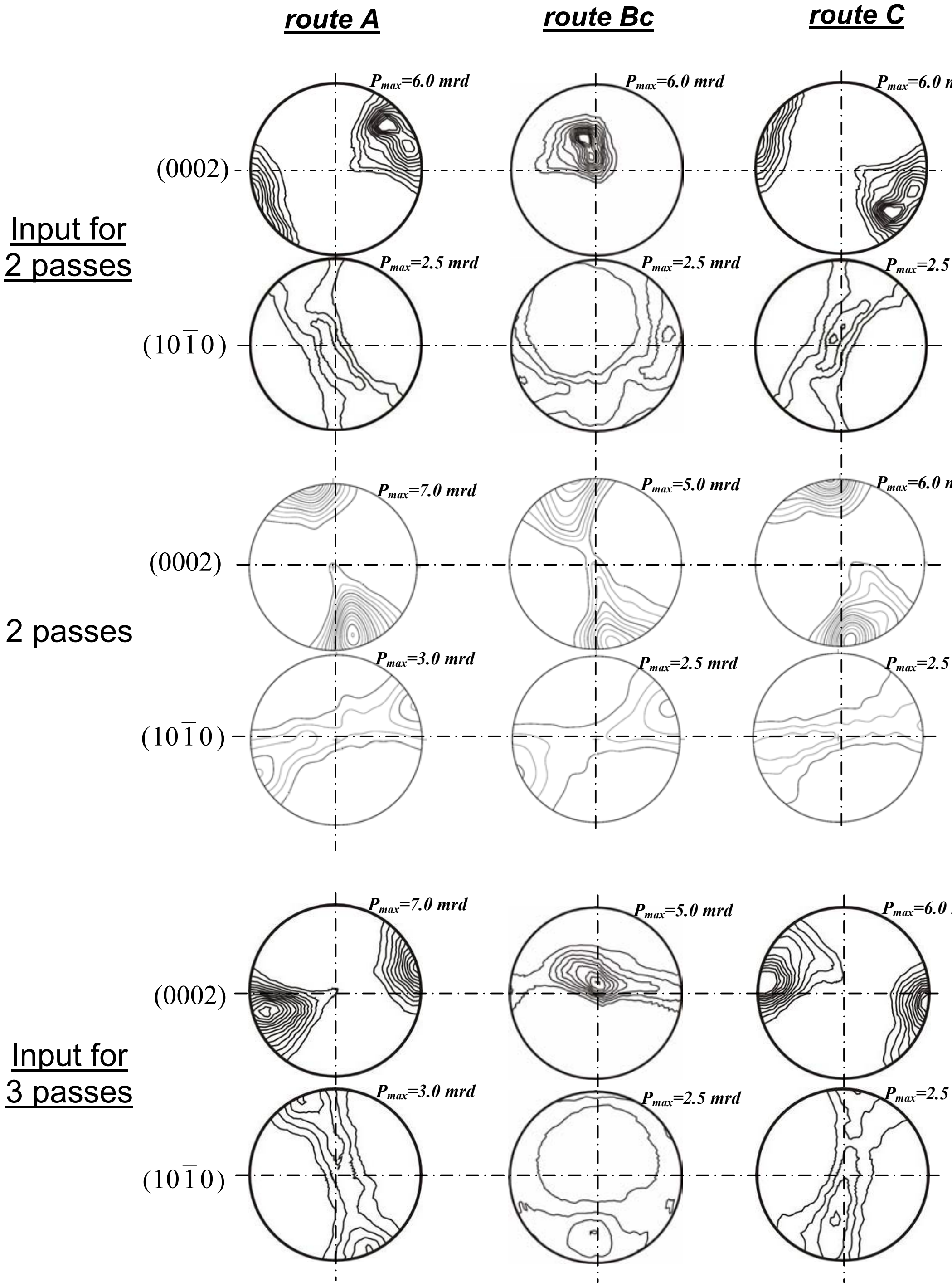

Fig. 5-4 (0002) and $(10\bar{1}0)$ complete pole figures on projection plane 1 of as-cast pure Mg before and after ECAP from 2 pass up to 4 passes with three routes of A, Bc and C. (Contour levels=1.0×, 1.5×, 2.0×, 2.5×, …).

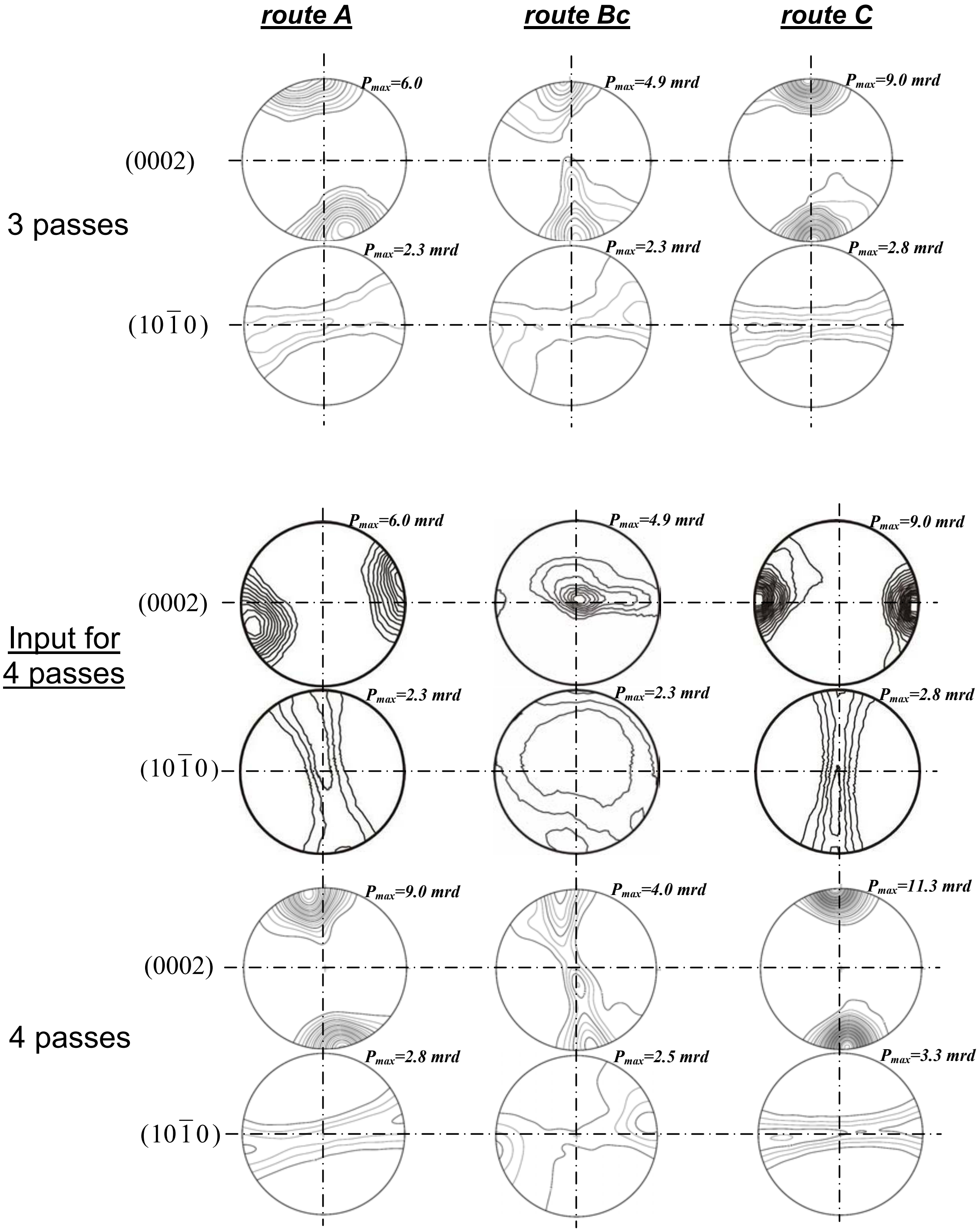

Fig. 5-4 Continued.

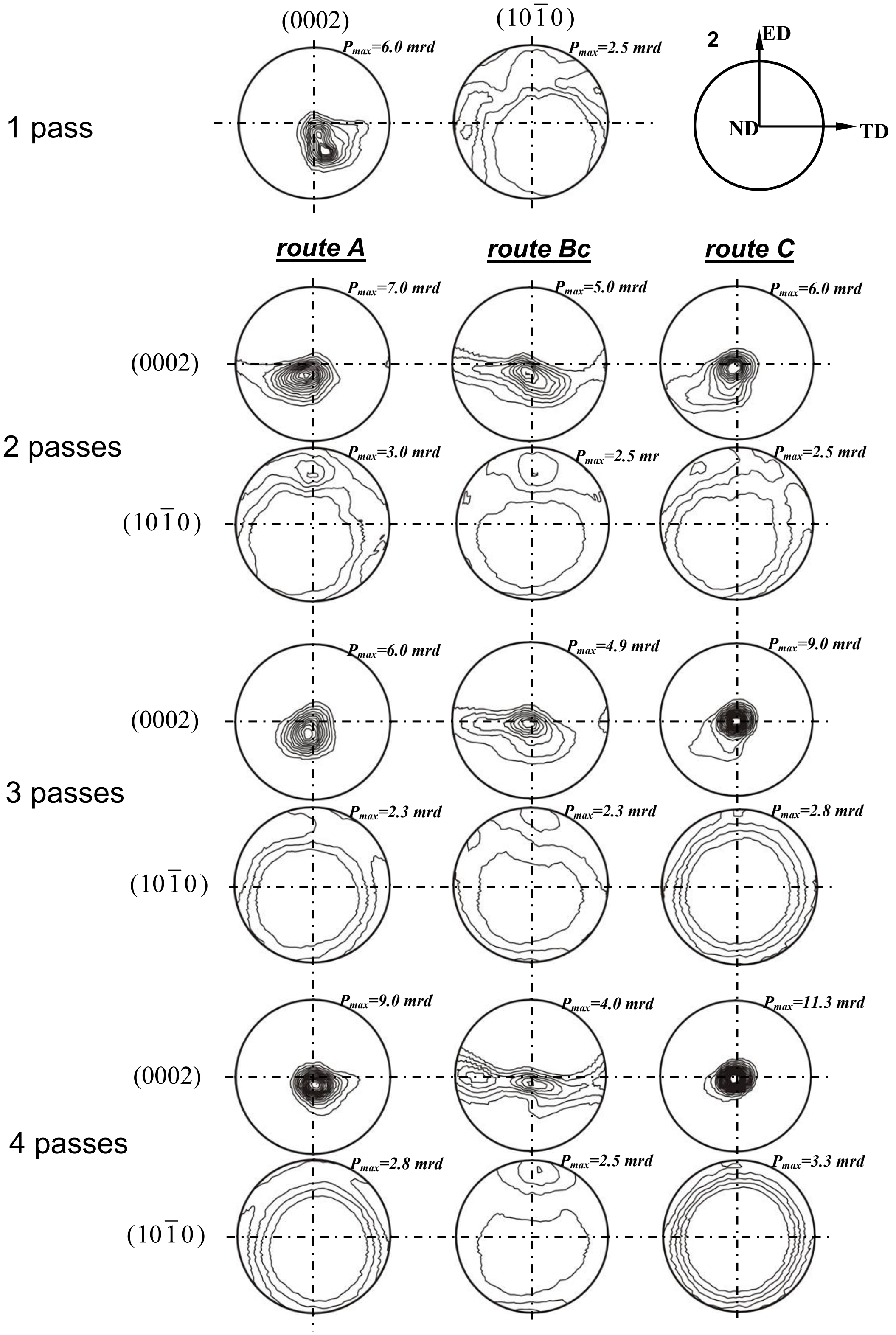

Fig. 5-5 (0002) and $(10\bar{1}0)$ complete pole figures on projection plane 2 of the as-cast pure Mg and the following ECAP processing from 1 pass up to 4 passes with three routes of A, Bc and C (Contour levels=1.0×, 1.5×, 2.0×, 2.5×, …).

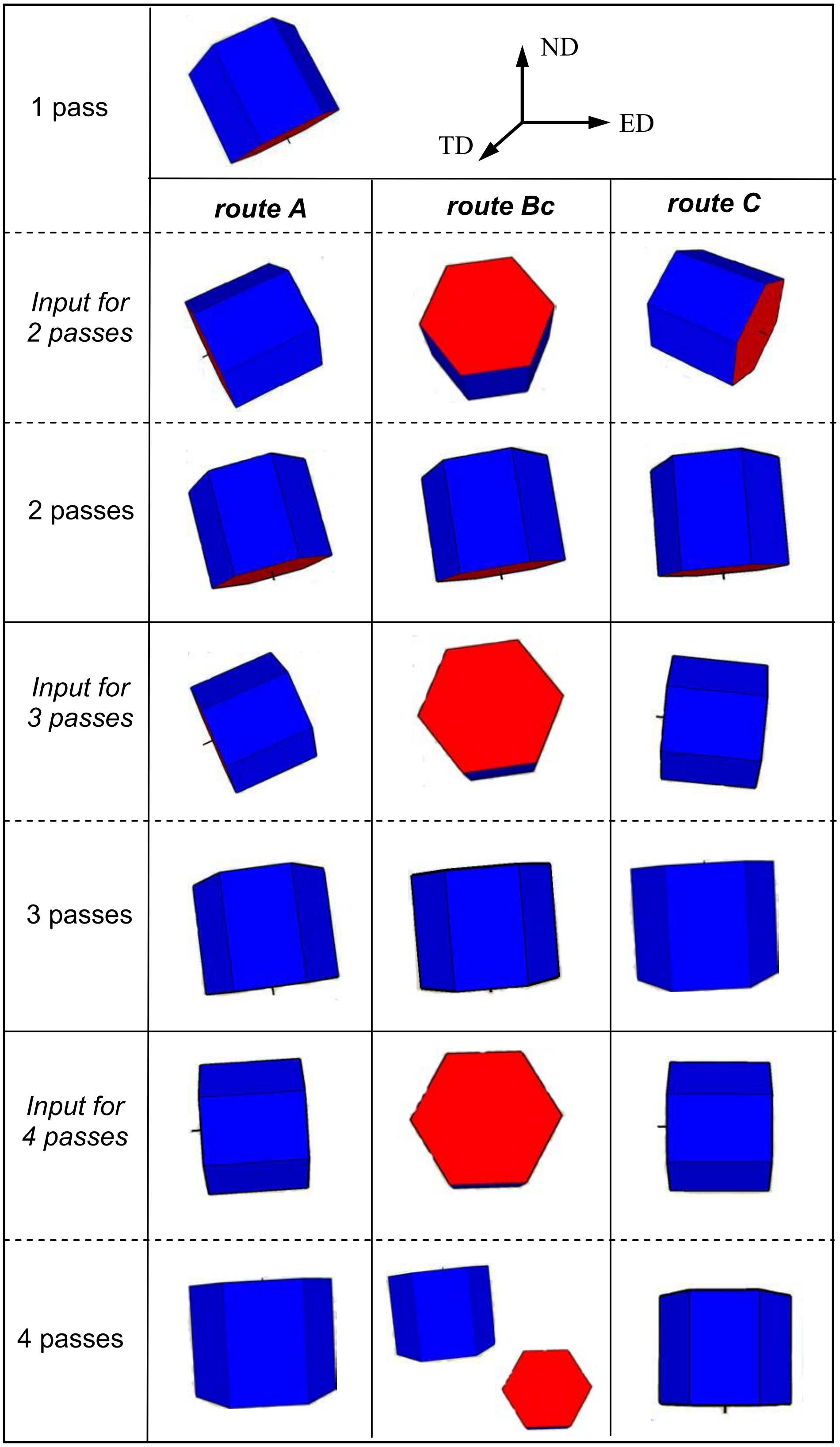

Fig. 5-6 Schematic illustration of the evolution of an ***hcp*** cell of the input and output texture after each passes ECAP processing by three routes.

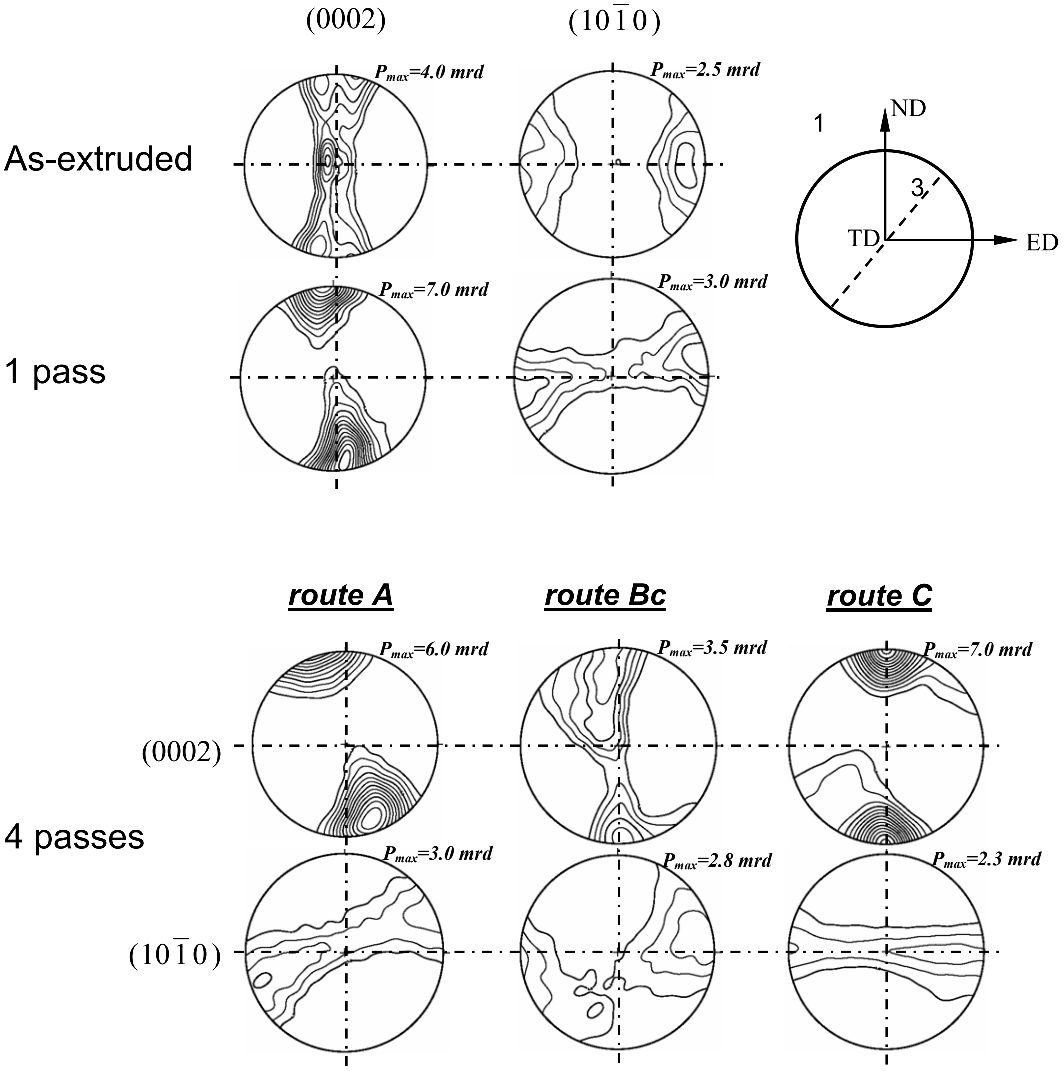

Fig. 5-7 (0002) and $(10\bar{1}0)$ complete pole figures on projection plane 1 of the extruded pure Mg and the following 1 pass and 4 passes ECAP with three routes of A, Bc and C (Contour levels=1.0×, 1.5×, 2.0×, 2.5×, …).

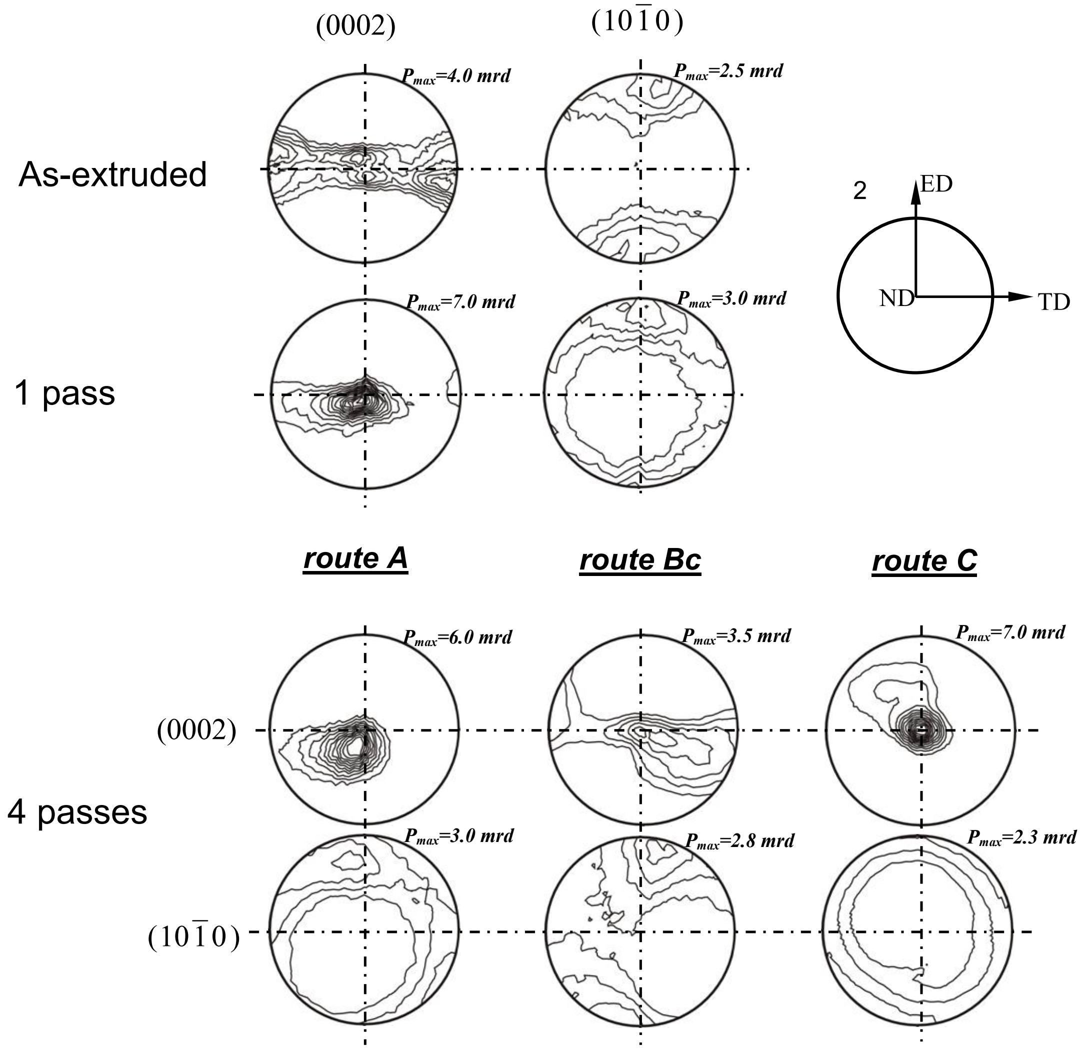

Fig. 5-8 (0002) and $(10\bar{1}0)$ complete pole figures on projection plane 2 of the extruded pure Mg and the following 1 pass and 4 passes ECAP with three routes of A, Bc and C (Contour levels=1.0×, 1.5×, 2.0×, 2.5×, …).

5.2 Mg-Si alloy

ECAP texture of as-cast Mg-Si

Fig. 5-9 shows the (0002) and $(10\bar{1}0)$ complete pole figures on projection plane 1 of as-cast Mg-Si alloy and the following 1, 2, 4 and 8 passes ECAP via three different routes of A, Bc and C, respectively. Pole figures on projection plane 2 are correspondingly shown in Fig. 5-10. After 1 pass processing the <00.2> fiber with its axis a 20° oft from the ND and an asymmetry around the ED is formed. With route A processing after 2 passes, oft angle of the <00.2> fiber axis to the ND is decreased and has an inverse rotation around the ED when looking on projection plane 2. Followed by 4 and 8 passes, the <00.2> fiber is retained with the increase of maximum intensity; but the asymmetry angle to ED varied from each pass when looking on projection plane 2.

With route Bc processing, the <00.2> fiber axis is re-orientated at about 5° to the ND with a weak girdle distribution along the TD when looking on projection plane 2 after 2 passes. No distinct change is found in the following 4 passes and 8 passes processing except a small decrease of the maximum intensity, which is attributed to the 90° rotation after each pass leading to a randomization of the former pass texture.

With route C processing, a complete compressive fiber with its ***c***-axis parallel to the compression direction ND is formed after 2 passes. This basal fiber is retained stable during the following 4 and 8 passes processing. And an obvious maximum with 11.3 mrd is obtained after 8 passes processing.

ECAP texture of as-extruded Mg-Si

(0002) and $(10\bar{1}0)$ complete pole figures on projection plane 1 and 2 of the hot extruded Mg-Si alloy and the following ECAP from 1 pass up to 8 passes with three route A, Bc and C are shown in Fig. 5-11 and Fig. 5-12, respectively. The quadratic extruded Mg-Si texture consists of a central component visible inside the (0002) pole figure with and a weak shear component. After 1 pass the <00.2> fiber with its axis 10° oft from the ND and a girdle distribution along the TD (looking on projection plane 2) is formed. An increase of the maxima from as-extruded of 3.5 mrd into 5.5 mrd is noted.

With route A processing from 2 passes up to 8 passes, similar trend evolution of the <00.2> fiber is obtained as those in pure Mg excepting the obtaining of comparatively low texture intensity. However, a combination of the newly formed <00.2> fiber and the retained component coming from the input texture was obtained after 2 passes with route Bc, which is similar as a quadratic extruded texture when looking on projection plane 2.

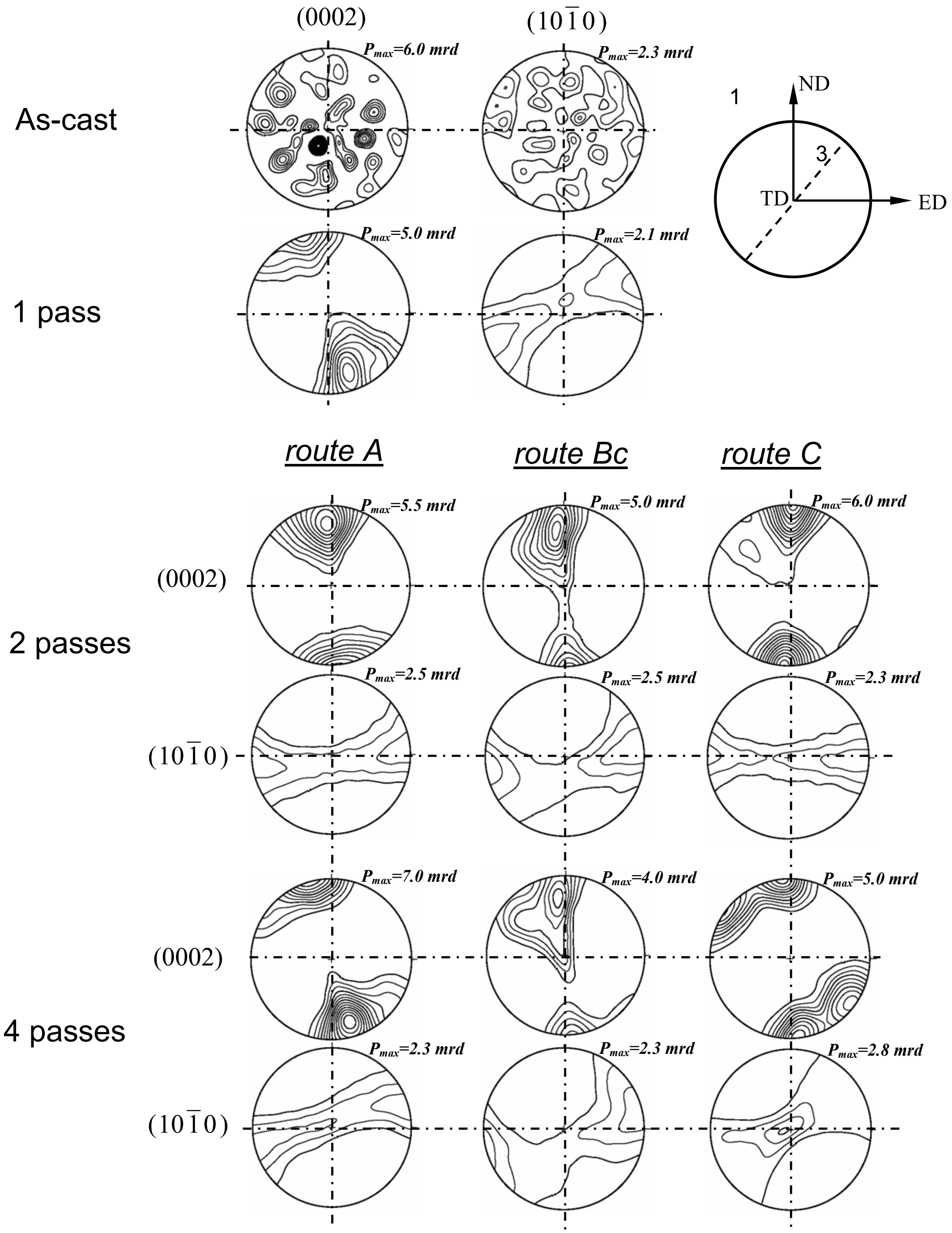

Fig. 5-9 (0002) and $(10\bar{1}0)$ complete pole figures on projection plane 1 of the as-cast Mg-Si alloy and the following 1, 2 ,4 and 8 passes ECAP with three routes of A, Bc and C (Contour levels=1.0×, 1.5×, 2.0×, 2.5×, …).

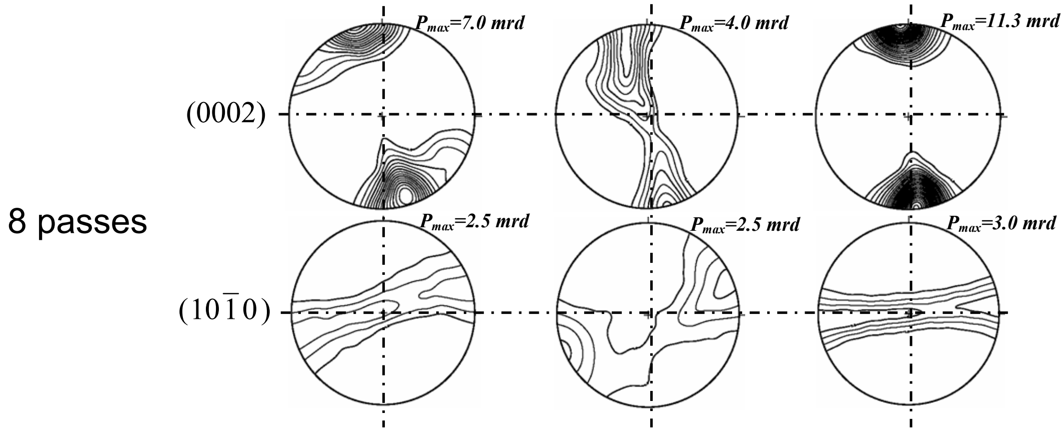

Fig. 5-9 Continued.

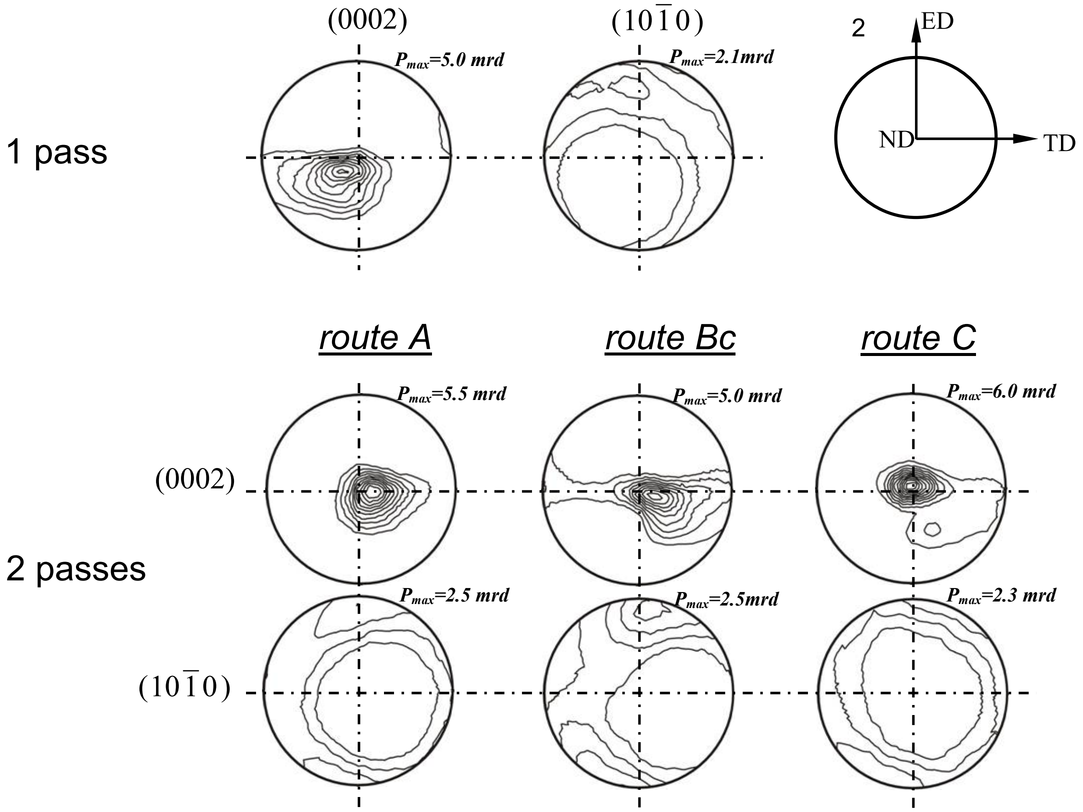

Fig. 5-10 (0002) and $(10\bar{1}0)$ complete pole figures on projection plane 2 of the as-cast Mg-Si alloy and the following 1, 2 and 4 passes ECAP with three routes of A, Bc and C (Contour levels=1.0×, 1.5×, 2.0×, 2.5×, …).

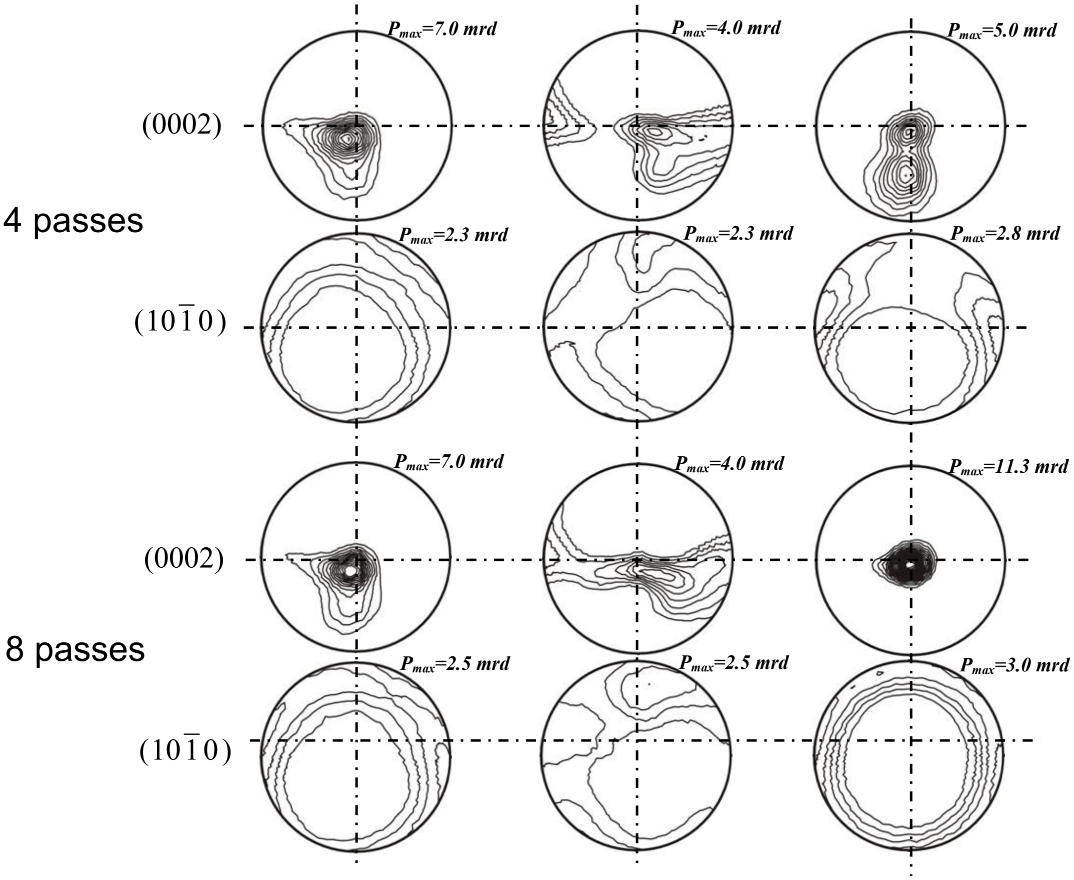

Fig. 5-10 Continued.

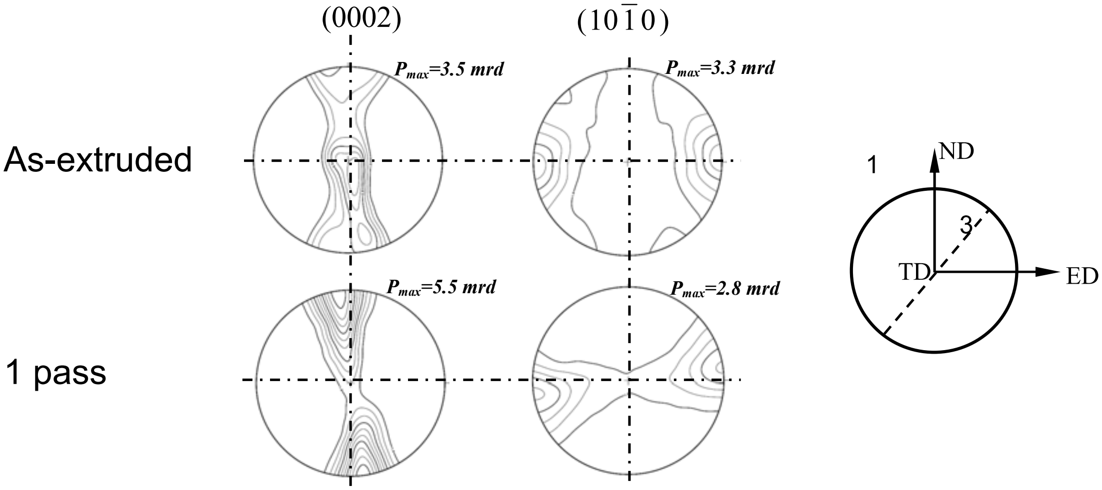

Fig. 5-11 (0002) and $(10\bar{1}0)$ complete pole figures on projection plane 1 of the as-extruded Mg-Si alloy and the following 1, 2, 4 and 8 passes ECAP with three routes of A, Bc and C (Contour levels=1.0×, 1.5×, 2.0×, 2.5×, …).

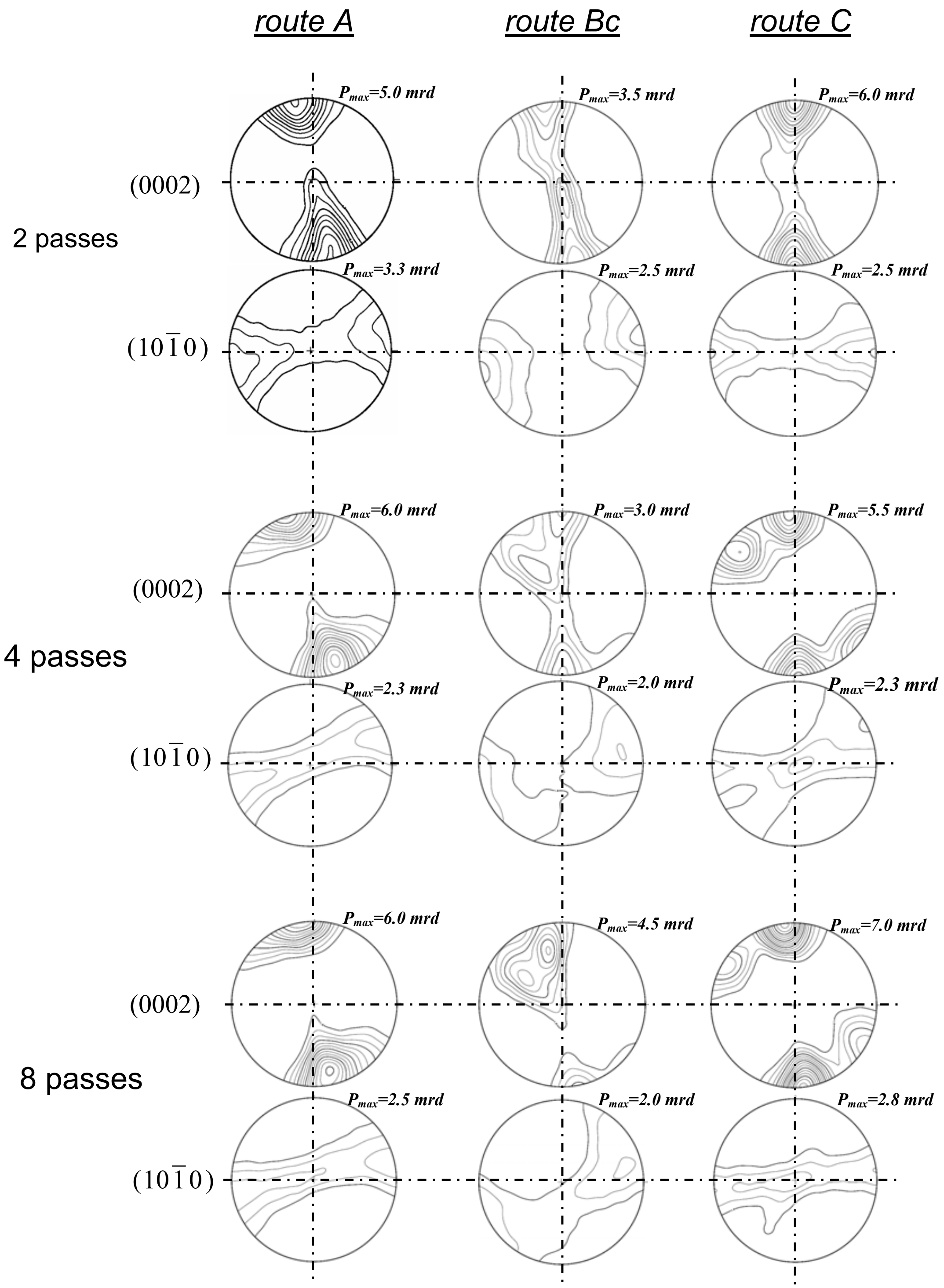

Fig. 5-11 Continued.

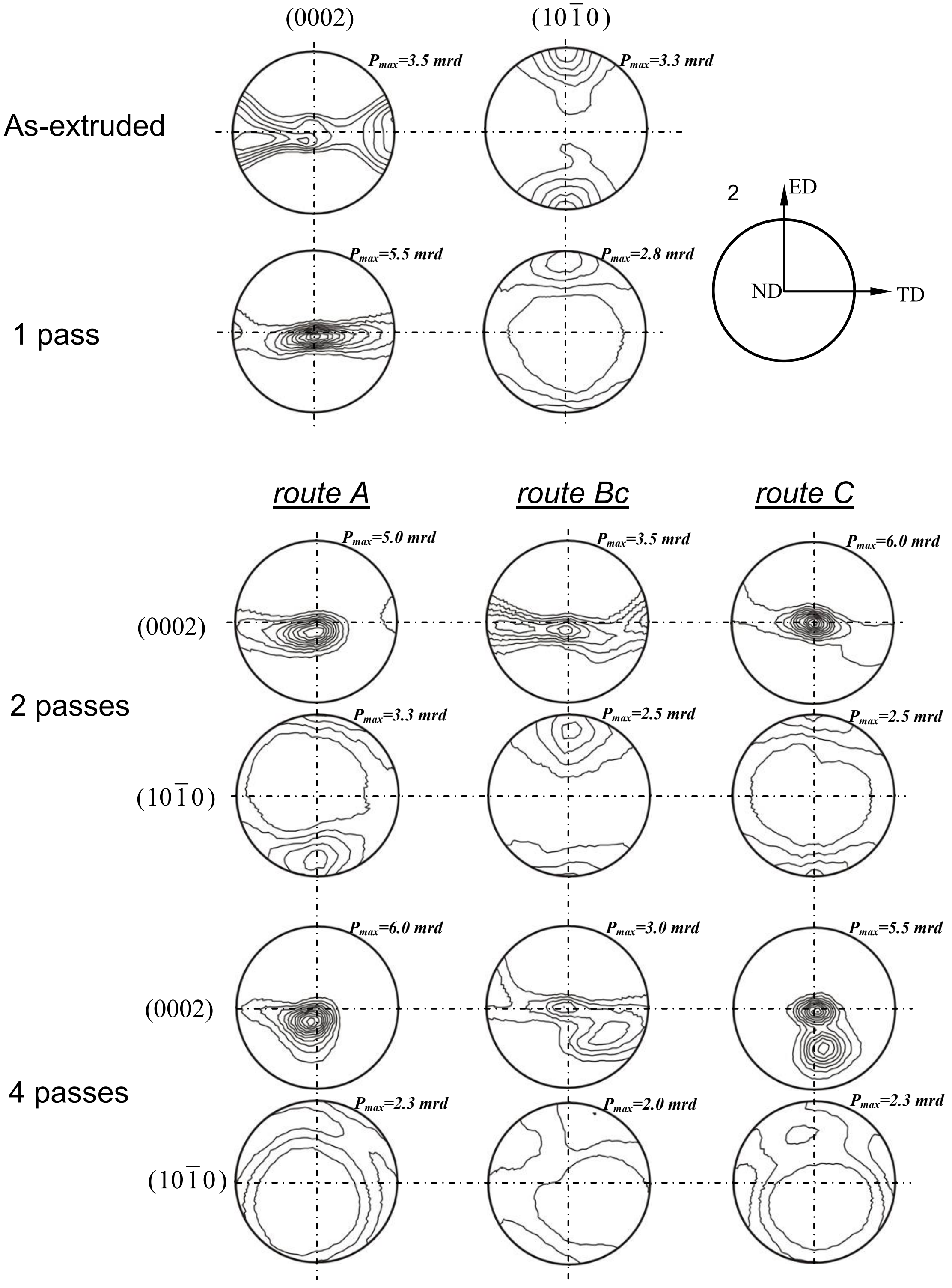

Fig. 5-12 (0002) and $(10\bar{1}0)$ complete pole figures on projection plane 2 of the as-extruded Mg-Si alloy and the following 1, 2, 4 and 8 passes ECAP with three routes of A, Bc and C (Contour levels=1.0×, 1.5×, 2.0×, 2.5×, …).

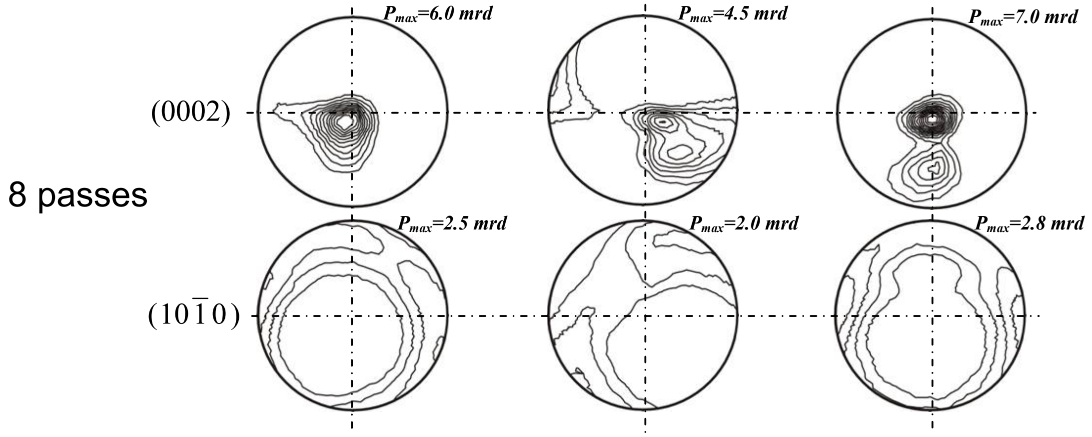

Fig. 5-12 Continued.

5.3 Discussion

Texture analysis is of great relevance to the mechanism of grain refinement during ECAP. Till present textures corresponding to various cases of ECAP and die angles have been investigated or modeled. ECAP is an effective technique to control texture strength and orientation [101]. Compared to conventional techniques ECAP offers a large variety of parameters for texture evolution. Two of them, the number of passes and the deformation route, are the most important. Represented publishes about the ECAP-processed ***fcc***, ***bcc*** and ***hcp*** materials' texture are documented here. Texture investigations on the ECAP-processed A5056 by route C showed that the components with an increase of sharpness very closing to the stable orientations predicted by the Taylor model of polycrystalline deformation for plane strain compression with relaxed constrained [118]. And the mainly so called copper-orientation {112} <111> and brass-orientation {110} <112> but was rotated by 15° around transverse direction, probably due to additional shear stresses which arise from frictional forces and backpressure. ECAP texture developed in Al- 0.13 % Mg via route C indicated that the main components were the {001} <110> and {112} <110> fiber with a rotation ~15-20° about the TD, this rotation was proved to occur as a consequence of the additional plane strain compression component by simulation [119]. As for ***hcp*** crystal structure materials, textures developed in Mg is one of the most attractive studies. Considered broadly, ECAP processing of Mg alloys tends to produce a certain class of textures regardless of the alloy or processing route. This class of texture is defined generally as <0001> // ND fiber textures [102]. Texture development in the ECAP-processed AZ61 was also described by the transformation of non-basal components [103]. It can be found that ***fcc*** and ***bcc*** polycrystalline materials can develop different texture components which record the information about the deformation or recrystallization. Moreover, ***hcp*** materials develop a basal fiber texture in most thermal-mechanic deformation process, which should be due to its inner crystallographic feature that has limited activated slip system. In addition, the polycrystal simulations also reveal that, despite significant changes of entry textures and strain path in multiple passes, the deformation in each pass is large enough to re-orient grains to the ideal fibers such that shear-type ECAP textures can be re-established. It is suggested that the rotation of local (or simple shear) reference system from the laboratory (or ECAP) reference system needs to be taken into account in ECAP texture analyses. It is noted that current input texture for ECAP has a common feature which the basal planes are parallel to the compression direction, or to say the compression direction is normal to the ***c***-axis. The $\{101\bar{2}\}$ twinning is thus most easily activated when the ***c***-axis is perpendicular to the compression stress (twinning under ***c***-axis extension). Jin et al. [115] has proposed a model which indicated that twinning greatly contributed to the formation of basal texture. The $\{10\bar{1}\bar{2}\}$ twinning can reorient the basal plane nearly normal to the compress stress direction which is the main origin of the basal fiber texture.

Remarkable is the less or even no shear influence on the ECAP-processed texture. Geometry of ECAP device and processing parameter should also be responsible. Kim et .al [127] has demonstrated that a lesser shear zone (LSZ) in the outer part of the work piece occurs when the corner angle of the die is nonzero because of the shorter travel path of the outer part within the main deformation zone in that case. Larger the outer arc curvature angle the more inhomogeneous deformation occurs, which weakens the theoretical 45° shear effect. Secondly, processing parameters, especially the temperature and pressing speed, also plays an important role in producing the basal fiber texture. High processing temperature accelerates the DRX process during and after the work piece passes through the 90° channel. It is known that a strong basal texture or near basal texture usually develops in a rolled Mg alloys. Hence, DRX, especially continuous DRX, is the main reason for the development of the basal texture [115]. Effect of the pressing speed is greatly related to the temperature though there is still limited number of related investigations. Since the present measured texture is a global texture over the whole thickness of the work piece after ECAP, existence of the local shear component is possible. This will be in detailed discussed in the next chapter by synchrotron diffraction.

It is also noted that asymmetry around the ED is observed in each ECAP-processed material. Table 5-1 summarizes this evolution in both ECAPed pure Mg and Mg-Si alloy, the asymmetric angle is defined as α. Remarkable is that this misfit angle α varies between -13° and +17°. Similar results have been published but the reasons are still under discussion [138]. This misfit angle shows a variation which cannot be explained by the ECAP process itself. Theoretically ECAP processing will lead to monoclinic pole figure symmetry with a symmetry axis from ECAP-direction to the TD-direction. But current measured results indicated a rotation stress is acted on the billet when it passes through the 90° channel. This rotation shear stress around the ED should come from the construction of the die. Since the current ECAP die consists two separated parts with the deformation channel totally in one side and it is fastened by 12 screws around it, the billet can be rotated when passes through the 90° channel because of the concentration of the stress near this channel. Hence, fasten and friction condition of the die leads to the variation of this asymmetry around the ED. Researches by Segal [139] using the slip line method indicates that different friction in channels results in non-uniform, variable deformation mode and the complicated loading history. A uniform strain distribution is remained with a decrease of effective strains when friction increases from zero to maximum; and the deformation mode changes from simple shear along the bisector plane for zero friction to combinations of three simple shears along fan boundaries and into the flow direction for intermediated friction. For maximum friction, deformation mode corresponds to simple shear into the flow direction. While it is difficult to estimate the effect from fasten and friction during ECAP. It can be concluded from the above analysis that ECAP processing under current die setting is a combination of rotation and shear stress; and basal planes slip accommodated by twinning is the main deformation mode. In order to highlight the shear effect, it is also suggested here a better improvement for constructing an entire die with the 90° channel inside and also to decrease the friction from die channel walls.

Comparing with the textures obtained by three different rotation routes, no distinct difference is found except that a gradual decrease of the texture intensity developed by route Bc processing. Effects from the accumulative effective shear end input texture are responsible. Schematic illustration of the slip system of four processing routes for consecutive pass is already shown in Fig. 2-12. Remarkable is that route Bc and C are both so-called redundant process but have different effect on the texture evolution. Looking on the input texture for route A and C processing compressive stress is nearly parallel to the ***c***-axis which is similar as rolling process, more basal planes are then re-orientated to the compression direction (ND). However, compressive stress is normal to the ***c***-axis with route Bc processing which means that these preferred grains must be re-rotated during ECAP. Re-orientation processing of the grains weakens texture. Moreover, the strain hardening behavior also varies with input texture. The ECAP-processed billet via route Bc should exhibit a stronger strain hardening behavior than those via route A and C processing.

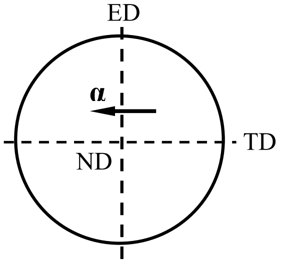

route A	**cast pure Mg**		**cast Mg-Si alloy**	
	P_{max}	α	P_{max}	α
1	6.0	-10	5.0	17
2	7.0	10	5.5	-13
4	9.0	5	7.0	11
route Bc	P_{max}	α	P_{max}	α
1	6.0	-10	5.0	17
2	7.0	10	5.5	-13
4	9.0	5	7.0	11

Tab. 5-1 List of the asymmetry angle α around the ED according the definition in (0002) pole figure (left) in ECAP-processed pure Mg and Mg-Si alloy.

5.4 Summary

(1) In general, a <00.2> basal fiber with its fiber axis having an oft angle to the TD is formed in current ECAP-processed pure Mg and Mg-Si alloy via all three routes of A. Bc and C. Asymmetry around the ED is obtained and varied with different routes and pass, which is attributed to the mismatch flow rate of the work piece and the friction condition of the device.

(2) Remarkable is the less shear effect, which is attributed both to the construction of the device and the materials inner structure. Construction of the die, the pressing temperature and speed, especially the existence of the outer curvature angle, are responsible. Activation of the basal slip is always preferred in coarse-grained Mg accommodating by twinning. ECAP of the starting coarse grained Mg at relatively high temperature has the similar deformation behavior as that hot compression or rolling of Mg since that DRX is easily happened.

(3) Texture intensity is getting stronger with the increase of processing pass via route A and C processing, while this is vice versa by route Bc processing. Existence of Si to form Mg_2Si in Mg greatly weakens the texture comparing with pure Mg. The initial texture just has limited effect on the texture evolution at first 2 passes.

6. Tensile mechanical behavior of the ECAP-processed Mg

6.1 Pure Mg

ECAP-processed as-cast pure Mg

Tensile stress-strain curves at room temperature of as-cast pure Mg and following ECAP from 1 pass up to 4 passes with route A, Bc and C processing are shown in Fig. 6-1 (a), (b) and (c), respectively. Variation of the 0.2 % yield tensile stress (YTS), the ultimate tensile stress (UTS) and the elongation to failure value with there processing routes are correspondingly illustrated in Fig. 6-2 (a) and (b), respectively. The as-cast pure Mg has an YTS of 25 MPa and elongation to failure value of 3 %. After 1 pass processing the YTS and elongation value are increased to 35 MPa and 4.5 %, respectively, which is mainly attributed to the great decrease of grain size after ECAP.

With route A processing tensile stress increases with processing pass and the YTS is nearly doubled after 4 pass processing compared with the as-cast condition, while the maximum UTS and elongation to failure value is obtained after 2 passes. Elongation to failure value is doubled from 1 pass to 2 passes including an increase of the tensile stress via route Bc processing; however, the ductility is sharply decreased after 4 passes excepting the increase of YTS. It can be found that evolution of the YTS and elongation to failure value via route C is similar as those obtained with route Bc processing.

Generally, room temperature tensile property of metals is greatly related to the grain size. According to Hall-Petch equation which states the relationship between yield tensile stress and grain size [120], decrease of the grain size will increase the YTS. However, texture also plays an important role on the deformation behavior [102-104]. Texture modification due to the different accumulative shear deformation with each route during ECAP processing can change the Schmid factor. Hence, variation of the tensile property is attributed to both the change of grain size and texture modification. Detailed effects of the different initial orientation on the mechanical behavior of Mg alloys were investigated and simulated by S. B. Yi and his co-workers [121].

Curves of the YTS against the square root of grain size $d^{-1/2}$ of ECAP-processed pure Mg with route A, Bc, and C are plotted in Fig. 6-3 (a), (b), and (c), respectively. With route A processing, as shown in Fig. 6-3 (a), grain size was greatly decreased from the as-cast to 1 pass which made the YTS greatly increase; however, the decrease of grain size was not so obvious from 1 pass to 4 passes but the YTS was greatly increased from the 35 MPa at 1 pass to 66 MPa at 4 passes which could be attributed to the texture strengthening effect. As shown in Fig. 5-2, basal planes in most grains orientated nearer to the center in (0002) pole figure and the pole intensity was increased from 7.5 mrd at 2 passes to 9.7 mrd at 4 passes. Hard orientation of the (0002) plane makes YTS increase and ductility decrease.

It can be found that the slope of the yield stress versus $d^{-1/2}$ is either positive or negative in the ECAP-processed Mg with route Bc processing. Small increase of the YTS occurs after 4 passes though there is an increase of average grain size. Similar results were previously obtained by the other investigators [77, 103], while this phenomenon was in contrary to the ECAP-processed Al alloys [122]. The negative slope of yield strength versus $d^{-1/2}$ in some ECAP-processed Mg materials may be also explainable by the texture transition that occurs progressively during repetitive ECAP to control the grain size, resulting in a lower yield stress at a higher pass number [103]. This suggests that the yield strength of the ECAP-processed Mg is not only controlled by grain size, the unique texture also plays an important role. Fig. 6-4 presents the ODF-sections at φ_2=0° and φ_2=30° of the ECAP-processed Mg after 2 passes and 4 passes processing, respectively. As can be found that a new shearing component at φ=70° occurred in the 4 passes processed billet, which indicated that high stress is needed to activate the slip system at the initial stage of the tensile test. Moreover, twinning was widely happened in large grains, as can be observed in Fig. 2 (f), twins can act as a barrier hindering the gliding of dislocations leading to the increase of the YTS [20, 21, 27].

Grain size decreased with the increase of processing pass via route C before 2 passes processing, as shown in Fig. 6-3 (c), the YTS was also increased. While YTS was increased with the increase of grain size after 4 passes processing which was not in accordance with the Hall-Petch law. The formation of a strong as 11.3 m. r. d. rolling type texture after 4 passes processing made the basal planes have a nearly to zero Schmid factor which greatly contributed to the increasing of YTS.

The maximum elongation to failure of the ECAP-processed Mg with three different routes processing was obtained at 2 passes. Due to the growth of large number of grains during the following passes processing after 2, elongation to failure was greatly decreased. Especially, existence of the large number of twins in those grains with route Bc processing decreased the ductility. Moreover, the modified textures which basal planes tended to parallel to the extrusion plane also made the elongation to failure decrease.

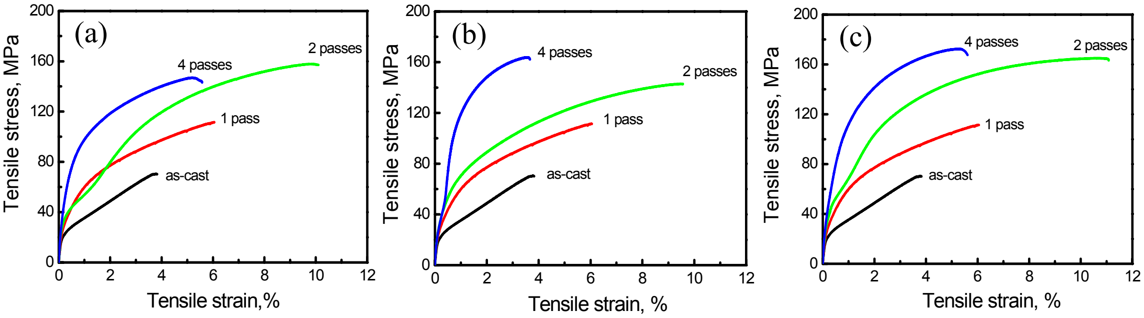

Fig. 6-1 Tensile stress-strain curves of the ECAP-processed as-cast pure Mg from 1 pass to 4 passes with (a) route A, (b) route Bc, and (c) route C, respectively.

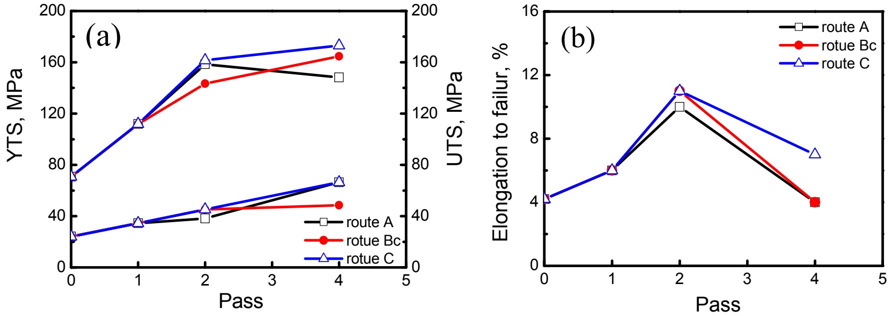

Fig. 6-2 Variation of (a) YTS and UTS, (b) elongation to failure with the processing pass of the ECAP-processed as-cast pure Mg with three routs of A, Bc and C, respectively.

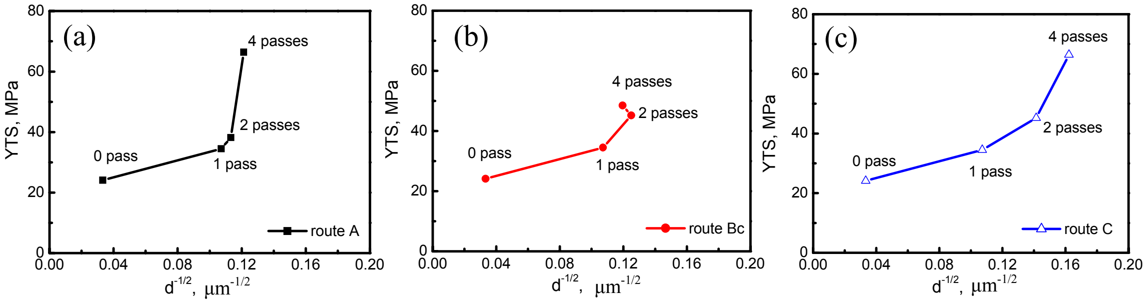

Fig. 6-3 Curves of the YTS (0.2% yield stress) against the square root of grain size $d^{-1/2}$ of the ECAP-processed pure Mg with different routes of (a) route A, (b) route Bc, and (c) route C.

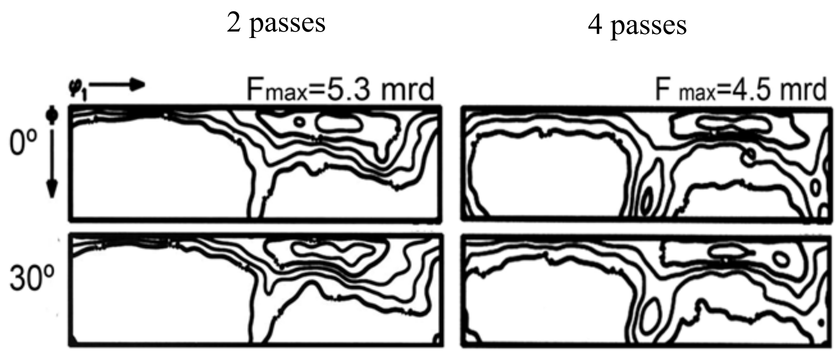

Fig. 6-4 ODF-sections at φ_2=0° and φ_2=30° of the ECAP-processed pure Mg at 2 passes and 4 passes with route Bc processing (Contour levels= 1.0 ×, 2.0 ×, …).

ECAP-processed as-extruded pure Mg

Tensile stress-strain curves of as-extruded pure Mg and the following ECAP processing from 1 pass to 4 passes via three routes of A, Bc and C are shown in Fig. 6-5 (a), (b) and (c), respectively. Similarly, variation of YTS, UTS and elongation to failure are shown in Fig. 6-6 (a) and (b), respectively. The YTS is doubled after hot extrusion which is due to the decrease of the grain size from 900 μm of as-cast to 38 μm, and as well the existence of the strong extrusion fiber texture. After 1 pass tensile stress was increased and the elongation to failure value was also increased from the as-extruded of 5 % to 8 %, which the main reason should be attributed to the formation of strong texture which basal planes in most grains nearly parallel to the tensile direction besides the small decrease of the average grain size comparing with the as-extruded condition. Followed by 2 passes and 4 passes processing via route A, tensile stress and elongation to failure value are both decreased due to the weakening of texture besides the small increase of grain size. Similar trend is found with route C processing till 4 passes. However, tensile stress decreases with the increase of pass with route Bc processing while the elongation to failure is on the contrary, which is mainly attributed to the texture effect.

It can be found from Fig. 6-6 that the tensile stress and ductility via route Bc processing are both higher than those with the other two routes processing at the same pass, which indicates that routes Bc processing is relatively effective to improve the mechanical properties of the as-extruded pure Mg at the present work.

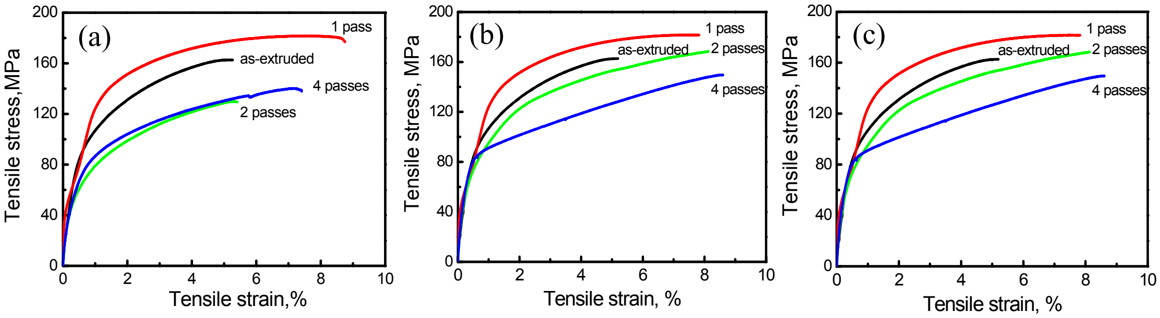

Fig. 6-5 Tensile stress-strain curves of the ECAP-processed as-extruded pure Mg from 1 pass to 4 passes with (a) route A, (b) route Bc, and (c) route C, respectively.

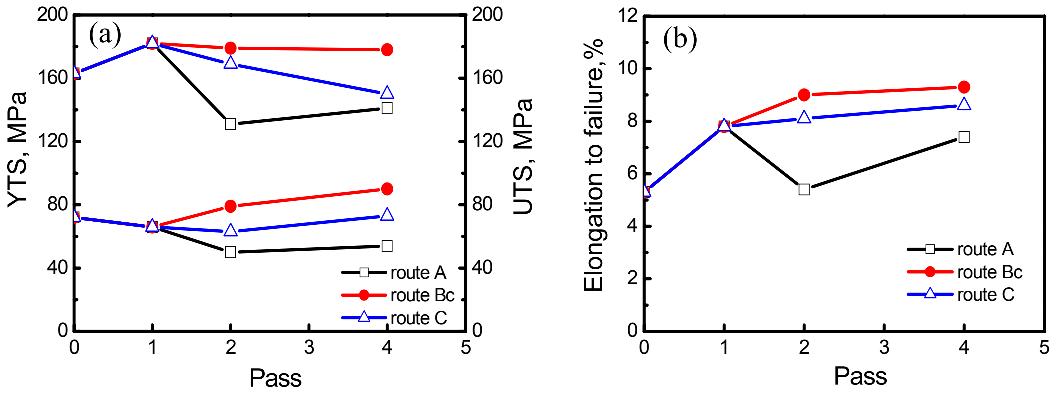

Fig. 6-6 Variation of (a) YTS and UTS, (b) elongation to failure with the processing pass of the ECAP-processed as-extruded pure Mg with three routs of A, Bc and C, respectively.

6.2 Mg-Si alloy

<u>ECAP-processed as-cast Mg-Si alloy</u>

Room temperature tensile stress-strain curves of ECAP-processed as-cast Mg-Si alloy from 1 pass to 8 passes with route A, Bc and C are shown in Fig. 6-7 (a), (b) and (c), respectively. After 1 pass the UTS and elongation to failure value are increased from the as-cast of 77 MPa and 1.2 % to 151 MPa and 3 %, respectively. With route A processing, as shown in Fig. 6-7 (a), the YTS is increased with the increase of processing pass until 8 passes; and the maximum elongation to failure value is doubled after 2 passes followed by a 2/3 increase after 4 passes, then was decreased into the same value as as-cast condition after 8 passes. With rout Bc processing the UTS is gradually increased from 1 pass to 8 passes; and the largest elongation to failure value of about 6 % is obtained after 2 passes then gradually decreased after 4 and 8 passes processing. With route C processing the 2 passes processed billet has the similar tensile behavior as that 1 pass processed excepting a small increase of UTS; and 4 passes processed billet has the largest elongation to failure value but has the lowest UTS.

As for Mg-Si alloy, grain size and homogeneous redistribution of the hard second Mg_2Si particles is another key factor that is also responsible for the tensile behavior of ECAP-processed billet besides the size and texture of matrix grains. Nearly double increase of the tensile stress and ductility after 1 pass ECAP is mainly due to the great refinement of grain size of matrix and as well Mg_2Si particels which can has been described in Fig. 4-6 and Fig. 4-7. SEM microstructures on the tensile fracture surface of as-cast and ECAP-processed Mg-Si alloys are given in Fig. 6-8. Elongated large brittleness cleavage cracks across the coarse matrix grains are observed in Fig. 6-8 (a) in as-cast Mg-Si alloy, and as well the cracks along Mg_2Si particles. Small dimples of matrix grains and cracks along Mg_2Si particles exited in the 1 pass ECAP-processed billet.

As for the ECAP-processed billet with route A processing, there is a trend that the tensile stress and ductility increase with the processing pass except a rapid decrease of the ductility after 8 passes processing. Similar results were obtained in other ECAP-processed materials [122] which is attributed to the evolution of microstructures formed by the same continuous shear deformation with route A. Gradient increase of the maximum intensity and its orientation moves to the pole figure center, as can be obtained from Fig. 5-7, makes Schmid factor of the basal planes in most grains decrease which strengthening the material. However, the ductility after 8 passes processing is extremely low though the tensile curve exhibits a relatively higher tensile stress. This could be attributed to the effect of Mg_2Si particles, as has been described that the dendritic eutectic Type-II Mg_2Si is gradually broken and homogeneously re-distributed with the increase of processing pass. Homogenization of Mg_2Si particles can effectively hinder the mobile dislocation. Increase of tensile stress of polycrystals is greatly related to the accumulation of dislocations on the grain boundaries of matrix grains or second phase [123-125]. Accumulation of dislocations around Mg_2Si particles increases the local stress; therefore cracks occur around particles when this stress is larger than the binding stress between Mg_2Si and matrix Mg, as shown in Fig. 6-8 (f), cracks around Mg_2Si boundaries are observed. It should be mentioned here that cracks are also observed in 4 passes ECAP-processed billet, but totally less than those in 8 passes ECAP-processed billet. Inter-grain propagation of cracks easily happens in the more homogeneous distributed particles in Mg-Si alloy which makes the 8 passes ECAP-processed billet have a very low ductility.

As for the tensile behavior of billets via route Bc processing, there is a distinct difference on the ductility. Microstructures, especially the refinement and redistribution of Mg_2Si phase with route Bc processing, is more complicated which is due to the alternate 90° shearing as compared to route A processing. Researches have shown that rout Bc in nature is a redundant shear which slip in the first pass is cancelled by slip in the third pass and slip in the second pass is cancelled by slip in the forth pass, and so on [47, 54]. Hence, redistribution of the broken Mg_2Si particles is different as route A processing. Maximum elongation to failure value was obtained after 2 passes processing which should attributed to the effect of Mg_2Si since the there is no evident difference in the texture, as shown in Fig. 5-7, the maximum pole intensity stables after 2 passes. Similar results were also obtained in the ECAP-processed hypoeutectic Al-Si casting alloy which was considered to be attributed to the dependence of the fracture propagation path on the processing route due to different geometric redistribution of the eutectic constituent [126]. Propagation path of the final crack is different in the billets with different routes processing. Redistribution of the broken Mg_2Si along the shearing deformation direction at 1 pass was weakened after 2 passes processing due to the 90° rotation of the billet which randomized the Mg_2Si particles. The SEM fracture surface microstructure observation in Fig. 6-8 (d) and (g) shows that there exited more cracks around Mg_2Si particles than those with route A processing. More randomization of Mg_2Si particles increased the tensile stress; and also increased the local stress concentration which easily active the formation of cracks. Propagation of cracks around hard Mg_2Si particles is the main fracture mechanism of ECAP-processed billet via route Bc processing.

Tensile behavior of ECAP-processed billets with route C is similar as those with route A. Strong as a rolling type texture was tended to form with the increase of processing pass except a double maximum occurred after 4 passes. Obtaining of the maximum elongation to failure value after 4 passes processing is mainly attributed to the uniform texture which basal planes in many grains orientated about 45 ° to the tensile direction, as shown in Fig. 5-7.

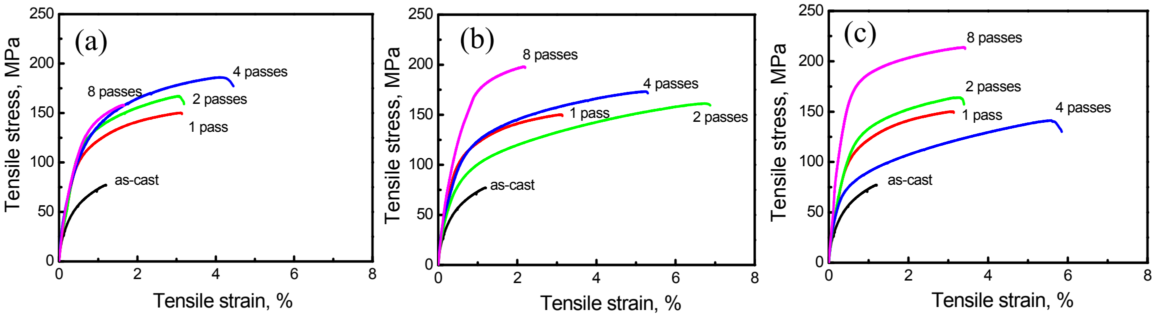

Fig. 6-7 Tensile stress-strain curves of the ECAP-processed as-cast Mg-Si alloy from 1 pass to 8 passes with (a) route A, (b) route Bc, and (c) route C, respectively.

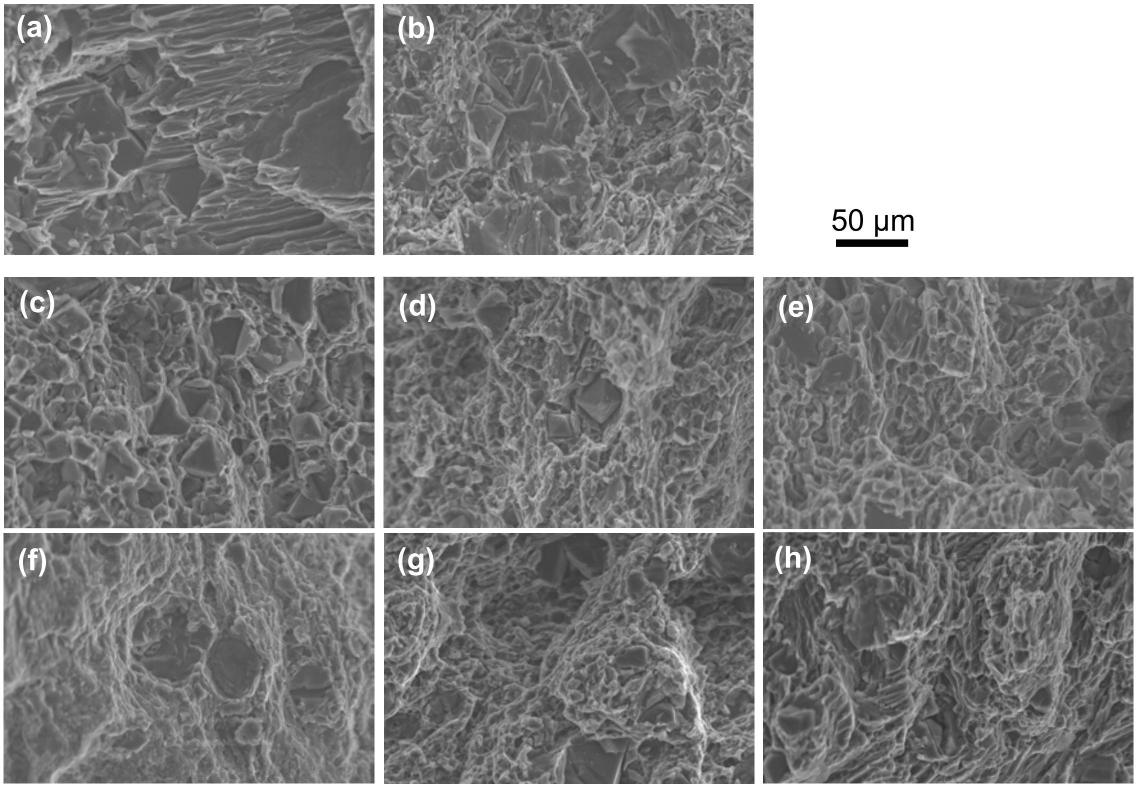

Fig. 6-8 SEM microstructures on the fracture surface of the tensile specimens Mg-Si alloys of (a) as-cast, ECAP-processed (b) 1 pass and with route A at (c) 4 passes and (f) 8 passes; route Bc at (d) 4 passes and (g) 8 passes; route C at (e) 4 passes and (h) 8 passes, respectively.

ECAP-processed as-extruded Mg-Si alloy

Room temperature tensile stress-strain curves of the as-extruded Mg-Si alloy and the following ECAP from 1 pass up to 8 passes via three routes of A, Bc and C are shown in Fig. 6-9 (a), (b) and (c), respectively. After hot extrusion the UTS and the elongation to failure value are increased from the as-cast of 77 MPa and 0.8 % to 179 MPa and 2.5 %, respectively. Distinct improvement of the mechanical properties is attributed to the grain size decrease of matrix grains and Type-II Mg_2Si particles after hot extrusion, and as well the formation of strong basal fiber texture, as shown in Fig. 5-9. After 1 pass the YTS and UTS are both increased with a doubling of the elongation to failure value. No distinctly different of the grain size and redistribution of Mg_2Si phase are found from the OM microstructure in Fig. 4-8 and Fig. 4-9 comparing with the as-extruded. The Mg_2Si particles are redistributed parallel to the extrusion direction. However, a strong <0001> basal fiber texture with a maximum of 5.5 mrd was formed after 1 pass processing which indicated that basal planes in most grains orientated parallel to the extrusion direction, which greatly contributed to the improvement of the tensile stress.

With route A processing a small decrease of the YTS from 165 MPa into 106 MPa is obtained after 2 passes. Decrease of the YTS is remained in the following 4 passes and 8 passes. With route Bc processing, gradually decrease of the YTS from 1 pass to 4 passes is observed excepting a distinct increase of the elongation to failure value after 4 passes processing, as shown in Fig. 6-9 (b). Two reasons should be responsible for this sharp decrease of the YTS; firstly, redistribution of the Type-II Mg_2Si after a 90° rotation shearing which is different comparing to that via route A processing; secondly, two components with a decrease of maximum into 3.5 mrd occurrs in the pole figure which has been discussed in Fig. 5-9 which weakens the material. Formation of a weak maximum with 44° to extrusion direction in pole figure after 4 passes processing makes the elongation increase comparing with that after 2 passes processing.

With route C processing, due to the strengthening of a rolling type texture after 2 passes the elongation to failure value is decreased. Tensile stress and elongation to failure value are increased from 4 passes to 8 passes which is attributed to the formation of two maximum in (0002) pole figure and the strengthening of rolling component after 8 passes.

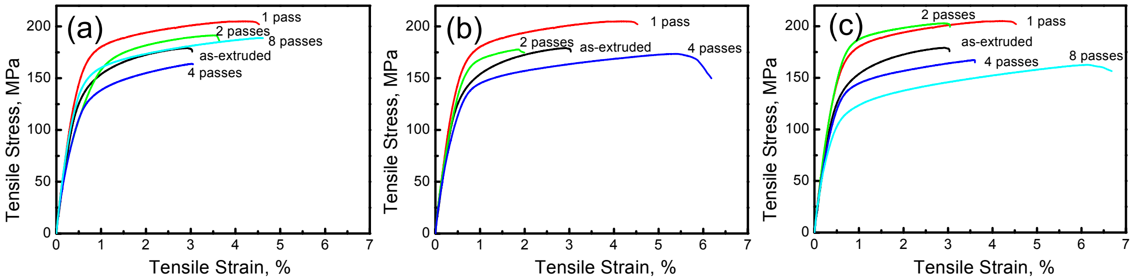

Fig. 6-9 Tensile stress-strain curves of the ECAP-processed as-extruded Mg-Si alloy from 1 pass to 8 passes with (a) route A, (b) route Bc, and (c) route C, respectively.

6.3 Summary

(1) As for the initial as-cast pure Mg, tensile stress was increased with the increase of processing pass via three routes processing; while the maximum elongation to failure was obtained at 2 passes processing which was due to the small grain size. Negative slope of the YTS versus square root grain size d $^{-1/2}$ was obtained in ECAP-processed pure Mg with route Bc and C processing. Texture strengthening effect was greatly contributed to this phenomenon but decreased the ductility in ECAP-processed billet after 4 passes processing.

(2) The maximum YTS in ECAP-processed as-extruded pure Mg was obtained after 1 pass; and then was gradually decreased together with the elongation to failure value after following pass processing. Relatively high tensile strength and ductility were obtained via route Bc processing.

(3) As for as-cast Mg-Si alloy, the YTS and elongation to failure value were both greatly increased with the increase of processing pass due to grain size refinement and more homogenization redistribution of Mg_2Si particles. Tensile stress was gradually increased with the increase of processing pass which was attributed to the homogeneous redistribution of refined Mg_2Si particles including the strengthening effect of basal fiber texture.

(4) Conclusively, distinct increase of the YTS and elongation to failure value were obtained in ECAP-processed both initial as-cast and as-extruded pure Mg, Mg-Si alloy just after single pass. As for the initial as-cast pure Mg and Mg-Si alloy, there was a similar trend that the YTS and ductility were both increased with the increase of process pass by all three routes. However, as for the input as-extruded materials the highest YTS value was obtained after first pass then decreased excepting an increase of the elongation to failure value. Besides the grains size effect, the different input texture played an important role on this tensile behavior.

7. Local texture analysis on the 50%-ECAP-processed pure Mg

Investigation on the texture homogeneity which is related to the deformation mode is significant to understand the evolution of texture at different plastic deformation stage. Present study is undertaken to investigate the textures at different region on a half ECAP-processed billet. Variation of textures at different position in the die will be analyzed by neutron and synchrotron diffraction. Textures evolution will be related to the deformation mode. In this research, the cast commercial pure Mg was first hot quadratic extruded at 340°C and then ECAP-processed. During ECAP the pure Mg billet was first inserted into the lubricated die then together heated to 350°C and holding this temperature for 30 min; and finally was pressed at a speed of 20 mm·min^{-1} and stopped after 50 % deformation. Thus the ECAP-processed pure Mg billet consists of a first part from the ingoing channel, a second part directly from the 90° die angle, and a third part from the quadratic outgoing channel after shear deformation. Macroscopic view of the half-ECAP-processed billet is shown in Fig. 7-1. Samples for texture measurement with neutrons were machined as schematically shown in Fig. 7-1 by dashed lines, in which two bulk samples at the ingoing and outgoing channels with each a dimension of 10×10×5 mm^3 and four small samples with a dimension of 4×5×10 mm^3 at the 90° angle region in the ECAP-processed billet.

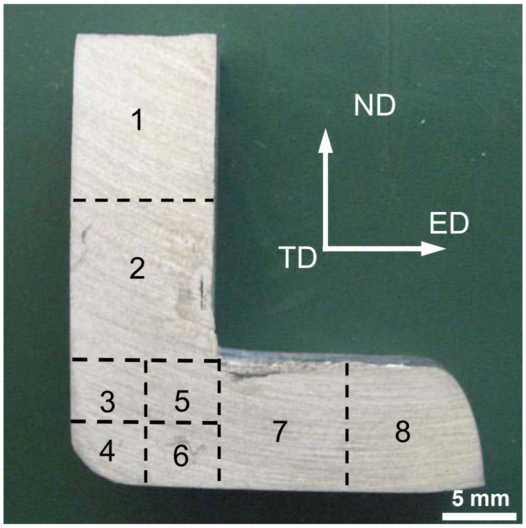

Fig. 7-1 Macroscopic view of the 50 % ECAP-processed pure Mg billet; and schematic shown of the samples for texture measurement with neutrons by dashed lines.

7.1 Microstructures

Optical microstructures of the 50 % ECAP-processed pure Mg at three different positions of ingoing, 90° angle, and outgoing channel are shown in Fig. 7-2 with low and high magnifications, respectively. Large as about 250 µm grains which surrounded by some small as 50 µm recrystallized grains were observed at the ingoing position. At the 90° deformation angle grain size was decreased and many twins were observed. Bi-modal grains distribution, which large as 100 µm and small as 20 µm, was obtained at the outgoing channel. Twins were still observed in some large grains. It should be mentioned that great grains refinement caused by DRX can be obtained. Twinning deformation plays an important role during ECAP. Inhomogeneous distribution of the grain size is notable.

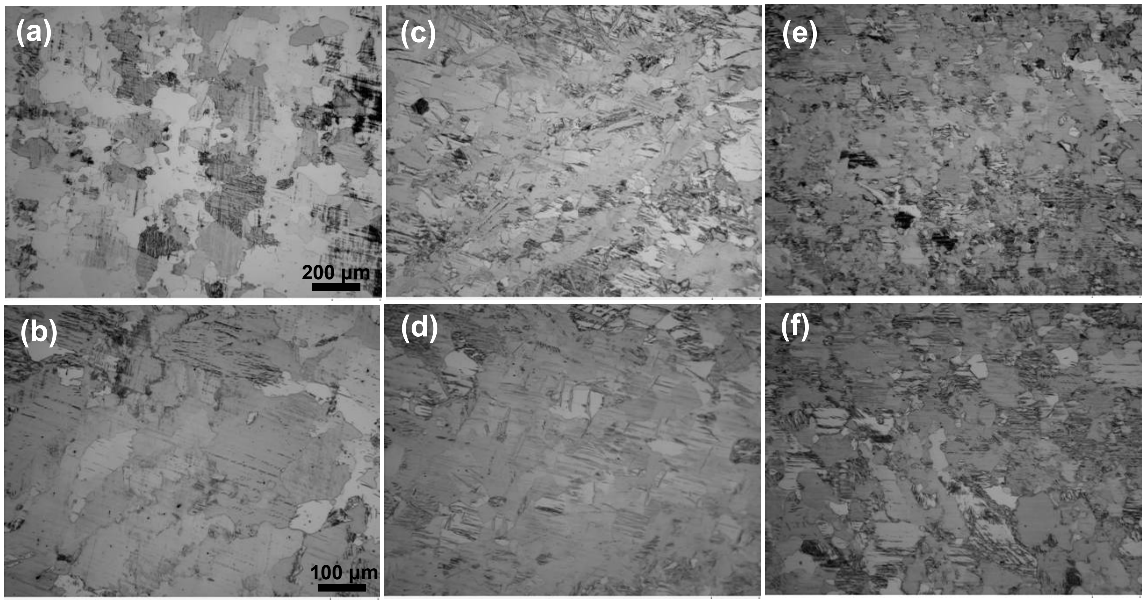

Fig. 7-2 Optical microstructures with low (the first row) and high (the second row) magnifications, respectively, of the 50 % ECAP-processed pure Mg at different positions of (a) and (b) ingoing channel, (c) and (d) middle at the 90° channel, (e) and (f) outgoing channel.

7.2 Textures by neutron diffraction

Fig. 7-3 shows the (0002) and $(10\bar{1}0)$ complete pole figures of the samples from ingoing and outgoing channels, in which pole figures of the small samples from position 3 to 6 are correspondingly illustrated in Fig. 7-4. The texture in sample 1 consists of a fiber texture component rotated about 10° from the ED and of a central maximum component visible inside the (0002) pole figure. Without the rotation this texture is related to the hot quadratic extrusion process before ECAP. Two reasons contribute to the texture rotation. Firstly an effect of asymmetric flow due to the ECAP device (90° angle) and secondly an unequal friction take part. The change to position 2 is small. A very weak intensity pole inside the central part of the (0002) pole figure occurs. No additional rotation was observed. Investigations on the homogeneity of stress and effective strain have been widely performed under finite element simulation [126-130]. Moreover, inhomogeneous distribution of the deformation strain rate has also been reported [131]. Thus, non-equal materials flow could therefore lead to the weak shear.

Looking on Fig. 7-4 with local textures in the 90° die region a continuous rotation of the fiber is observed from position 3 over position 5 and 4 to position 6. The final orientation at position 6 shows a fiber axis close to the transverse direction. Another evolution can be seen for the second texture component. The central maxima already started splitting at position 2 moves continuously outside. But at position 5 one can see a weak new texture 90° outside the central maximum which results from twinning. The amounts of twins are much stronger at position 6 than in position 5. Due to the heavy texture changes in this 90° die region synchrotron texture measurements were carried out, which will be thereafter discussed in detailed. Texture sharpness is nearly constant in the ingoing channel and in the 90° die region but volume fraction of different texture components vary. In position 6 the twin component is dominant with an orientation degree of 3.3 mrd.

The outgoing channel shows with two positions which we have investigated. Firstly, position 8 represents the beginning of the materials flow and secondly (position 7) a part directly after passing the shear zone. The (00.2) pole figure of position 8 includes an orientation girdle along the shear zone rotated about 45° to ED. Inside this orientation girdle one can see a double maximum already known from rolling textures in the rolling plane. A second texture component which is stronger describes grains oriented in the ND. But the total texture is relatively weak. It has to be noted that position 8 is a global texture over the whole thickness of the ECAP-processed sample. A texture gradient is expected and will be measured by synchrotron radiation.

Directly after passing shear zone the influence of shear zone is much weaker. A separation in time scales denotes that position 7 comes after position 8. The texture is much stronger with 5.0 mrd but more or less concentrated in one texture component. Only a small intensity girdle with about 50° to the ED is left. This asymmetry in the pole figures results from shearing. The texture in position 7 can be good correlated to the sample at position 6 which similar. The asymmetry in the (00.2) pole figure at position 6 results also from the shear but is much lower than 45°. A rotation of about 10° around the TD between position 6 and position 7 is visible. This rotation due to the inhomogeneous flow field during ECAP starts already at the beginning (sample position 1) and is finished for this experiment after passing the shear zone (sample position 7).

7.3 Textures by synchrotron diffraction

It is found that the above texture measurement by neutron radiation at different parts of the half-ECAP-processed Mg is still not enough to detect the specific position of the texture evolution at deformation region. There is an obvious change at deformation region (position 3, 4, 5 and 6); and it is difficult to find the exact texture changing position from this measurement. It is expected that more information will be obtained by detailed analyzing the texture evolution along the ND direction. It is also not clear that whether the ECAP-processed position 7 includes the information at positions 5 and 6 or not. Hence, gradient texture measurement by synchrotron diffraction was carried out. Texture gradient (in 1 mm each step along the ND) of sample 7 with a dimension of $7\times10\times10$ mm^3, and small samples of 3, 4, 5 and 6 with each a dimension of $4\times4\times10$ mm^3 was measured at 1 mm each step along the ND direction by synchrotron beam of 1×1 mm^2 at HARWI-II-W2, Hamburg. Recalculation of the pole figures was performed by series expansion method with an L_{max}= 10.

Fig. 7-5 shows the recalculated (0002) and $(10\bar{1}0)$ completed pole figures in the selected top and bottom parts in sample 3, 5 and 6, and sample 7 of the top, middle and bottom parts, respectively. Looking on the 1 mm thickness top part at position 3 double maxima occurs in the (00.2) pole figure, which can also be observed in the pole figure by neutron diffraction. This strong central maximum with 4.0 mrd should originate from the initial as-extruded texture; and the weaker fiber orientates about 45° to the ED. While a <00.2> fiber with its axis 10° oft from the TD is formed at the bottom part of position 3, and a girdle distribution with a weak intensity pole which originates from the top part is also observed.

At both top and bottom parts of the position 5 two components are obtained, of which one is similar as in position 3 and another is a 45° shear fiber which indicates shear deformation at the intersection plane of two vertical channels. A <00.2> fiber with strong maxima as 6.6 mrd is obtained at the top part of position 7 which is directly after inner 90° curvature angle from position 5. Remarkable is the strong maxima at the top part of position 7 which should directly come from the intense materials flow after the 90° channel. Twinning is also contributed to the strong <00.2> fiber. A combination of a shearing fiber and one component originated from position 5 is formed at the middle part of position 7. This shear fiber can also be seen in position 8.

Looking on the bottom part of the billet a double fiber distribution occurs at the top part of position 6, one is the <00.2> fiber with its axis about 8° oft to the ND and another is a less than 45° shear fiber. The shearing fiber tends to be weakened at the bottom part. When the material of the position 6 flows to the bottom part at position 7 the double fiber distribution appears again, but still less than 45° shear effect is observed. It is noted that the double fiber at position 8 is a combination of the three parts at position 7 when comparing the synchrotron results and the neutron results.

7.4 Discussion

The main texture component development from the results by neutrons in the whole 50 %-ECAP-processed pure Mg billet is schematically illustrated by an ***hcp*** cell in Fig. 7-6. It can be found that the axis of the <00.2> fiber was gradually rotated to be perpendicular to the ED. Strong rotation of this single cell starts at position 4 and 6. Results by synchrotron diffraction indicate that the weak shear starts at position 3 and are getting stronger at position 5. It is noted that the top half parts have relatively strong texture than those at half bottom part. Normally, the wildly investigated or more reported the ECAP-processed texture is measured at position 7. Due to different measurement technologies, the published ECAP-processed Mg textures are either local or bulk. However, current results indicate that textures after ECAP which according to position 7 is inhomogeneous along the ND. A clear texture gradient from the top of the billet to the bottom after ECAP of a cube-oriented Ni single crystal has also been investigated by Skrotzki et al. [127]; and the results showed that a crucial parameter strongly influences the shape of the flow lines at the top and bottom of the billet is friction, which depends not only on the die geometry, back pressure and lubrication, but also on the strength of the material.

Strain homogeneity during ECAP was studied by conducting the finite element simulations for a range channel angles from 60°~150° under the consideration of friction [128]. Large number of simulation results indicated that the deformation was deviated from simple shear. It has been revealed that the real deformation characteristics in ECAP were not perfectly homogeneous, unlike the ideal simple shear case. Sources of the deformation in-homogeneity in ECAP are summarized as [129-134]: (i) external conditions such as die geometries, loading modes (typically, backpressure and passing routes), temperature, ram speed, and die frictions; and (ii) internal conditions such as material's strain hardening ability and strain rate sensitivity. Among the various factors, friction, die corner angle and strain hardening property critically affect the deformation homogeneity of work pieces in ECAP. It should be mentioned here that the initial grain size in the current ECAP-processed Mg also plays an important role in the texture evolution. The larger the grain size more activation of twinning will happen which can greatly contribute to the formation of strong basal fiber texture.

According to the simulation results by FEM the effective strain is higher at top surface and decreases significantly at bottom part which was mainly due to the presence of the out corner angle [128, 134]. One selected simulated result by Zhao et al. is shown in Fig. 7-7 which describes the strain distribution during and after ECAP [135]. It can be found that the equivalent strain distribution is inhomogeneous in the inner region of the work piece. The equivalent strain in the front and the end parts of the work piece is smaller than the one in the center part of the work piece; and intensive shear deformation is obtained in the center part of work piece, so the equivalent strain is the maximum. Kim et al. has demonstrated that a lesser shear zone (LSZ) in the outer part of the work piece occurs when the corner angle of the die is not zero because of the shorter travel path of the outer part within the main deformation zone in that case [128, 133]. Less effective strain can be proved at the bottom position 4 which has relatively low texture intensity in pole figure. However, this is not the case at position 6, as shown in Fig. 7-5. This should be attributed to the increased local flow velocity of the work piece, as shown in Fig. 7-8 (a) the simulated strain rate during ECAP. Variation of this velocity is greatly related to the outer curvature angle and the strain hardening behavior of the work piece [132]. The larger the die corner more inhomogeneous strain distribution occurs.

Since the outer curvature angle of the present die is 37°, the pronounced inhomogeneous distribution of strain can lead to the intense shear at position 6. Highest effective strain at the top surface of the ECAP-processed billet results in a strong basal fiber texture which is position 7 under current research.

7.5 Summary

(1) Grain size was gradually decreased from the initial of 250 µm at ingoing channel to about 30 µm at outgoing channel in the 50 % ECAP-processed pure Mg. Noticeable is the obtaining of large number of twins, especially in the coarse grains. Twinning early starts before the material flows to the intersection plane of two vertical channels.

(2) Neutrons radiation texture analysis illustrated a gradient texture evolution in the 50 % ECAP-processed pure Mg. During the whole process a continuous rotation of the input texture, which a fiber texture from extrusion, was regarded from the ingoing channel over the 90° die region till the first part of the outgoing channel. Weaker texture was obtained at the bottom part of the ECAP-processed billet which indicated a less effective strain at this region.

(3) Remarkable was the low influence of the shear. More important was twinning with texture maxima at the ND in position 7. But this twinning starts much earlier in the 90° die region and has to follow the rotation by asymmetric flow. Because of the time scale effect, a weak shear fiber was found at the outgoing part where the billet firstly passed through the 90° channel.

(4) The results by neutrons measurement were insufficient and much more local texture analysis was further characterized by synchrotron diffraction, particular in the deformation region. Synchrotron measurements results indicated an inhomogeneous texture distribution along the ND. And a double fiber evolution from the 90° channel to the out-going part describes the deformation mechanism during ECAP in the current device.

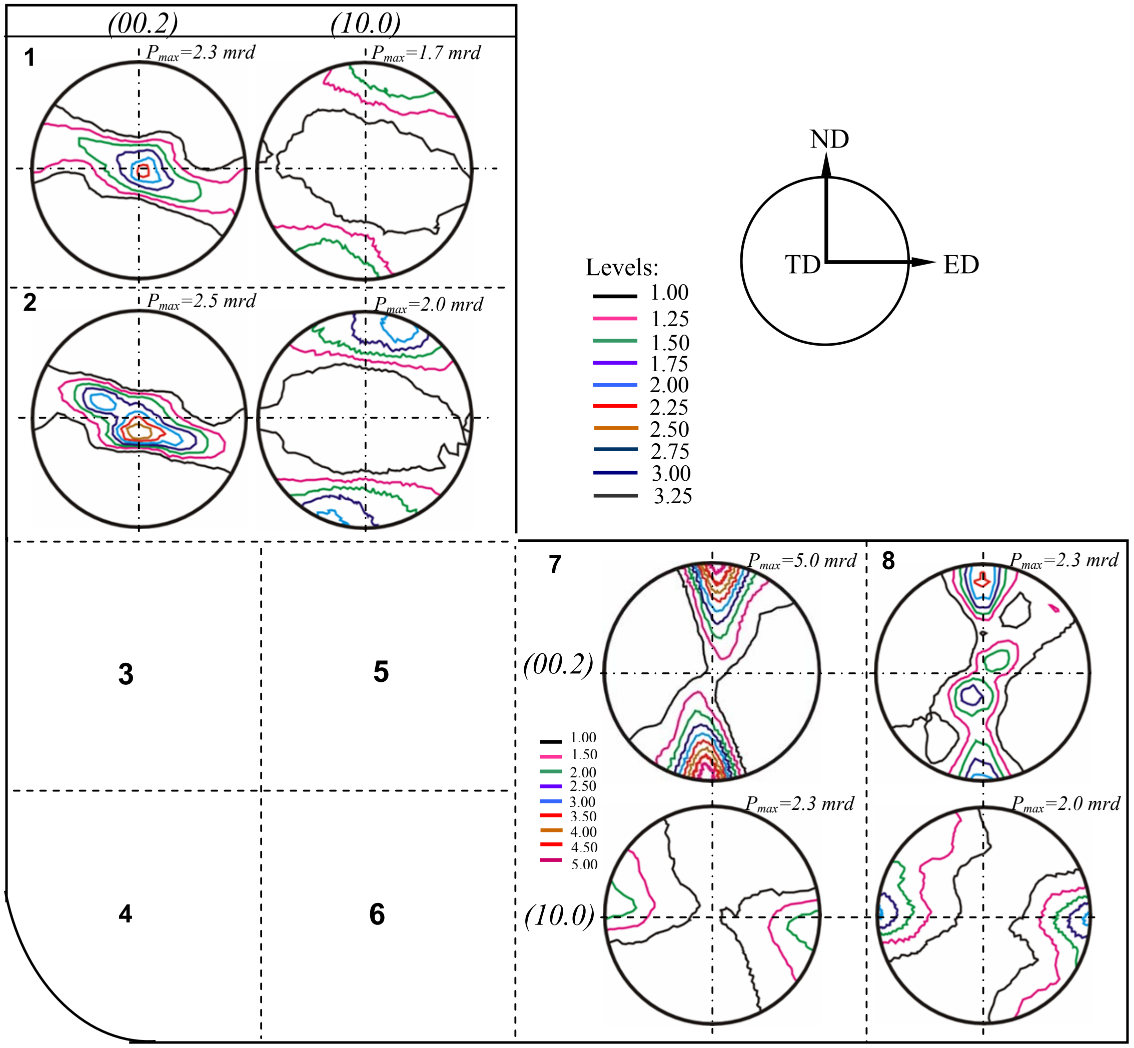

Fig. 7-3 (00.2) and (10.0) complete pole figures of the samples at different positions in the 50 % ECAP-processed pure Mg billet.

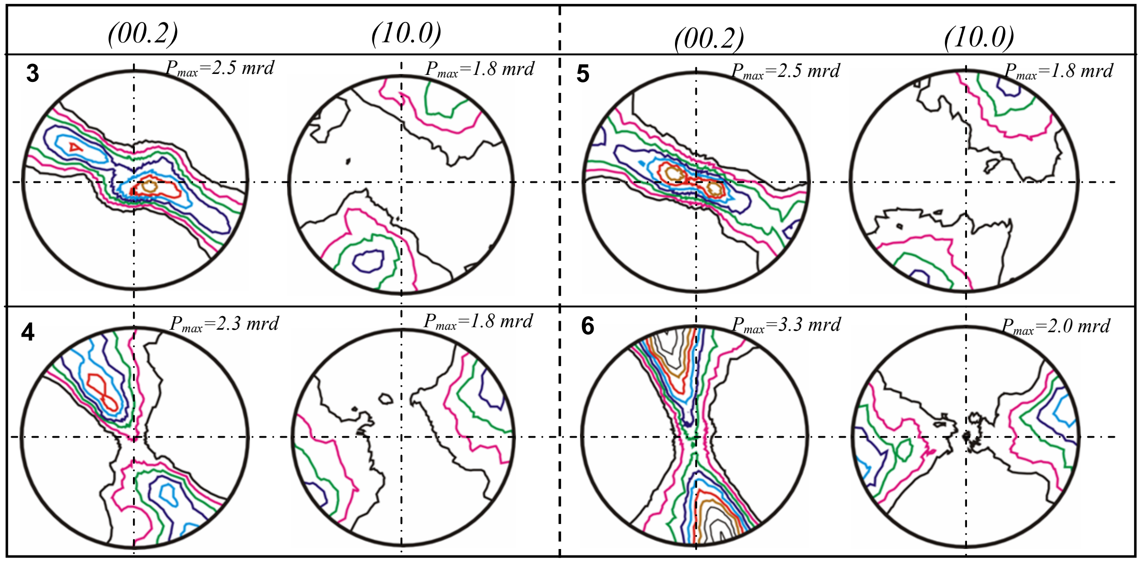

Fig. 7-4 (00.2) and (10.0) complete pole figures of the four small samples 3 to 5 which accordingly show the position as in Fig. 7-3.

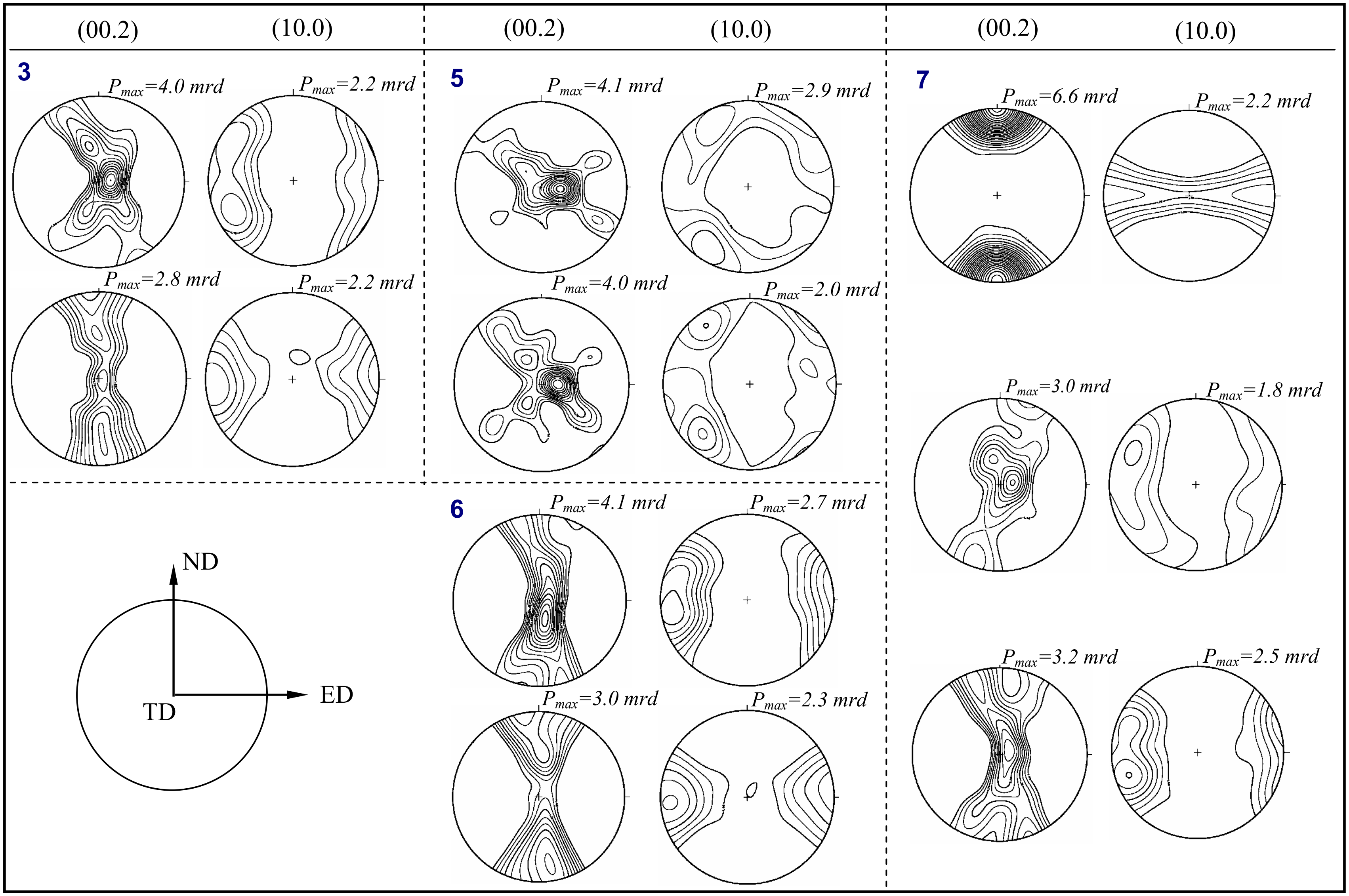

Fig. 7-5 Recalculated (00.2) and (10.0) completed pole figures for the corresponding region in Fig. 1 measured by synchrotron diffraction Contour levels=1.0×, 1.25×, 1.50×, 1.75×, …).

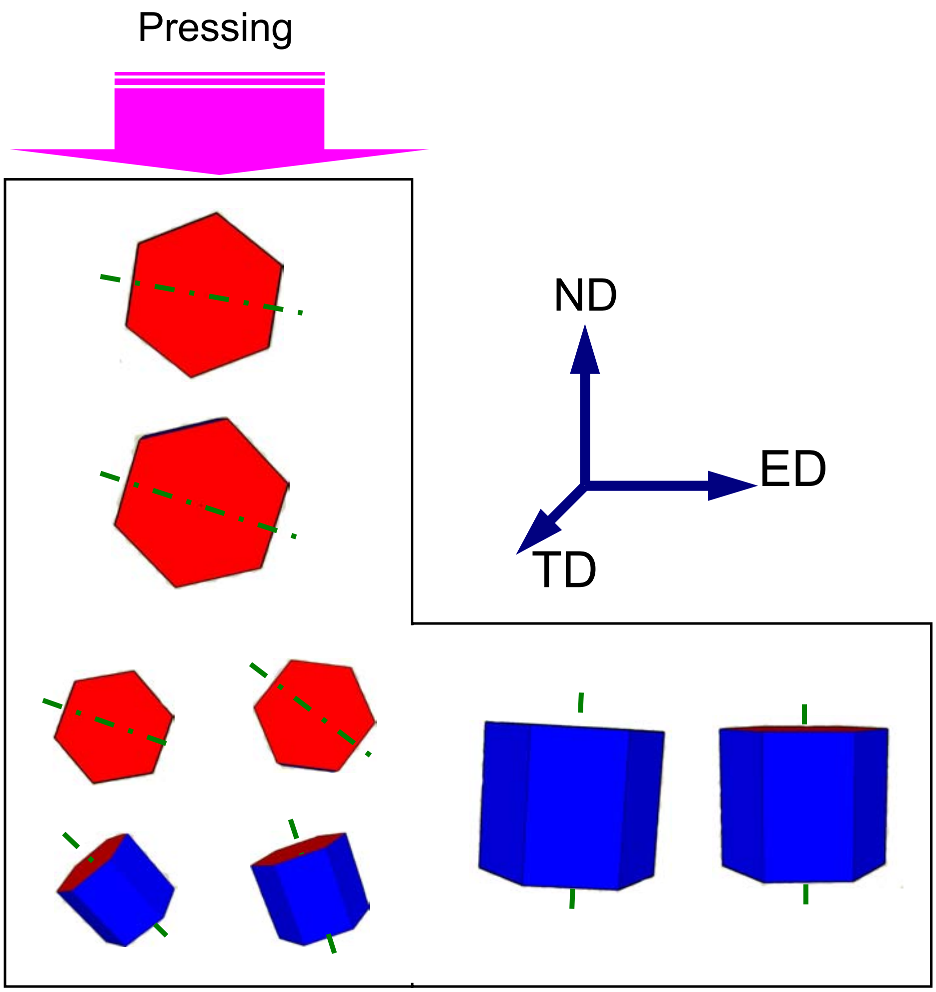

Fig. 7-6 Schematic illustration of the main texture component evolution in the 50%-ECAP-processed pure Mg billet with an ***hcp*** cell.

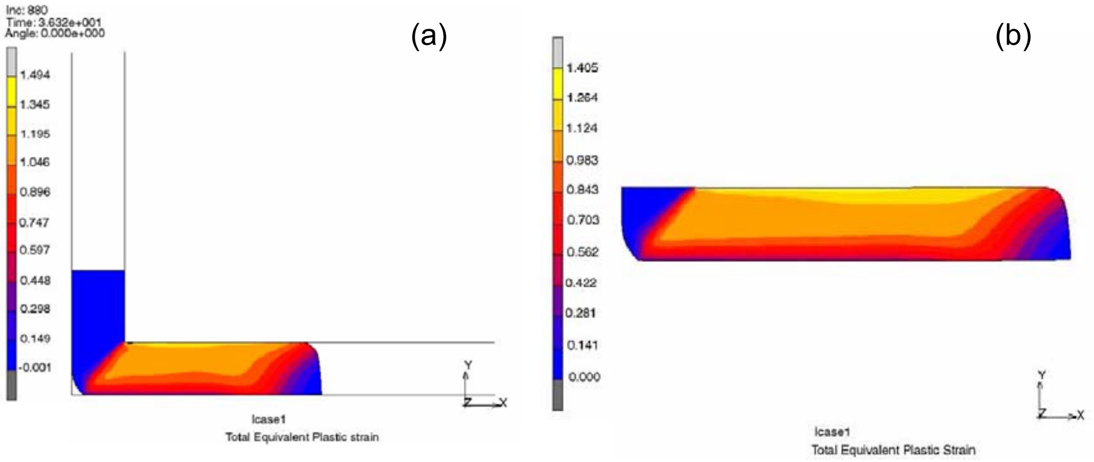

Fig. 7-7 Distribution of the total equivalent strain during the ECAP processes. (a) Steady stage of the first pass, (b) final state of the first pass [135].

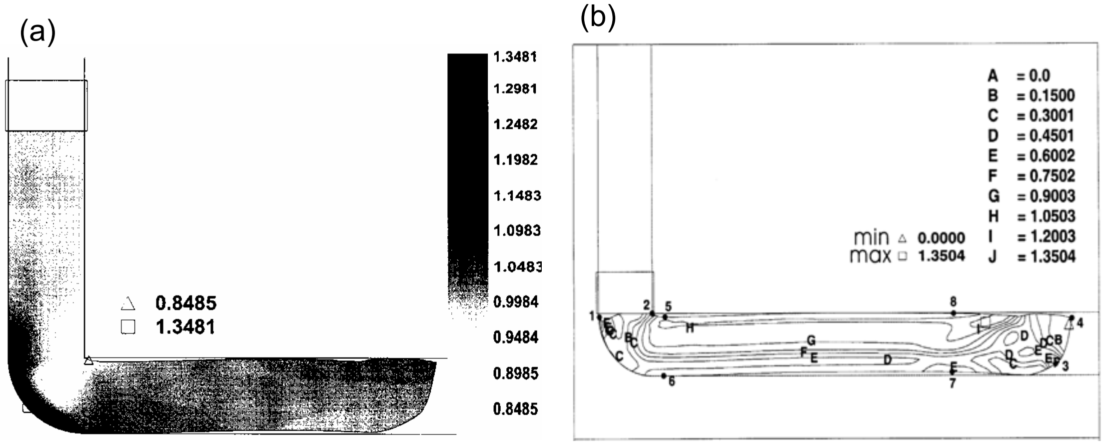

Fig. 7-8 (a) distribution of flow velocity during the ECAP process; (b) distribution of effective strain in the work piece after the ECAP process [133].

8. Conclusions

ECAP processing of as-cast and as-extruded pure Mg and Mg-Si alloy which contains hard to deform Mg_2Si particles was successfully performed with three rotation routes of A, Bc and C at present study. Evolutions of microstructure and texture via three different rotation routes processing were investigated. Grain refinement mechanism of ECAP was discussed. Refinement and re-distribution of the hard Mg_2Si particles via different routes processing were observed. Effect of the existence of Mg_2Si particles on the refinement and re-distribution of matrix grains was investigated, and as well as its effect on the texture evolution. Room temperature tensile behavior of ECAP-processed Mg and Mg-Si alloy was investigated and related to the microstructure evolution. Local texture on a single pass ECAP-processed pure Mg was also carried out by neutron and synchrotron diffraction, which should be the first study. Following results from the present study are concluded.

(1) Grains in pure Mg can be greatly refined after first two passes ECAP processing for both conditions of as-cast and as-extruded pure Mg. Further decrease of grain size is limited under the present ECAP condition which has a relatively high processing temperature. It is proposed here gradually decrease processing temperature with the increase of processing pass under the premise not to obtain cracks in the ECAP-processed billet. No distinct difference of the microstructures was found among using three routes of A, Bc and C. Large number of twins was observed in large grains.

(2) Polygonal Type-I Mg_2Si coarse grains can not be effectively broken and homogeneously redistributed during ECAP no mater the initial material is as-cast or as-extruded Mg-Si alloy under the present work, in which should be due to their more or less round morphologies and the distinct difference of the hardness at elevated temperature between Mg_2Si intermetallic phase and matrix Mg. Dendritic Type-Π Mg_2Si can be gradually broken and homogeneously redistributed in the matrix. However, the total distribution of Mg_2Si was still inhomogeneous via three routes processing. It is proposed from the present study that it is effective for the use of Si to form only eutectic Type-Π Mg_2Si to prepare Mg-Si alloy or so called in-situ Mg_2Si/Mg composite. Existence of the Mg_2Si particles can hinder the growth of matrix grains and contribute to the initiation of twinning, which could greatly improve the following mechanical property at elevated temperatures.

(3) In brief, a <00.2> basal fiber with its fiber axis having an oft angle to the ND was produced in the ECAP-processed pure Mg and Mg-Si alloy via three routes of A, Bc and C under current construction of the device. Asymmetry around the ED was obtained and unstable with each route and processing pass, which was attributed to the mismatch flow rate of work piece and the friction condition of ECAP device.

(4) Remarkable is the less shear effect which has been analyzed in detail by considering of the effects from construction of ECAP device, processing parameters and the materials inner structure. ECAP of the starting coarse grained Mg at relatively high temperature has the similar deformation as hot compression or rolling of Mg since that DRX is easily happened. Texture analysis indicated that ECAP was a complex deformation processing besides simple shear. Basal slip accommodated by twinning was the main deformation mechanism during ECAP.

(5) Texture intensity was becoming stronger with the increase of processing pass via route A and C processing, while this was vice versa via route Bc processing. Existence of Si to form Mg_2Si in Mg greatly weakened the texture comparing with pure Mg. The initial texture had limited effect on the texture evolution at first 2 passes; and similar texture was then produced in both the initial as-cast and as-extruded Mg and Mg-Si alloy.

(6) As for the as-cast pure Mg, tensile stress was increased with the increase of processing pass via three routes processing; while the maximum elongation to failure value was obtained at 2 passes which was due to the small grain size. Negative slope of the YTS versus square root of grain size $d^{-1/2}$ was obtained in the ECAP-processed pure Mg via route Bc and C processing. Texture strengthening effect was greatly contributed to this phenomenon. The maximum YTS was obtained after 1 pass in the ECAP-processed as-extruded pure Mg, but the elongation to failure value was gradually increased in the following pass processing. Relatively higher tensile strength and ductility were obtained via route Bc processing than those with route A and C processing.

(7) As for the as-cast Mg-Si alloy, the YTS and elongation to failure value were both greatly increased after ECAP due to the decrease of grain size and the homogenization of the Mg_2Si particles. Tensile stress was gradually increased with the increase of processing pass which was attributed to the more homogeneous distribution of the refined Mg_2Si particles. Distinct increase of the YTS and the elongation to failure value were obtained in the 1 pass ECAP-processed both initial as-cast and as-extruded pure Mg and Mg-Si alloy.

(8) As for the initial as-cast pure Mg and Mg-Si alloy, there was a similar trend that the YTS and ductility were both increased with the increase of process pass by all three routes. However, as for the input as-extruded materials the highest YTS value was obtained after first pass then decreased in the following pass excepting an increase of the elongation to failure value. Besides the grains size effect, the different input texture played an important role on this tensile behavior.

(9) Gradient texture evolution was investigated in a 50 % ECAP-processed pure Mg. The interesting result by neutron radiation indicated that during whole ECAP process a continuous rotation of the input texture, which was a fiber texture from extrusion, was regarded from the ingoing channel over the 90° die region till the first part of the outgoing channel. Weaker texture was obtained at the bottom part of the ECAP-processed billet. Remarkable was the low influence of the shear. More important was twinning with texture maxima at the ND in the position directly after the inner 90° angle. But this twinning started much earlier in the 90° die region and had to follow the rotation by asymmetric flow.

(10) The results by neutron radiation measurement were insufficient to further locally detect the texture evolution at deformation region where two vertical channels meet. Because of the strong texture gradient, this detailed local texture analysis was investigated by synchrotron radiation. Synchrotron results indicated an inhomogeneous texture distribution along the ND. And a double fiber evolution from the 90° channel to the outgoing part has illustrated the deformation mechanism transformation during ECAP under current construction of device.

References:

[1] C. E. Holloway, M. Melnik. *Magnesium compounds: classification and analysis of crystallographic and structural data,* J. Organometallic Chemistry. 465 (1994), p. l-63.

[2] D. Eliezer, E. Aghion, F.H. Froes. *Magnesium Science, Technology and Applications*, Advan. Perform. Mater.. 5 (1998), p. 201-212.

[3] G. C. Holywell. *Magnesium: the first Quarter Millennium*, JOM. Jul 57 (2005), p. 27-33.

[4] G. Hirt, R. Cremer, T. Witulski, H.-C. Tinius. *Lightweight near net shape components produced by thixoforming,* Mater. & Design, 18 (1997), p. 315-321.

[5] S.J. Das. *Magnesium for Automotive Applications: Primary Production Cost Assessment,* JOM. Nov 55 (2003), p. 22-26.

[6] J. Deetz. *The use of Wrought Magnesium in Bicycles*, JOM. May 57 (2005), p. 50-53.

[7] B.L. Mordike, T. Ebert. *Magnesium Properties- applications- potential*, Mater. Sci. & Eng. A302 (2001), p. 37-45.

[8] M. Mabuchi, K. Higashi. *Strengthening mechanism of Mg-Si alloys*, Scripta Mctall. & Mater, 33 (1995), p. 331-335.

[9] M. Riffel, J. Schilz. *Mechinical alloying of* Mg_2Si, Scripta Metall. Mater. 32 (1995), p.1951-1956.

[10] L. Lu, K.K. Thong, M. Gupta. *Mg-based composite reinforced by* Mg_2Si, Comp. Sci. & Techn. 63 (2003), p. 627-632.

[11] E.E. Schmid, K. Olderburg , G. Frommeyer. *Microstructures and properties of as-cast intermetallic MgSi-Al alloys,* Z. Metallkde. 81 (1990), p. 809-815.

[12] P.G. Partridge. *The crystallography and deformation modes of hexagonal close packed metals*, Metall. Rev. (1969), p.170-194.

[13] M. Suzuki, T. Kimura, J. Koike, K. Maruyama. *Strengthening effect of Zn in heat resistant Mg-Y-Zn solid solution alloys*, Mater. Sci. & Eng . A252 (1998), p. 248-255.

[14] M.H. Yoo, S.R. Agnew, J.R. Morris, K.M. Ho. *Non-basal slip systems in HCP metals and alloys : source mechanism*, Mater. Sci. and Eng. A319-321 (2001), p. 87-92.

[15] M.H. Yoo, J.R. Morris, K.M. Ho, S.R. Agnew. *Nonbasal deformation modes of HCP metals and alloys: Role of dislocation source and mobility*, Metall. And Mater. Trans. 33A (2002), p. 813-821.

[16] S.B. Yi, S. Zaefferer, H.-G. Brokmeier. *Mechanical behaviour and microstructural evolution of magnesium alloy AZ31 in tension at different temperatures*, Mater. Sci. & Eng. A 424 (2006), p.275-281.

[17] M. H. Yoo, S. R. Agnew, J. R. Morris, K. M. Ho. *Non-basal slip systems in HCP metals and alloys: source mechanisms*, Mater. Sci. & Eng. 319-321(2001), p. 87-92.

[18] J. Koike, T. Kobayashi, T. Mukai, H. Watanabe, M. Suzuki, K. Maruyama, K. Higashi. *The activity of non-basal slip systems and dynamic recovery at room temperature in fine-grained AZ31B magnesium alloys*, Acta Mater. 51 (2003), p. 2055-2065.

[19] M. Mabuchi, K. Ameyama, H. Iwasaki, K. Higashi. *Low temperature superplasticity of AZ91 magnesium alloy with non-equilibrium grain boundaries*, Acta Mater. May 47 (1999), p. 2047-2057.

[20] M.R. Barnett. *Twinning and the ductility of magnesium alloys: Part I: 'Tension' twins*, Mater. Sci. & Eng. A 464 (2007), p. 1-7.

[21] M.R. Barnett. *Twinning and the ductility of magnesium alloys Part II. 'Contraction' twins*, Mater. Sci. & Eng. A 464 (2007), p. 8-16.

[22] H. Yoshinaga, T. Obara, S. Morozumi. *Twinning deformation in magnesium compressed along the c-axis*, Mater. Sci. & Eng. A 12 (1973), p. 255-264.

[23] B.C. Wonsiewicz, W. A. Backofen. *Plasticity of magnesium crystals*, Trans AIME. 239 (1967), p. 1422-1431.

[24] R.E. Reed-Hill, W.D. Robertson. *The crystallographic characteristic fracture in magnesium single crystal,* Acta Metall. 5 (1957), p. 717-728.

[25] L. Jiang, J. J. Jonas, A. A. Luo, A. K. Sachdev, S. Godet. *Twinning-induced softening in polycrystalline AM30 Mg alloy at moderate temperatures*, Scripta Materialia. 54 (2006), p. 771-775.

[26] C.W. Tan, S.N. Xu, L. Wang, Z.Y. Chen, F. C. Wang, H. N. Cai. E*ffect of temperature on mechanical behavior of AZ31 magnesium alloy*, Transactions of Nonferrous Metals Society of China, 17 (2007), p. 41-45.

[27] M.R. Barnett, D.L. Atwell, A.G. Beer. *Grain size in Mg Alloys: Recrystallization and Mechanical Consequences*, Mater. Sci. Foru. 558-559 (2007), p. 433-440.

[28] M. R. Barnett, A. G. Beer, D. Atwell, A. Oudin. *Influence of grain size on hot working stresses and microstructures in Mg-3Al-1Zn*, Scripta Materialia, 51 July (2004), p.19-24.

[29] R.Z. Valiev, T.G. Langdon. *Principles of equal-channel angular pressing as a processing tool for grain refinement*, Prog. in Mater. Sci. 51 (2006), p. 881-981.

[30] V.M. Segal. *Materials processing by simple shear*, Mater. Sci. & Eng. A197 (1995), p. 157-164.

[31] V.M. Segal. *Severe plastic deformation: simple shear versus pure shear*, Mater. Sci. & Eng. A338 (2002), p. 331-344.

[32] R.Z. Valiev, I.V. Alexandrov. *Nanostructured materials from severe plastic deformation*, NanoStructured Mater. 12 (1999), p. 35-40.

[33] G. Sakai, K. Nakamura, Z. Horita, T.G. Langdon. *Application of High Pressure Torsion to Bulk Samples*, Mater. Sci. Foru. 503-504 (2006), p. 391-398.

[34] J.Y. Huang, Y.T. Zhu, H. Jiang, T. C. Lowe. *Microstructures and dislocation configurations in nanostructured Cu processed by repetitive corrugation and straightening*, Acta Mater., 49 May (2001), p. 1497-1505.

[35] J.Y. Huang, Y.T. Zhu, D.J. Alexander, X.Z. Liao, T.C. Lowe, R.J.Asaro. *Development of repetitive corrugation and straightening*, Mater. Sci. & Eng. A371 (2004), p. 35-39.

[36] N. Nobuhiro, Y. Saito, S.H. Lee, Y. Minamino. *ARB (Accumulative Roll-Bonding) and other new Techniques to Produce Bulk Ultrafine Grained Materials*, Advan. Eng. Mater. 5 (2003), p. 338-344.

[37] M. Karlik, P. Homola, M. Slámová. *Accumulative roll-bonding: first experience with a twin-roll cast AA8006 alloy*, J. Alloys & Comp. 378 (2004), p. 322-325.

[38] G.A. Salishchev, O.R. Valiakhmetov, R.M. Galeyev. *Formation of submicrocrystalline structure in the titanium alloy VT8 and its influence on mechanical properties*, J. Mater. Sci. 28 (1993), p. 2898-2902.

[39] V. Varyukhin, Y. Beygelzimer, S. Synkov, D. Orlov. *Application of Twist Extrusion*, Mater. Sci. Foru. 503-504 (2006), p. 335-340.

[40] M. Richert, Q. Liu, N. Hansen. *Microstructural evolution over a large strain range in aluminum deformed by cyclic-extrusion–compression*, Mater. Sci. & Eng. A260 (1999), p. 275-283.

[41] C.G. Rhodes, M.W. Mahoney, W.H. Bingel, R.A. Spurling, C.C. Bampton. *Effects of ftction stir welding on microstructure of 7075 Aluminum*, Scripta Mater. 36 (1997), p. 69-75.

[42] D.C. Hofmann, K. S. Vecchio. *Submerged friction stir processing (SFSP): An improved method for creating ultra-fine-grained bulk materials*, Mater. Sci. & Eng. A 402 (2005), p. 234-241.

[43] V.M. Segal. *Equal channel angular extrusion: from macromechanics to structure formation*, Mater. Sci. & Eng. A271 (1999), p. 322-333.

[44] V.M. Segal, USSR Patent No. 575892 (1977).

[45] Y. Iwahashi, J.T. Wang, Z. Horita, M. Nemoto, T.G. Langdon. *Principle of equal-channel angular pressing for the processing of ultra-fine grained materials*, Scripta Mater. 35 (1996), p. 143-146.

[46] M. Furukawa, Z. Horita, M. Nemoto, T.G. Langdon. *Review-Processing of metals by equal-channel angular pressing*, J. Mater. Sci. 36 (2001), p. 2835-2843.

[47] Y. T. Zhu, T.C. Lowe. *Observations and issues on mechanisms of grain refinement during ECAP process*, Mater. Sci. & Eng. A291 (2000), p. 46-53.

[48] P.B. Berbon, M. Furukawa, Z. Horita, M. Nemoto, T.G. Langdon. *An Examination of the Deformation Process in Equal-Channel Angular Pressing*, Mat. Res. Soc. Symp. Proc. 601(2000), p. 347-352.

[49] Y. Iwahashi, Z. Horita, M. Nemoto, T. G. Langdon. *An investigation of microstructural evolution during equal-channel angular pressing*, Acta Materialia. November 45 (1997), p. 4733-4741.

[50] M. Furukawa, Y. Iwahashi, Z. Horita, M. Nemoto, T.G. Langdon. *The shearing characteristics associated with equal-channel angular pressing*, Mater. Sci. & Eng. A257 (1998), p. 328-332.

[51] K. Furuno, H. Akamatsu, K. Oh-ishi, M. Furukawa, Z. Horita, T.G. Langdon. *Microstructural development in equal-channel angular pressing using a 60° die*, Acta Materialia.
May 52 (2004), p. 2497-2507.

[52] I. P. Semenova, G. I. Raab, L. R. Saitov, R. Z. Valiev. *The effect of equal-channel angular pressing on the structure and mechanical behavior of Ti-6Al-4V alloy*, Mater. Sci. & Eng. A387-389 (2004), p. 805-808.

[53] K. Nakashima, Z. Horita. M. Nemoto,T.G. Langdon. *Influence of channel angle on the development of ultra-fined grains in equal-channel angular pressing*, Acta Mater. 46 (1998), p. 1589-1599.

[54] T.G. Langdon. *The principles of grain refinement in equal-channel- angular pressing*, Mater. Sci. & Eng. A462 (2007), p. 3-11.

[55] S.C. Yoon, P. Quang, S.I. Hong, H.S. Kim. *Die design for homogeneous plastic deformation during equal channel angular pressing*, J. Mater. Proc. Techn. 187-188 (2007), p.46-50.

[56] H. S. Kim, M. H. Seo, S.I. Hong. *On the die corner gap formation in equal channel angular pressing*, Mater. Sci. & Eng. A291 (2000), p. 86-91.

[57] M. Furukawa, Y. Kawasaki, Y. Miyahara, Z. Horita, T.G. Langdon. *An investigation of the deformation process during equal-channel angular pressing of an aluminum single crystal*, Mater. Sci. & Eng. 410-411 (2005), p. 194-200.

[58] H. S. Kim, M.H. Seo, S.I. Hong. *Plastic deformation analysis of metals during equal channel angular pressing*, J. Mater. Proc. Techn. 113 June (2001), p. 622-626.

[59] C.J. Luis Pe′rez. *On the correct selection of the channel die in ECAP processes*, Scripta Mater. 50 (2004), p. 387-393.

[60] A.Yamashita, D. Yamaguchi,Z. Horita, T.G. Langdon. *Influence of pressing temperature on microstructural development in equal-channel angular pressing*, Mater. Sci. & Eng. A287 (2000), p. 100-106.

[61] D.H. Shin, J.J. Pak, Y.K. Kim, K.T. Park, Y.S. Kim. *Effect of pressing temperature on microstructure and tensile behavior of low carbon steels processed by equal channel angular pressing*, Mater. Sci. & Eng. A325 (2002), p. 31-37.

[62] Y.C. Chen, Y.Y. Huang, C.P. Chang, P.W. Kao. *The effect of extrusion temperature on the development of deformation microstructures in 5052 aluminum alloy processed by equal channel angular extrusion*, Acta Mater. 51 (2003), p. 2005-2015.

[63] W.H. Huang, C.Y. Yu, P.W. Kao, C.P. Chang. *The effect of strain path and temperature on the microstructure developed in copper processed by ECAE*, Mater. Sci. & Eng. A366 (2004), p. 221-228.

[64] P.B. Berbon, M. Furukawa, Z. Horita, M. Nemoto, T.G. Langdon. *Influence of pressing speed on microstructural development in equal-channel angular pressing*, Metall. Mater. Trans. 30A (1999), p. 1989-1997.

[65] R.Z. Valiev. *Paradox of severe plastic deformation*, Advan. Eng. Mater. 5 (2003), p. 296-300.

[66] R.Z. Valiev, I.V. Alexandrov, Y.T. Zhu, T.C. Lowe. *Paradox of strength and ductility in metals by severe plastic deformation*, J. Mater. Res. 17 (2002), p. 5-8.

[67] S.L. Semiatin, D.P. DeLo, E.B. Shell. *The effect of material properties and tooling design on deformation and fracture during equal channel angular extrusion*, Acta Mater. 48 (2000), p.1841-1851.

[68] R.Z. Valiev, R.K. Islamgaliev, I.V. Alexandrov. *Bulk nanostructured materials from severe plastic deformation*, Prog. in Mater. Sci. 45 (2000), p. 103-189.

[69] P.W.J. Mckenzie, R. Lapovok, Y. Estrin. *The influence of back pressure on ECAP processed AA 6016: Modeling and experiment*, Acta Mater. 55 (2007), p. 2985-2893.

[70] K. Xia, W. Xu. *Back pressure equal channel angular consolidation of Al particles*, Scripta Mater. 53 (2005), p. 1225-1229.

[71] K. Xia, J.T. Wang, X. Wu, G. Chen, M. Gurvan. *Equal channel angular pressing of magnesium alloy AZ31*, Mater. Sci. & Eng. A410-411 (2005), p. 324-327.

[72] R. Lapovok, P. F. Thomson, R. Cottamy, Y. Estrin. *Extraordinary superplastic ductility of magnesium alloy ZK60*, J. Mater. Sci. 40 (2005), p. 1699-1708.

[73] L. Jin, D.L. Lin, D. Mao, X.Q. Zeng, W.J. Ding. *Mechanical properties and microstructure of AZ31 Mg alloy processed by two-step equal channel angular extrusion*, Mater. Lett. 59 (2005), p. 2267-2270.

[74] T. Liu, S.D. Wu, S.X. Li, P.J. Li. *Microstructure evolution of Mg-14% Li-1% Al alloy during the process of equal channel angular pressing*, Mater. Sci. & Eng. A460-461 (2007), p. 499-503.

[75] M.Y. Zheng, S.W. Xu, K. Wu, S. Kamado , Y. Kojima. *Superplasticity of Mg-Zn-Y alloy containing quasicrystal phase processed by equal channel angular pressing*, Mater. Lett. 61 (2007), p. 4406-4408.

[76] Y. Miyahara, Z. Horita, T.G. Langdon. *Exceptional superplasticity in an AZ61 magnesium alloy processed by extrusion and ECAP*, Mater. Sci. & Eng. A420 (2006), p. 240-244.

[77] W.J. Kim, C.W. An, Y.S. Kim, S.I. Hong. *Mechanical properties and microstructures of an AZ61 Mg Alloy produced by equal channel angular pressing*, Scripta Mater.47 (2002), p. 39-44.

[78] K. Matsubara, Y. Miyahara, Z. Horita, T. G. Langdon. *Developing superplasticity in a magnesium alloy through a combination of extrusion and ECAP*, Acta Mater, 51 June (2003), p. 3073-3084.

[79] W.J. Kim, Y.K. Sa. *Micro-extrusion of ECAP processed magnesium alloy for production of high strength magnesium micro-gears*, Scripta Mater. 54 (2006), p. 1391-1395.

[80] R.Z.Valiev. *Nanostructuring of metals by severe plastic deformation for advanced properties*, Nature Mater. Aug 3 (2004), p. 511-516.

[81] H.-R. Wenk, P. Van. Houtte. *Texture and anisotropy*, Rep. Prog. Phys. 67 (2004), p. 1367-1428.

[82] H.J. Bunge. *Texture Analysis in Materials Science*, Cuvillier Verlag, Göttingen, 1993.

[83] H.J. Bunge, C. Esling. *Quantitative Texture Analysis*. DGM Informationsgesellschaft, Oberursel, 1982.

[84] R.-J. Roe. *Description of crystallite orientation in polycrystalline materials III, general solution to pole figure inversion*, J. Appl. Phys. 36 (1965), p. 2024.

[85] S. Matthies. *On the basic elements of and practical experience with the WIMV algorithm- an ODF reproduction method with conditional ghost correction*, ICTOM (1998), p.37-48.

[86] W.R. Phillips. *Mineral Optics*: San Francisco, W.H. Freeman and Co, 1971.

[87] H.J. Bunge. *Experimental Techniques of Texture Analysis*, DGM Informationsgesellschaft, Oberursel, 1986.

[88] H.-G. Brokmeier. *Advances and applications of neutron texture analysis*. Textures & Micro 33 (1999), p. 13-33.

[89] H.-G. Brokmeier. *Neutron Diffraction Texture Analysis of Multi-Phase Systems*, Textures & Microstructures. 10 (1989), p. 325-346.

[90] Y.N. Wang, J.C. Huang. T*exture analysis in hexagonal materials*, Mater. Chem. & Phy. 81 (2003), p. 11-26.

[91] J. Bohlen, S.B. Yi, J. Swiostek, D. Letzig, H.G. Brokmeier, K.U. Kainer. *Microstructure and texture development during hydrostatic extrusion of magnesium alloy AZ31*, Scripta Mater. 53 (2005), p. 259-264.

[92] G. Garcés, M. C. Cristina, M. Torralba, P. Adeva. *Texture of magnesium alloy films growth by physical vapour deposition*, J. Alloys & Comp. 309 (2000), p. 229-238.

[93] A. Styczynski, C.H. Hartig, J. Bohlen, D. Letzig. *Cold rolling textures in AZ31 wrought magnesium alloy*, Scripta Mater. 50 (2004), p. 943-950.

[94] M. T. Pérez-Prado, J. A. del Valle, J. M. Contreras, O. A. Ruano. *Microstructural evolution during large strain hot rolling of an AM60 Mg alloy*, Scripta Mat. 50 March (2004), p. 661-665.

[95] Y. Chino, K. Sassa, A. Kamiya, M. Mabuchi. *Enhanced formability at elevated temperature of a cross-rolled magnesium alloy sheet*, Mater. Sci. & Eng. 441 (2006), p. 349-356.

[96] S.H. Kim, B.S. You, C.D. Yim, Y.M. Seo. *Texture and microstructure changes in asymmetrically hot rolled AZ31 magnesium alloy sheets*, Mater. Lett. 59 (2005), p. 3876-3880.

[97] D. D. Roger. *Recrystallization and texture*, Prog. in Mater. Sci. 42 (1997), p. 39-58.

[98] M. T. Pérez-Prado, O. A. Ruano. *Texture evolution during annealing of magnesium AZ31 alloy*, Scripta Mat. 46 January (2002), p. 149-155.

[99] W.H. Huang, L. Chang, P.W. Kao, C.P. Chang. *Effect of die angle on the deformation texture of copper processed by equal channel angular extrusion*, Mater. Sci. & Eng. A307 (2001), p. 113-118.

[100] S. Ferrasse, V.M. Segal, S.R. Kalidindi, F. Alford. *Texture evolution during equal channel angular extrusion, Part I. Effect of route, number of passes and initial texture*, Mater. Sci. & Eng. A368 (2004), p. 28-40.

[101] S. Ferrasse, V.M. Segal, S.R. Kalidindi, F. Alford. *Texture evolution during equal channel angular extrusion (ECAE), Part II. An effect of pos-deformation annealing*, Mater. Sci. & Eng. A372 (2004), p. 235-244.

[102] S.R. Agnew, P. Mehrotra, T.M. Lillo, G.M. Stoica, P.K. Liaw. *Crystallographic texture evolution of three wrought magnesium alloys during equal channel angular extrusion*, Mater. Sci. & Eng. A408 (2005), p. 72-78.

[103] W.J. Kim, S.I. Hong, Y.S. Kim, S.H. Min, H.T. Jeong, J.D. Lee. *Texture development and its effect on mechanical properties of an AZ61 Mg alloy fabricated by equal channel angular pressing*, Acta Mater. 51 (2003), p. 3293-3307.

[104] T. Liu, Y.D. Wang, S.D. Wu, R. L. Peng, C.X. Huang, C.B. Jiang, S.X. Li. *Textures and mechanical behavior of Mg-3.3%Li alloy after ECAP*, Scripta Mater. 51 (2004), p. 1057-1061.

[105] G.I. Taylor. *Analysis of plastic strain in cubic crystal*, Mechanics of Solids. (1938), p.218.

[106] A. Molinari, G.R. Canova, S. Azhi. *A self consistent approach of the large deformation polycrystal viscoplasticity*, Acta Metall. 35 (1987), p. 2983-2994.

[107] A. Molinari, L.S. Toth. *Tuning self consistent viscoplastic model by finite element results-I. Modeling*, Acta Metall. Mater. 42 (1994), p. 2453.

[108] J.F.W. Bishop, R. Hill. *A theory of plastic distortion of polycrystalline aggregate under combined stress*, Philos. Mag. 42 (1951), p. 414.

[109] V.P. Houtte. *Simulation of the rolling and shear texture of brass by the Taylor theory adapted for mechanical twinning*, Acta Metall., 26 (1978), p. 591-604,

[110] G.R. Canova, C. Fressengeas, A. Molinari, U.F. Kocks. *Effect of rate sensitivity on slip system activity and lattice rotation*, Acta Metall.36 (1988), p. 1961-1970.

[111] R.A. Lebensohn, C.N. Tome. *A self-consistent anistropic approach for the simulation of plastic deformation and texture development of polycrystals: application to zirconium alloys*, Acta metal. Mater, 41 (1993), p. 2611-2624.

[112] R.A. Lebensohn, C.N. Tome. *A self-consistent viscoplastic model: prediction of rolling textures of anistropic polycrystals*, Mater. Sci. & Eng. A175 (1994), p. 71-82.

[113] I.J. Beyerlerin, R.A. Lebensohn, C.N. Tome. *Modeling texture and microstructural evolution in the equal channel angular extrusion process*, Mater. Sci. & Eng. A345 (2003), p. 122-138.

[114] C. N. Tome, R. A. Lebensohn, U. F. Kocks. *A model for texture development dominated by deformation twinning: Application to zirconium alloys*, Acta metal. Mater., 39 (1991), p. 2664-2680.

[115] Q.L. Jin, S. Y. Shim, S.G. Lim. *Correlation of microstructural evolution and formation of basal texture in a coarse grained Mg-Al alloy during hot rolling*, Scripta Mater 55(2006), p. 843-846.

[116] H.L. Ding, L.F. L, S.H. Kamado, W.J.Ding, Y. Kojima. *Evolution of microstructure and texture of AZ91 alloy during hot compression*, Mater. Sci. & Eng. A452-453 (2007), p. 503-507.

[117] R. Gehrmann, M.M. Formmert, G. Gottstein. *Texture effects on plastic deformation of magnesium*, Mater. Sci. & Eng. A395 (2005), p. 338-349.

[118] C. Pithan, T. Hashimoto, M. Kawazoe, J. Nagahora, K. Higashi. *Microstructure and texture evolution in ECAE processed A5056*, Mater. Sci. & Eng. A280 (2000), p. 62-68.

[119] A.Gohlinia, P. Bate, P.B. Prangnell. *Modelling texture development during equal channel angular extrusion of aluminium*, Acta Mater. 50 (2002), p. 2121-2136.

[120] N.J. Petch. *The cleavage strength of polycrystals*, J. Iron Steel Inst. 174 (1953), p. 25-28.

[121] S.B. Yi, C.H. Davies, H.-G. Brokmeier, R.E. Bolmaro, K.U. Kainer, J. Homeyer. *Deformation and texture evolution in AZ31 magnesium alloy during uniaxial loading*, Acta Mater. 54 (2006), p. 549-562.

[122] Z. Horita, T. Fujinami, M. Nemoto, T.G. Langdon. *Improvement of mechanical properties for Al alloys using equal-channel angular pressing*, J. Mater. Proce. Techn. 117 (2001), p. 288-292.

[123] P. Lukáč, Z. Trojanová . *Hardening and softening in selected magnesium alloys*, Mater Sci & Eng. A462 (2007), p. 23-28.

[124] G. Proust, C.N. Tomé, G.C. Kaschner. *Modeling texture, twinning and hardening evolution during deformation of hexagonal materials*, Acta Mater, 55 (2007), p. 2173-2184.

[125] T.G. Nieh, A.J. Schwartz, J. Wadsworth. *Superplasticity in a 17 vol.% SiC particulat-reinforced ZK60A magnesium composite (ZK60/SiC/17p)*, Mater Sci & Eng. A208 (1996), p. 30-36.

[126] J. M. Garcia-infanta, A.P. Zhilyaev, C.M. Cepeda-Jimenez, O.A. Ruano, F. Carreno. *Effect of the deformation path on the ductility of a hypoeutectic Al–Si casting alloy subjected to equal-channel angular pressing by routes A, B_A, B_C and C*, Scripta Mater 58 (2008), p. 138-141.

[127] W. Skrotzki, L.S. Toth, B. Kloden, H.-G. Brokmeier, R. Arruffat-Massion. *Texture after ECAP of a cube-oriented Ni single crystal*, Acta Mater, 56 (2008), p. 3439-3449.

[128] H.S. Kim. *Finite element analysis of equal channel angular pressing using a round die*, Mater. Sci. & Eng., A315 (2001), p. 122-128.

[129] H.S. Kim, M.H. Seo, S.I. Hong. *On the die corner gap formation in equal channel angular pressing*, Mater. Sci. & Eng. A291 (2000), p. 86-90.

[130] A.V. Nagasekhar, Yip Tick-Hon, H.P. Seow. *Deformation behavior and strain homogeneity in equal channel angular extrusion/pressing*, J. Mater. Proc. Techn. 192-193 (2007), p. 448-452.

[131] B.S. Moon, H.S. Kim, S.I. Hong. *Plastic flow and deformation homogeneity of 6061 Al during Equal Channel Angular Pressing,* Scripta, Mater. 46 (2002), p. 131-136.

[132] R.B. Figueiredo, P.R. Cetlin, T.G. Langdon. *The processing of difficult-to-work alloys by ECAP with an emphasis on magnesium alloys*, Acta Mater. 55 (2007), p. 4769-4779.

[133] H.S. Kim. *Evalutation of strain rate during equal channel angular pressing*, J. Mater. Res.
17 (2002), p. 172-179.

[134] S. Dumoulin, H.J. Roven, J.C. Werenskiold, H.S. Valberg. *Finite element modeling of equal channel angular pressing: Effect of material properties, friction and die geometry*, Mater. Sci. & Eng. A 410-411 (2005), p. 248-251.

[135] W.J. Zhao, H. Ding, Y. P. Ren, S.M. Hao, J. Wang, J.T. Wang. *Finite element simulation of deformation behavior of pure aluminum during equal channel angular pressing*, Mater. Sci. & Eng. A410-411(2005), p. 348-352.

[136] C. Xu, M. Furukawa, Z. Horita, T.G. Langdon. *The evolution of homogeneity and grain refinement during equal-channel angular pressing: A model for grain refinement in ECAP*. Mater. Sci. & Eng. A 398 (2005), p. 66-76.

[137] C.W. Su, L. Lu, M.O. Lai. *A model for the grain refinement mechanism in euqal channel angular pressing of Mg alloy from microstructural studies*. Mater. Sci. & Eng. A434 (2006), p. 227-236.

[138]] L. S. Toth, R. A. Massion, L. Germain, S. C. Baik, S. Suwas. *Analysis of texture evolution in equal channel angular extrusion of copper using a new flow filed*. Actat Mater., 52, (2004), p. 1885-1898.

[139] V.M. Segal. *Slip line solutions, deformation mode and loading history during equal channel angular extrusion*. Mater. Sci. & Eng. A345 (2003), p.36-46.

Curriculum Vitae

Personal information:

Surname: Gan
Given name: Weimin
Gender: Male
Date of Birth: 13.09.1980
Place of birth: Anhui Province, P. R. China
Citizenship: Chinese

Current post address: GKSS Research Center,
Max-Planck-strasse 1, Geb 03,
21502, Geesthacht,
Germany
Tel: +49-4152-871327
Fax: +49-4152-871338
E-mail: weimin.gan@gmail.com, weimin.gan@gkss.de

Education:

1996 - 1998	Middle school study , Taihu Middle School, Anhui Province
1998 - 2002	Bachelor degree study, major in materials science, Anhui University of Technology and Science, Wuhu China.
2002 - 2004	Master degree study, major in materials science. Harbin Institute of Technology, Harbin China.
2004 - 2008	PhD candidate in materials science, Harbin Institute of Technology, Harbin China.
2005 - 2008	PhD candidate in materials science, Clausthal University of Technology, Germany.

Professional experience:

2005 - 2008	DAAD-Helmholtz scholarship holder at GKSS, Geesthacht Germany.
2006 - 2008	Research assistant at Institute of Materials Science and Engineering , Clausthal University of Technology, Clausthal-Zellerfeld Germany.

Name, Vorname:
Gan Weimin

Datum:
13.09.2008

EIDESSTATTLICHE ERKLÄRUNG

Hiermit erkläre ich an Eides Statt, dass die eingereichte Dissertation weder in Teilen noch in Ihrer Gesamtheit einer anderen Hochschule zur Begutachtung vorliegt oder vorgelegen hat und dass ich bisher noch keinen Promotionsversuch unternommen habe.

Unterschrift

Ganweimin